Faculté des bioingénieurs

Spatial and temporal risk assessment of crop yield loss from tephra fall: A case study on Mount Etna

Author: Zoé Saintrain

Supervisors: Prof. Pierre Delmelle (UCLouvain/SST/ELI/ELIE),
Hind Dib (UCLouvain/SST/ELI/ELIE)

Readers: Prof. Patrick Bogaert (UCLouvain/SST/ELI/ELIE),
Prof. Sébastien Biass (UNIGE/SSTE/DST)

Academic year 2024-2025

Master's thesis presented in fulfillment of the requirements for the degree of Bioengineer in Agricultural Sciences

During the writing of this work, the author used Chat GPT 5 (OpenAI, USA), a generative AI model, as a support tool to check grammar and improve clarity. No text generation was used. All content was reviewed and edited by the author. The author assumes full responsibility for the content of this thesis.

Acknowledgement

Before presenting this work, I wish to express my sincere gratitude to all those who contributed to the completion of this master's thesis.

First, I would like to thank my co-supervisors: Professor Pierre DELMELLE and Hind DIB. Thank you for your guidance, patience and kindness. A special thank you to Pierre for his expert advice and careful reviews. To Hind, I am grateful for your encouragement and availability. Our discussions helped me to focus and structure my research and to overcome the obstacles along the way.

I would also like to thank my readers, Professors Patrick BOGAERT and Sébastien BIASS, for devoting their time and attention to reading this work and for their help throughout the year. Sébastien, thank you for your invaluable assistance with TephraProb and the eruption simulations.

Thanks to Doctor Aubry VANDEUREN, who basically taught me how to code in R, was always enthusiastic about helping me when I got stuck and was a source of inspiration. This work would have been less successful without his help. I would also like to thank Baptiste DELHEZ for his consistent availability and willingness to answer my questions.

I am beyond grateful to my parents and grandparents for taking care of me throughout the process of writing this thesis, for giving me the opportunity to attend university and for providing the support I needed to complete it.

I would like to thank all my long-standing friends as well as those I have met along the way. Thank you for making my time at UCLouvain truly unforgettable. Our shared moments, from conversations and laughter to collaborative study sessions and mutual support, helped me during the journey. Thank you, Camille and Victorine, for your unfailing friendship. Thank you, Luna, Ombeline and Guigui for being my everyday study buddies this year. Thank you, Lison, for your support. Thank you, Clémentine, for always listening. Thank you, Ismaël, for your reviews. I am truly grateful to the Agro Faculty for the opportunity to meet so many incredible people.

Last but not least, thank you, Sebastian for being there for me unconditionally and inspiring me to find joy and wonder in academic work.

The only people I will not be thanking are those who stole my computer three weeks before the deadline. Instead, I will be thanking the cloud for existing.

Table of Contents

List of Figures

List of Tables

1. Introduction

Volcanic soils represent approximately 1 % of the world's ice-free land surface (Eswaran et al., 1993) and provide the foundation for agricultural systems that sustain at least 10 % of the global population (Shoji et al., 1993). Their unique physical and chemical properties make them particularly favourable for agricultural land use (Dahlgren et al., 2004). As a result, agriculture is a dominant activity in many volcanic regions worldwide.

These agriculturally valuable landscapes are also subject to a variety of volcanic hazards, among which tephra fallout is the most common and widespread (Burket et al., 1980; Newhall & Hoblitt, 2002). Tephra is a material made of volcanic rock fragments ejected during eruptions, the smallest of which are ash, measuring less than 2 millimetres in diameter (Blong, 1984). Due to their small size and low density, volcanic ash particles can be transported over hundreds to thousands of kilometres from the source, affecting downwind areas ranging from 1 km^2 to more than 1000 km^2 (Kennedy, 2023; Sparks et al., 1992). Consequently, tephra fallout affects a wide range of societal sectors including infrastructure (Wilson et al., 2014), public health (Horwell & Baxter, 2006), aviation (Durant et al., 2010) and agriculture (Neild et al., 1998), even with low-magnitude eruptions (Cronin et al., 1998). Within the agricultural sector, crops are generally more vulnerable to the impact of volcanic tephra fall than other farm assets (Wilson & Kaye, 2007).

Although tephra fall impacts on agriculture can be severe and long-lasting (Wilson et al., 2011), the implementation of targeted preparedness measures can substantially reduce the level of disruption (Wilson & Cole, 2007). To support the adoption of such strategies, there is a critical need for reliable risk models that integrate the components of hazard, exposure and vulnerability, thereby enabling the spatial and temporal prioritization of mitigation actions (Smith, 2013).

Crop impacts from tephra fall are primarily driven by hazard severity, with tephra mass load identified as the most influential hazard intensity metric (HIM) (Rosi et al., 1993). The amount of tephra that a volcano can eject during an eruption is estimated either through field measurements or through simulations. To date, advances have been achieved in tephra hazard modelling, including the development of numerical models like TEPHRA2 and FALL3D, which resolve advection-diffusion-sedimentation processes in a probabilistic framework (Bonadonna, Connor, Houghton, Connor, Byrne, Laing, & Hincks, 2005). However, efforts to translate hazard simulations into quantitative risk models of agricultural loss from volcanic tephra fall have been limited. While the general nature of agricultural impacts is now qualitatively well understood (Cronin et al., 1998; Jenkins et al., 2015; Wilson et al., 2011), only a few studies have attempted to link tephra load to crop damage using empirical relationships derived from post-event assessments and expert judgment (Craig et al., 2021; Wilson & Kaye, 2007). These models, however, are often overly simplistic and subject to considerable uncertainty (Ligot, De Tornaco, et al., 2024).

Even rarer are studies that combine all components of risk to perform a quantitative spatial and temporal risk assessment of crop losses from volcanic tephra fall. The work of Thompson et al., (2017) constitutes one of the few examples, carried out at the scale of dairy and fruit farms.

The objectives of this study are therefore to:

1. Conduct a quantitative spatial and temporal risk assessment of crop yield losses from volcanic tephra fall in the agricultural areas surrounding Mount Etna.
2. Perform this assessment using two models with different hazard assessments: (i) a probabilistic aggregation of tephra deposits that does not account for wind seasonality, and (ii) biweekly mean tephra deposits that explicitly incorporate wind seasonality.
3. Apply both models to two eruptive scenarios of different magnitudes (VEI 2 and VEI 3).
4. Identify how risk components translate into the spatial and temporal patterns of agricultural yield loss.
5. Identify the seasons and agricultural areas most at risk.

2. Literature Review

2.1. Volcanic agriculture: context and issues

In volcanically-active regions, agriculture is generally the main sector of economic activity (FAO, 2021) and is driven by high fertility of volcanic soils (Shoji et al., 1993).

In 2015, around 800 million people lived within the first hundred kilometres around an active volcano (Figure 1) (Brown et al., 2015). This population is projected to grow due to increased agriculture on volcanic soils and expanding urbanization (Small & Naumann, 2001).

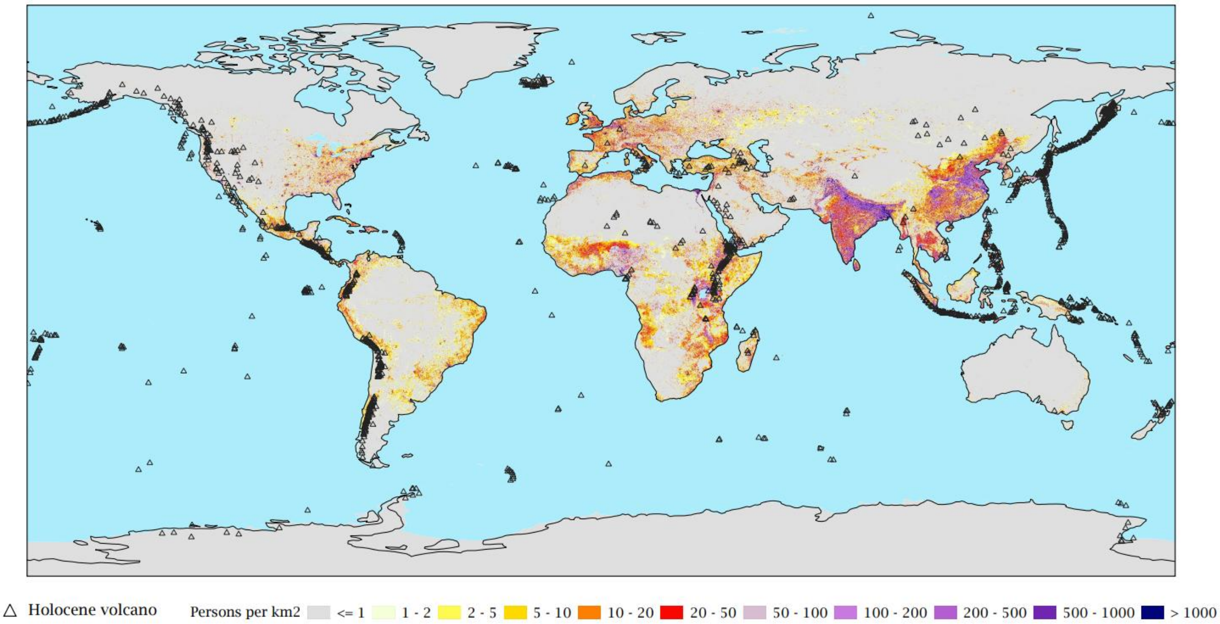

Figure 1. Holocene volcanoes and global spatial distribution of population density (Calipsa, in preparation)

The fertility of volcanic soils results from the weathering of tephra, which provides readily available plant nutrients (Ca, S, K and P) (Dahlgren et al., 2004) and allows organic matter stabilization and good aggregation, leading to adequate water retention and high hydraulic conductivity (Dahlgren et al., 2004; Shoji et al., 1993).

While volcanic soils provide agricultural advantages, agricultural systems and associated population remain exposed to volcanic hazards when located near active volcanoes (Tilling, 2005). The Food and Agriculture Organization estimates that 30% of the total damage and losses from volcanic eruptions are borne by agriculture and its subsectors, including crops, livestock, forestry, fisheries and aquaculture (FAO, 2021). Between 2005 and 2015, volcanic disasters globally resulted in 463 fatalities and impacted over 2.3 million individuals, incurring economic losses exceeding one billion USD (EM-DAT, 2017). Tephra accumulation on crops is the leading cause of agriculture-related losses from volcanic eruptions (Figure 2) (FAO, 2018).

Figure 2. Tephra from Mount Sinabung covering farmer's field, 2014 (Fiantis & Minasny, 2017).

2.2. Tephra: the most widespread volcanic hazard

A volcanic event results from a near-surface or surface magma movement, releasing energy (Fisher, 1997). Volcanic hazards can take many different forms: tephra, lava flows, volcanic gases, pyroclastic flows, lahars, landslides and earthquakes that can even trigger tsunamis. These hazards can occur simultaneously or not, with variable spatial extents and intensities (Blong, 1984). The type of eruption significantly depends on magma viscosity and ascent rate. Gas bubbles formed due to reduced pressure within the volcanic conduit and trapped within magma can be released either passively or explosively during eruptions, leading to effusive or explosive events, respectively. Conversely, explosive eruptions occur when gas bubbles fragment the ascending magma and burst explosively at the vent. Volcanic eruptions produce an eruptive column composed of hot gases and tephra, often injected high into the atmosphere (Carey & Bursik, 2015; Carey & Sparks, 1986). This eruptive column can extend hundreds of kilometres, depending on the eruption's magnitude and prevailing wind conditions. Depending on the Volcanic Explosivity Index (VEI), a scale designed to quantify the explosiveness of volcanic eruptions proposed by Newhall and Self (1982), substantial volumes of tephra can be produced. These volumes range from approximately 10^6 to 10^{12} m^3 for eruptions with VEI values between 2 and 8 (Newhall & Self, 1982).

Tephra particles are classified by diameter : volcanic bombs and blocks (>64 mm), lapilli (64–2 mm) and volcanic ash (<2mm) (Figure 3) (Blong, 1984). In everyday language, tephra fall is commonly referred to as volcanic ash fall.

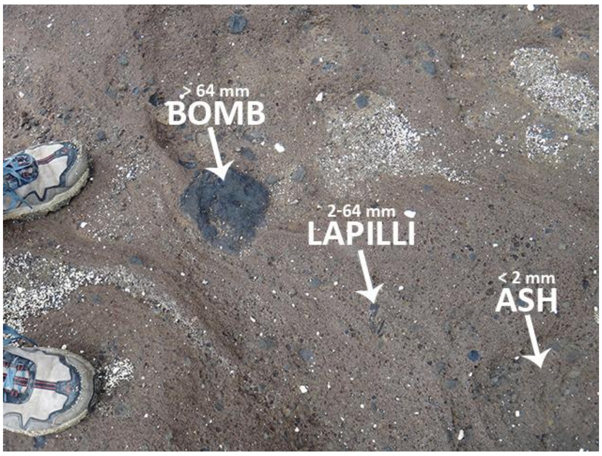

Figure 3. Photo of tephra categories depending on particle size: bomb, lapilli and ash. Photo: C. Cameron

Most documented volcanic eruptions typically persist from one to six months (Siebert et al., 2011). That being said, eruption durations can vary widely, ranging from brief bursts lasting mere minutes (such as at Tongariro in New Zealand; (Scott & Potter, 2014)) to sustained volcanic activity spanning decades (as observed at Soufrière Hills in Montserrat; (Wadge et al., 2014)) or even extending over centuries (for instance, Kilauea in Hawai'i; (Heliker, 2003)). As illustrated by the 1995/96 Ruapehu eruptions, even minor eruptions can pose a threat to the agricultural sector (Cronin et al., 1998)

The consequences of tephra fall can vary significantly based on tephra accumulation intensity and the vulnerability of affected areas, encompassing transportation and aviation disruptions, health issues, contamination of soil and water, agricultural losses, equipment damage, and structural failures such as roof collapses (United Nations International Strategy for Disaster Reduction Secretariat, 2015).

2.3. Tephra falls impacts on agriculture

As outlined earlier in Section 2.1, tephra deposition can have long-term beneficial effects on soil fertility, thereby enhancing agricultural productivity. On the contrary, the short-term effects of tephra deposition and accumulation can negatively impact agricultural systems. Direct impacts include degradation to crops, livestock health, farm buildings or equipment. Indirect impacts include the disruption of other related systems, including critical infrastructure or essential services on which agriculture operation is reliant. They can be transportation networks, water supply systems, and electricity (Figure 4) (Craig, 2015; Wilson & Kaye, 2007).

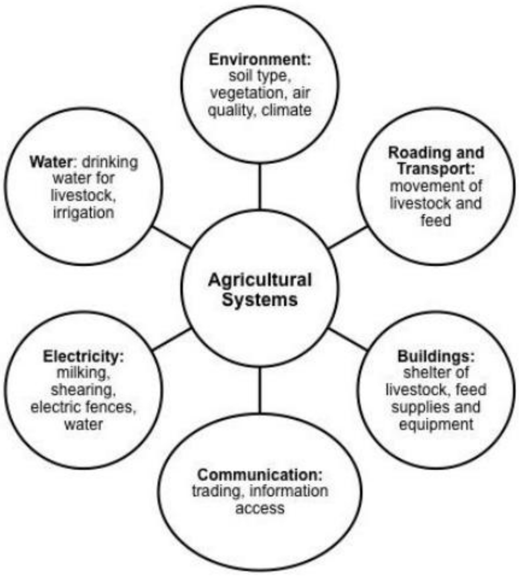

Figure 4. Diagram showing the key supporting systems of agriculture operation and production. Disruption to these components leads to increased agricultural losses (Craig, 2015).

Tephra fallout can affect multiple components of agricultural operations through various processes operating at different scales, the broadest of which is climate. Large sulphur-rich explosive eruptions have been shown to trigger global cooling, which may persist for several years and extend to non-volcanic regions, thereby threatening agriculture and food supplies (Kondo, 1988).

Regarding livestock, grazing animals are highly susceptible to ingesting significant quantities of tephra, even from thin deposition layers (Edwards et al., 2004). This can lead to digestive issues resulting in internal injuries. Tephra can be abrasive to ruminant teeth, impairing their ability to graze and potentially causing starvation (Leonard et al., 2005; Neild et al., 1998). Tephra contamination renders feed and water sources unsuitable for animal consumption (Wilson, 2009). Without external provision of feed and water, animals face the risk of mortality due to both starvation and dehydration.

Tephra deposition can affect soil permeability and temperature. For instance, smaller ash particles can obstruct pore spaces and drainage channels, reducing water infiltration, whereas coarser tephra allows for high infiltration rates exceeding those of the underlying soil (Diaz et al., 2005). Depending on tephra colour, it can either increase or decrease soil temperature through its effect on albedo, disturbing the root system (Cook et al., 1981; Smith et al., 2009). Tephra deposit on soil can limit plant growth by altering the soil's radiation regime or by physically preventing seedling emergence, especially if humidity encrusts the deposit (Blong, 1984).

Although volcanic hazards can disrupt agricultural systems in many ways, the accumulation of tephra on crops is the main and most frequent volcanic hazard responsible for agricultural damage, occurring in more than 90% eruptions (Burket et al., 1980; Newhall & Hoblitt, 2002;

Tampubolon et al., 2018). Consequently, this work will focus on the risk posed by tephra fallout to crop production.

2.4. Tephra falls impacts on crops

Tephra deposition on crops can reduce marketable yield through degradation of produce appearance and external quality, as well as by disrupting plant physiology and consequently biomass production (Ligot, Delmelle, et al., 2022). Plants exposed to tephra fallout may experience a spectrum of damage, depending on the physical and chemical properties of the tephra, although physical impacts are the most significant (Craig, 2015). Indeed, numerous case studies indicate that severe chemical impacts typically necessitate specific agricultural, volcanic, and climatic conditions.

Typical physical impacts include coverage and smothering of plants, leading to an inhibition of photosynthesis and gas exchanges, depending on the grain size and deposit thickness (Cook et al., 1981; Wilson et al., 2011). They also include overloading depending on the accumulated tephra weight, which can lead the plant to compensate for the downward pressure by physiologically changing, particularly at early growth stages of plant development (Macedonio & Costa, 2012). Abrasive tephra, transported by wind, can inflict mechanical damage on leaves and fruits, thereby creating entry points for pathogens and exacerbating water loss, leading to desiccation (Cook et al., 1981; Griggs, 1919; Wilson et al., 2011). This phenomenon can be extended temporally through wind-driven tephra remobilization (Murata et al., 1966) and can eventually lead to premature defoliation as a consequence of premature leaf abscission, a plant response to foliar wounding (Black & Mack, 1984).

Figure 5. Corn crops covered in tephra following the eruption of Tungurahua in Ecuador in 2007. Photo: R. Patricio.

Heavy tephra falls (> 100 mm) have severe consequences for nearly all aspects of farming, including crops, livestock and operations, often resulting in the complete burial of vegetation (Eggler, 1948; Griggs, 1919; Wilson & Kaye, 2007). Even more moderate accumulations of a few centimetres can smother plants and mechanically damage aerial structures such as leaves, twigs and stems (Ayris & Delmelle, 2012). As tephra thickness decreases, the overall impact becomes increasingly governed by secondary factors, such as grain size, plant morphology and environmental conditions, rather than the deposit thickness alone (Ligot, De Tornaco, et al., 2024). Accordingly, smaller amounts of tephra can still affect agricultural systems in various ways and with variable severity and even low-magnitude eruptions may inflict damage on the farming sector.

2.5. Risk assessment

In the face of volcanic hazards, risk assessments enable us to predict and quantify the potential impact they can engender on exposed assets. According to the United Nations International Strategy for Disaster Risk Reduction (UNISDR, 2009), risk assessment is "a methodology to determine the nature and extent of risk" and risk itself is defined as "the combination of the probability of an event and its negative consequences". While the public often interprets "risk" as solely the probability or chance of an event (e.g., "the risk of an accident"), technical disciplines typically define it by its potential consequences or "potential losses" within a specified cause, location and timeframe. Notably, public understanding of the significance and origins of various risks can vary considerably (UNISDR, 2009). At its core, risk is defined as a loss arising from the combination of hazard, exposure and vulnerability (Aspinall & Blong, 2015). Risk assessment quantifies the consequences of an event by combining assessments of these three components (Figure 6).

A hazard is defined as a process or phenomenon with the potential to cause loss of life, injury, other health impacts, property damage, socio-economic disruption or environmental degradation (UNISDR, 2009). Unlike other natural hazards, volcanic hazards exhibit a complex array of properties that can lead to diverse disruptions and damages (Wilson et al., 2014) (Figure 6). These properties are collectively termed “hazard intensity metrics” (HIMs). They are measurable characteristics that directly relate to the level of impact. A hazardous event is characterized by its location, intensity or magnitude, frequency and probability.

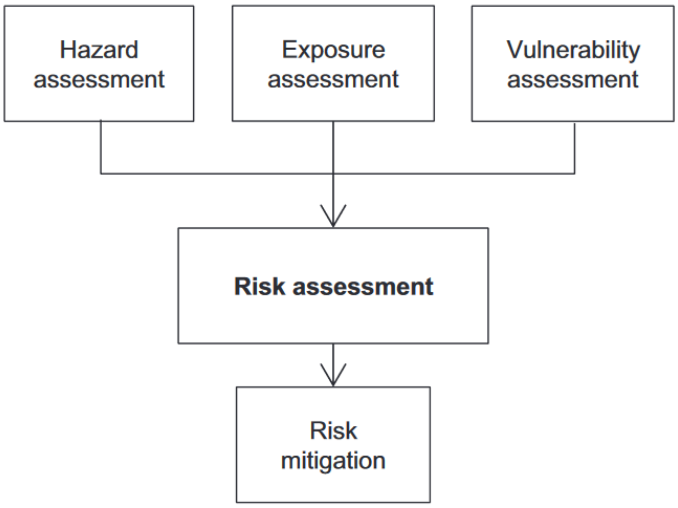

Figure 6. Diagrammatic representation of natural hazard risk assessment components and processes (Wilson et al., 2014).

Exposure refers to the physical presence of any element (e.g. crops, people, buildings or systems) within a hazard zone, thereby indicating its potential to be impacted by the hazards of interest.

Finally, vulnerability characterizes the susceptibility of an exposed element to damage from a hazard (Craig et al., 2021). Vulnerability assessments, which may be undertaken in physical, economic, and/or social contexts (UNISDR, 2009), relate the hazard intensity to the likely damage. Vulnerability characteristics (VCs) are the inherent properties of an exposed element that determine its susceptibility to the effects of a hazard.

Given the high exposure of agricultural systems to tephra fallout and its associated impacts, robust predictive models are essential to anticipate and mitigate potential damage (Craig, 2015). While it is generally accepted that increased tephra deposit thickness leads to more severe agricultural impacts (Blong, 1984), a comprehensive risk assessment requires more than simply considering hazard intensity. A holistic evaluation must also integrate different HIMs, the VCs of the affected agricultural systems and the environmental context of the impacted area (Wilson et al., 2012) (Figure 7).

One of the most challenging aspects of volcanic risk assessment stems from the multiplicity of volcanic hazards and their characteristics, which can occur in combination or be staggered over time, coupled with the complex spatial and temporal dynamics of their impacts. Furthermore, while the diversity of volcanic hazards is significant, the VCs of agricultural exposed assets are often unique yet interact within the same system and may vary considerably with time of day or season (Aspinall & Blong, 2015). Site-specific characteristics and plant-specific variables add up to tephra properties to control the level of damage to crops (Miller, 1966; Neild et al., 1998; Wilson & Kaye, 2007). To manage this inherent complexity, a common approach is to simplify the scope by focusing on a single type of hazard (e.g. tephra fall) and a specific asset category (e.g. crops).

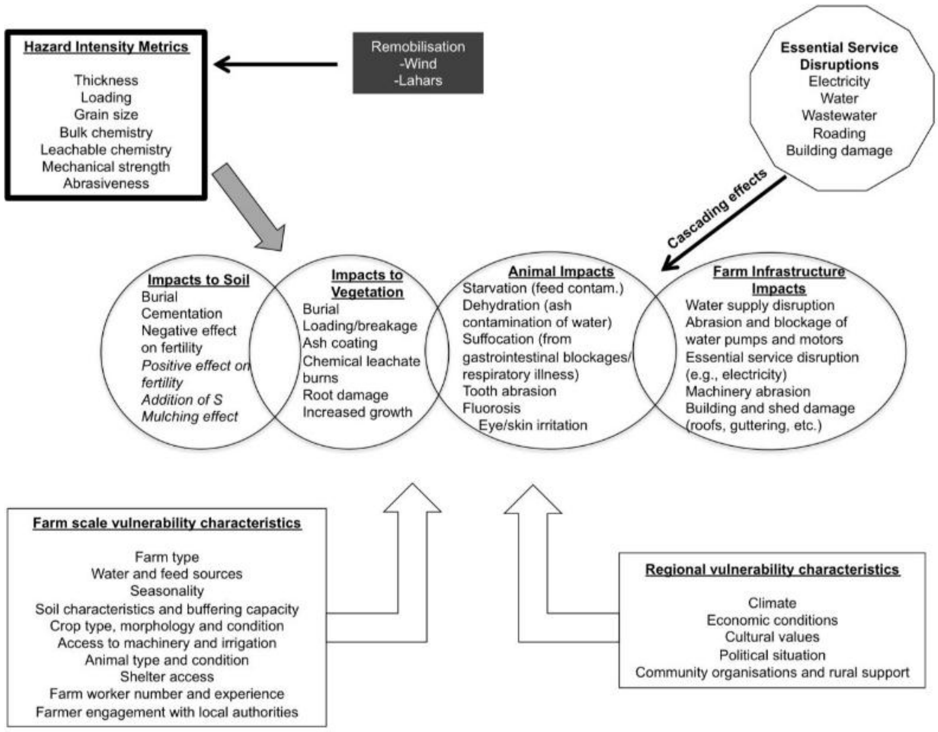

Figure 7. Diagram showing the relationship between agricultural tephra fall impacts, HIMs and VCs of agricultural systems and other related systems (Craig, 2015).

2.6. Hazard assessment

Various characteristics of tephra can pose hazards to agriculture (Cronin et al., 2003; Neild et al., 1998). Assessing this hazard relies heavily on HIMs, which are quantitative measures of tephra fallout severity. They include deposit thickness (mm), surface loading (kg/m²), grain size distribution, leachable element concentration, grain shape (abrasiveness) and colour.

For an HIM to be effective, it must meet specific criteria: a direct correlation with impact intensity, ease of measurement and reproducibility, prior quantification in post-event assessments and compatibility with analytical hazard models (Wilson & Kaye, 2007).

Tephra deposit thickness is consensually considered to be the most significant HIM for describing tephra fallout intensity and is consistently recorded in impact assessments (Craig et al., 2021; Martí et al., 2018; Rosi et al., 1993). This is because, as previously mentioned, tephra accumulation on crops is the primary driver of volcanic damage to agriculture (Burket et al., 1980; Newhall & Hoblitt, 2002). While ground thickness only approximates the tephra on plant surfaces, greater deposit thickness leads to more severe damage to crops (Ligot, Viera, et al., 2024).

Tephra falls deposition pattern

Tephra dispersal in the atmosphere and the spatial distribution of deposit on the ground depend on their tephra characteristics, atmospheric conditions and the dynamics of the volcanic plume. As a result, there's a clear relationship between the distance from the vent and the median particle size in the deposit (Pyle, 1989): larger particles fall closer to the vent while smaller particles disperse further away (Bonadonna et al., 1998; Carey & Sparks, 1986; Sparks, 1997). Tephra deposits are thickest near the eruption source and thin with increasing distance. Interactions between particles, such as aggregation and gravitational instabilities also affect how long particles stay in the atmosphere, potentially accelerating the fallout of finer ash (Bonadonna et al., 2015).

The way tephra deposits thin with distance from the volcano can be modelled using exponential, power-law or Weibull functions (Bonadonna & Houghton, 2005; Fierstein & Nathenson, 1992; Macedonio & Costa, 2012). Experts use spatially distributed field measurements of deposit thickness, tephra mass load and the maximum or mean grain size of the tephra.

Tephra dispersion modelling

Within the framework of volcanic risk assessment, the primary objective of tephra dispersion modelling is to predict HIMs both spatially and temporally. To account for the complexity of tephra deposition and dispersion process, a range of modelling approaches has been developed.

Numerical models are typically based on the advection-diffusion-sedimentation equation, which describes the transport of particles through the atmosphere under the influence of wind advection, turbulent diffusion, and gravitational settling (Folch et al., 2009). These models solve the equation comprehensively, often in three dimensions, allowing for detailed and physically realistic simulations of plume dynamics and tephra dispersion. In contrast, analytical models apply simplified versions of this equation, resulting in faster computation times but reduced spatial and physical resolution (Bonadonna, Connor, Houghton, Connor, Byrne, Laing, & Hincks, 2005; Hurst & Turner, 1999). While analytical models are particularly useful for probabilistic assessments and rapid scenario testing due to their efficiency (Biass et al., 2016), numerical models are preferred for real-time forecasting and complex terrain or wind conditions (Bonadonna & Costa, 2013). The selection of a modelling approach is typically guided by the study's objectives, the required spatial and temporal resolution, the quality of available input data and the computational resources available (Panza et al., 2011).

Three main types of tephra dispersion models can be distinguished: 1) One-dimensional analytical sedimentation models, such as those proposed by (Bursik et al., 1992; Sparks et al., 1992); 2) two-dimensional analytical models, including TEPHRAFALL and TEPHRA2 (Bonadonna, Connor, Houghton, Connor, Byrne, Laing, & Hincks, 2005; Hurst & Turner, 1999); 3) Three-dimensional numerical models, such as FALL3D (Folch et al., 2009).

The output from all tephra dispersal models is a spatial appreciation of tephra fall intensity (thickness, load or atmospheric concentration). Deterministic models simulate one or more plausible eruptive events based on known parameters, whereas probabilistic models incorporate uncertainty in input variables (e.g. erupted mass, grain-size distribution, column height, and wind profiles) to produce distributions of potential outcomes. Probabilistic modelling is particularly effective for long-term hazard assessments, where the goal is not to reproduce a specific past event but to characterize a range of possible future scenarios. They can provide tephra mass accumulation and particle size distribution results such as exceedance probability maps, probabilistic isomass and hazard curves.

2.7. Exposure assessment

Exposure assessments "identify the number, typology and location of elements (e.g. buildings, infrastructure and people) which have the potential to be impacted by the hazard(s) of interest" (Wilson et al., 2014). These evaluations can be conducted at various spatial scales, from site-specific to regional levels, typically involving a trade-off between resolution and extent. They often rely on existing datasets or more detailed information can be gathered through field surveys or remote sensing technologies (Foulser-Piggott et al., 2014).

2.8. Vulnerability assessment

VCs are the features of the affected system that determine its vulnerability to or resilience to hazards, in this case tephra fallout (Fuchs et al., 2012). These characteristics can be assessed at multiple scales, from the individual plant to the broader agrarian system. At the plant scale, vulnerability is influenced by a range of factors including morphology, phenology, and metabolism.

The overall form of a plant, referring to its architecture (such as whether it is herbaceous, shrubby, climbing, or tree-like) affects its susceptibility to burial and mechanical damage from tephra deposition. Small-stature and prostrate plants are more likely to be impacted by tephra fall compared to upright or taller species (Bosi & MIAVITA group, 2012; Craig et al., 2021). Similarly, denser canopies or complex structural architectures can enhance tephra accumulation, increasing the physical stress on the plant. While root crops production tend to be more resilient to tephra fall (Wilson et al., 2007), fruiting plants production is more vulnerable as their edible part is directly exposed, gets easily abraded by even small tephra deposits and is difficult to clean effectively (Thompson et al., 2017).

Leaf-level traits play a key role in determining crops vulnerability to tephra fall. Characteristics such as surface roughness, pubescence, shape, size, and orientation significantly influence volcanic ash retention (Miller, 1966; Sword-Daniels et al., 2011; Wilson & Kaye, 2007). Leaves with dense trichomes tend to accumulate more ash than glabrous ones, increasing shading, blocking transpiration, and promoting tissue damage (Smith & Staskawicz, 1977). Similar effects are observed in fruit: hairy-skinned varieties like kiwifruit and peaches retain more ash and are harder to clean than smooth-skinned fruits such as avocados or apples (Thompson et al., 2017; Wilson & Kaye, 2007). Furthermore, the distribution and density of stomata are crucial, as they may facilitate the absorption of acidic or saline substances dissolved in tephra, impacting plant physiology (Fernández & Eichert, 2009; Munns, 1993).

Plant phenology, the timing of life-cycle events as driven by weather and climate (e.g germination, flowering, maturation and harvest)(Lieth, 1974), is another determinant of crop vulnerability. During early growth, immature plants are particularly susceptible to burial or mechanical damage due to their low structural resistance and limited energy reserves (Bosi & MIAVITA group, 2012; Craig et al., 2021). The flowering stage represents a highly sensitive period (Blong, 1984; Craig et al., 2021; J. Neild et al., 1998), as flowers are structurally delicate and essential for reproductive success. Tephra deposited during this stage can physically damage or smother these tissues, leading to significant reductions in fruit set and eventual yield. During maturation, the development of fruits is tightly dependent on the availability of assimilates produced by the rest of the plant (Fischer et al., 2013). Therefore, any reduction in photosynthetically active foliage due to ash coverage can severely compromise fruit development and quality. Finally, the harvest stage itself is also critical. When tephra deposits onto market-ready fruits or vegetables, cleaning becomes necessary to meet commercial standards. This process can increase labor costs and reduce product value due to aesthetic damage or contamination (Barnard, 2004; Ligot, Viera, et al., 2024).

Approaches to modelling agricultural vulnerability to tephra deposition

Models of crop vulnerability to tephra fall vary in complexity, from qualitative exposure descriptions to probabilistic fragility functions, each with specific strengths and limitations. Understanding these methods is essential for selecting the most appropriate tools for scenario modelling and decision-making.

Qualitative Exposure Assessments

The simplest form of assessment, qualitative exposure assessments, consists of descriptive statements outlining the likely impacts of a hazard on exposed assets (Craig et al., 2021). While useful for rapid appraisals, these methods tend to overlook heterogeneity within asset types and do not explain the underlying mechanisms of impact.

Qualitative Vulnerability Assessments

Going a step further, qualitative vulnerability assessments aim to identify the factors that determine the vulnerability or resilience of systems (Craig et al., 2021). These factors are described qualitatively or quantitatively and ranked according to their perceived influence.

However, such rankings can be subjective and may vary across expert judgments. In agriculture, this method has helped highlight key VCs such as climate and irrigation availability following the 1991 Hudson eruption (Wilson et al., 2011).

Damage/Impact States

Damage state classifications categorize impacts into predefined levels, often combining qualitative descriptors with quantitative indicators such as damage percentage or repair costs. When they are assigned to a HIM, impact states enable predictive assessment (Craig et al., 2021). While this classification approach provides a structured framework for impact assessment, it may not capture the full complexity of real-world situations, and some impacts may not fit neatly into a single category. Furthermore, these models assume uniform vulnerability across assets, which may not reflect the diversity in agricultural system design and function. The UN-ISDR Global Assessment Report on Disaster Risk Reduction (Jenkins et al., 2015) proposed damage state classifications for agricultural systems, which were further associated with specific tephra thickness thresholds based on empirical case studies (Figure 8).

Code:			D0	D1	D2	D3	D4	D5
Description:			No damage	Disruption to harvest operations and livestock grazing of exposed feed	Minor productivity loss: less than 50 %/crop	Major productivity loss: more than 50 %/crop: Remediation required	Total crop loss: Substantial remediation required	Major rehabilitation required/ Retirement of land[7]
AGRICULTURE TYPE:	Horticulture & Arable	Ground Crops & Arable	0 mm (0-20 mm)	1 mm (0.1-50 mm)	5 mm (1-50 mm)	50 mm (1-100 mm)	100 mm (25-200 mm)	300 mm (100- 500 mm)
		Tree Crops	0 mm (0-20 mm)	1 mm (0.1-50 mm)	5 mm (1-50 mm)	50 mm (1-100 mm)	200 mm (5-500 mm)	300 mm (200- 500 mm)
	Pastoral		0 mm (0-20 mm)	3 mm (0.1-50 mm)	25 mm (1-70 mm)	60 mm (20-150 mm)	100 mm (30-200 mm)	300 mm (100- 500 mm)
	Paddies		0 mm (0-50 mm)	1 mm (0.1-50 mm)	30 mm (1-75 mm)	75 mm (20 - 300 mm)	150 mm (75 – 300 mm)	300 mm (100- 750 mm)
	Forestry		0 mm (0-75 mm)	5 mm (0.1-75 mm)	200 mm (20-300 mm)	1000 mm (100-2000 mm)	1500 mm (100->2000 mm)	?

Figure 8. Hazard-loss relationships illustrating approximate median and interdecile dry ash thickness (HIM) associated with critical levels of agricultural productivity loss across various crop types. Derived from expert judgment and scarce empirical/experimental data, these relationships assume a worst-case scenario in crops in growing stage; seasonal modifiers can adjust impacts for other growth periods. These estimations are intended as broad guidelines and necessitate refinement for specific regional and crop conditions (Jenkins et al., 2015).

Fragility Functions

Fragility functions are generally considered as the most robust tool to represent vulnerability (Craig et al., 2021). These functions can take two forms: (1) deterministic functions that express damage or loss as a function of hazard intensity, and (2) probabilistic functions that estimate the probability of a damage state being reached or exceeded when a hazard intensity occurs (Craig et al., 2021).

The first category quantitatively links the HIM to measurable outcomes such as physical damage, loss of function, or economic loss (Craig et al., 2021). These functions may be limited by their dependence on a single HIM, which does not always capture the complexity of multi-dimensional impacts. For example, Wilson & Kaye (2007) developed vulnerability functions for the New Zealand agricultural sector, correlating tephra deposit thickness with damage ratios across different types of farming systems (Figure 9).

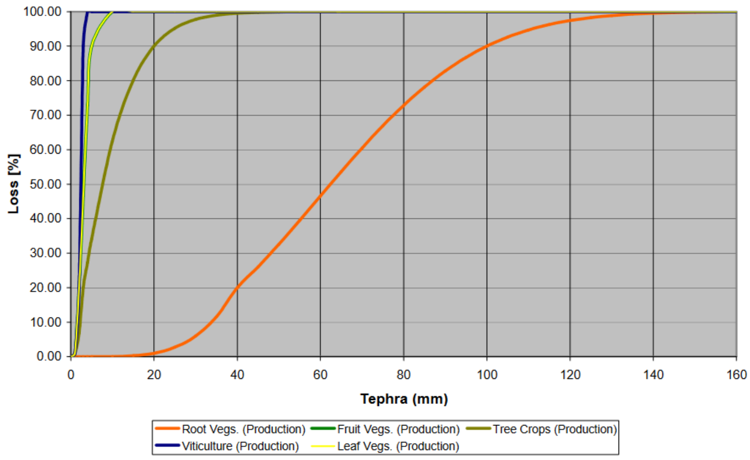

Figure 9. Fragility functions for horticultural farming, linking tephra deposit thickness (mm) to production loss (%) (Wilson & Kaye, 2007).

The creation of such functions requires large empirical datasets. Post-event impact assessments (post-EIAs) are commonly employed to collect data on hazard effects, tephra characteristics, and crop vulnerability, which in turn inform the development of vulnerability and risk analysis models (Craig et al., 2016, 2021; Wilson et al., 2014). However, the hazardous, unpredictable, and often remote nature of volcanic eruptions, combined with the relatively recent emergence of volcanic impact science, has resulted in a paucity of empirical data concerning crop vulnerability to tephra and frequently an incomplete characterization of post-eruption tephra properties. To address this data scarcity, a key strategy has been the extensive reliance on expert judgment (Wilson & Kaye, 2007) and the use of impact states, which forms the basis for a second category of vulnerability functions.

The second category comprises probabilistic fragility functions, which are designed to represent the probability that a given damage state will be reached or exceeded as hazard intensity increases (Craig et al., 2021). These functions are especially useful in risk assessments where uncertainty is inherent, such as early warning systems and scenario-based planning. However, their reliability depends heavily on the availability of robust and representative datasets. In this context, Craig et al. (2021) proposed a set of fragility functions for estimating the probability of crops reaching or exceeding different damage states, depending on the thickness of the tephra. They are presented and reviewed in Section 8.2.

Given that morphological and phenological characteristics are key determinants of crop vulnerability (Ligot, Viera, et al., 2024), fragility functions are typically developed for each crop category and individually constructed for each phenological stage. Crops can be classified based on the harvested or edible plant part (Wilson & Kaye, 2007), on specific plant traits such as architecture or growth form (Bosi & MIAVITA group, 2012; Jenkins et al., 2015), or through a combined classification integrating both structural traits and harvestable components (Craig et al., 2021).

Limitations

Although significant progress has been made in modelling tephra fall hazards (Bonadonna, Connor, Houghton, Connor, Byrne, Laing, & Hincks, 2005), and the impacts of tephra fall on agriculture are generally well understood qualitatively (Cronin et al., 1998; Jenkins et al., 2015; Jenkins et al., 2014; Wilson et al., 2011), the development of fully integrated, quantitative risk models remains limited. This is largely due to the scarcity of robust impact and vulnerability datasets specific to agricultural systems (Jenkins et al., 2014). Several studies have proposed models that relate tephra thickness or mass loading (kg/m^2) to agricultural impacts, often derived from post-event assessments and expert judgment. However, these models are widely recognized as simplistic and subject to considerable uncertainty, primarily due to three factors: the scarcity of observational data, the oversimplification of vulnerability, typically reduced to crop type and phenological stage, and the exclusive use of ash thickness as the sole HIM (Ligot, Bogaert, et al., 2023).

2.9. Risk assessment applications

Agricultural risk assessments are valuable tools both before and after a volcanic event (Craig, 2015) (Figure 10). Prior to an eruption, they support preparedness planning by anticipating potential losses and guiding community-level recommendations, including land-use decisions. In agricultural settings, they contribute to reducing exposure and vulnerability by informing crop selection, spatial distribution, rotation schemes, and adaptive farming practices (Wilson & Cole, 2007).

Following an eruption, risk assessments are also useful in shaping both emergency response and long-term recovery strategies (Craig, 2015). They enable efficient resource allocation, prioritization of interventions and development of tailored mitigation actions. Access to precise and detailed data on impact severity and spatial extent is essential for designing effective responses and minimizing adverse outcomes (Blaikie, 1994).

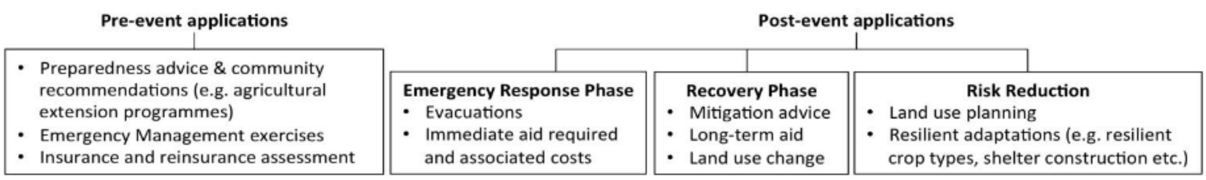

Figure 10. Diagram showing the pre- and post-event applications of risk assessment. Adapted from Craig, (2015).

From the perspective of agricultural insurance, pre-event risk analyses assist providers in quantifying the exposure and vulnerability of particular agricultural systems or regions, directly influencing premium calculations, contract conditions, and coverage eligibility (Niño et al., 2015). More accurate, spatially explicit pre-event risk models allow insurers to tailor their products according to real levels of agricultural risk, enhancing fairness and efficiency.

Following a hazard, post-event risk assessments become essential for accurately estimating agricultural losses and triggering compensation mechanisms. Within the European Union context, indemnities typically rely on farm-level observations or meteorological indices, providing a robust basis for claim verification and payout calculations (ECORYS. & Wageningen Economic Research., 2017). These assessments also guide the disbursement of public disaster aid when private mechanisms are insufficient, contributing to more effective financial recovery. The integration of both pre- and post-event risk evaluations enhances the overall sustainability of insurance systems by improving loss forecasting and reserve planning.

In Italy, agricultural insurance schemes have shown variable efficiency depending on the accuracy and granularity of risk assessments used. Capitanio and De Pin (2018) emphasize that insurance performance and cost-benefit ratios improve significantly when risk mapping is incorporated into the underwriting and claim processes, particularly for spatially heterogeneous hazards such as drought or frost (Capitanio & De Pin, 2018). However, tephra hazard remains poorly integrated in such frameworks, highlighting a key gap in the agricultural insurance landscape.

2.10. Gap of knowledge

Despite the development of increasingly sophisticated spatial and temporal risk assessment models for agricultural losses due to hazards such as drought (Carrão et al., 2016) or floods (Winsemius et al., 2016), equivalent frameworks for tephra fallout remain largely absent. As mentioned before, predictive tools integrating tephra intensity, crop sensitivity and seasonal timing into spatial damage assessments are lacking. This absence impedes preparedness planning, insurance pricing accuracy, and post-disaster compensation.

3. Case study of Mount Etna

3.1. A highly active and well-documented volcano in the Mediterranean region

Mount Etna, located in eastern Sicily (37.748°N, 14.999°E) (Figure 11), is the highest and largest active volcano in Europe, rising to an elevation of 3,357 meters above sea level (a.s.l.) and covering an area of approximately 1,200 km² (Branca & Del Carlo, 2004; Smithsonian Institution, 2025). Around one million people live within 30 kilometers of the volcano (Smithsonian Institution, 2025). The nearest city is Catania, the second most populous city on the island with a population of 310,000 inhabitants. It is located 35 km south-south-east of the volcano. (ISTAT, 2024). Etna's eruptive activity is among the most extensively documented in the world, with continuous records dating back to around 5000 BCE (Smithsonian Institution, 2025).

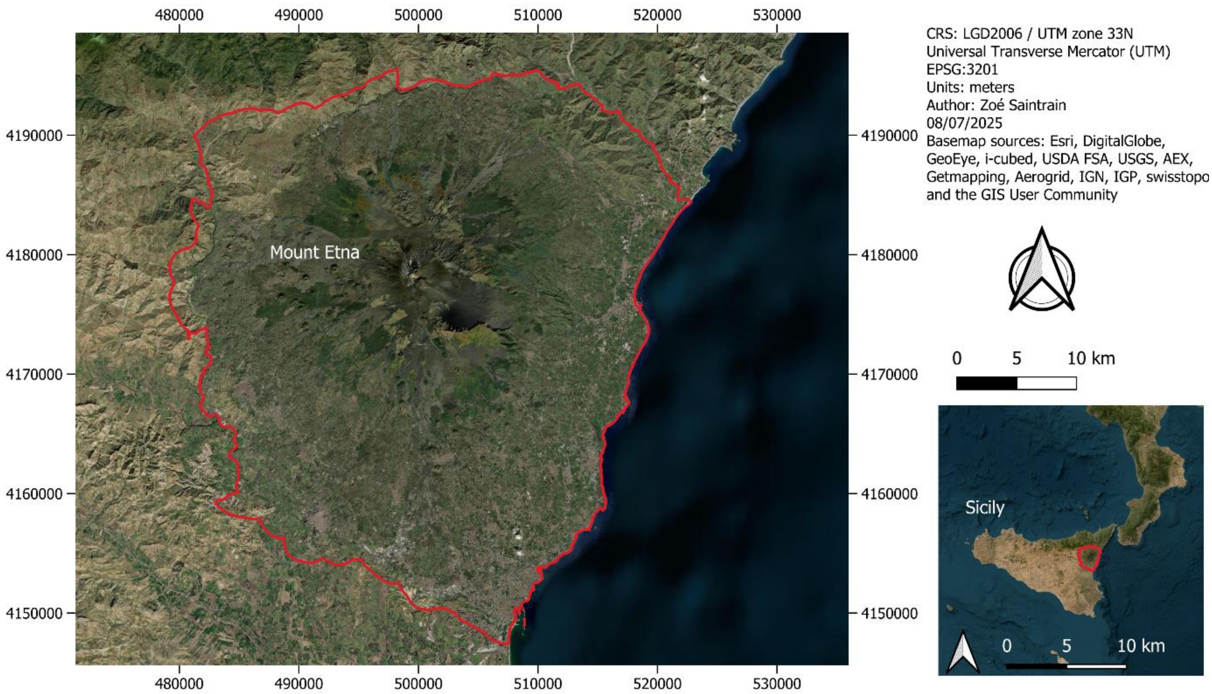

Figure 11. Geographical context of the study area (Signorello et al., 2020).

Mount Etna holds both scientific and cultural significance. Inhabited since prehistoric times due to its central location in the Mediterranean, it has become one of the most studied and renowned volcanoes globally. The interrelation between human settlements and the volcanic environment has been continuous since the Neolithic era. The favourable climatic, hydrological and pedological conditions of the Mount Etna's lower slopes (also known as the "mountain foot region" (0-1000 m a.s.l.)), combined with its strategic position at the crossroads between the Tyrrhenian and Hyblean regions, have supported the development of complex socio-cultural systems throughout history (Soldati & Marchetti, 2017). Owing to its exceptional geological, volcanological and geomorphological features, Mount Etna was inscribed on the UNESCO

World Heritage List in June 2013, further cementing its global scientific and cultural relevance (UNESCO, 2013).

3.2. Beyond lava: explosive activity and tephra emissions

Mount Etna is one of the most active volcanoes in the world, exhibiting nearly continuous eruptive behaviour (Coltelli et al., 1998). While Etna was historically classified as an effusive volcano, primarily producing lava flows that, although destructive to infrastructure, posed limited direct threats to human life, recent studies have revealed its capacity for highly explosive events, such as the Plinian eruption of 122 BCE (Coltelli et al., 1998) . Explosive activity at Mount Etna was long considered secondary to lava effusion; however, it has become increasingly frequent in recent decades (Osservatorio Etneo, n.d.; Scollo et al., 2009).

Etna's volcanic activity ranges from mild strombolian eruptions to more intense sub-Plinian events (Scollo et al., 2009). Strombolian activity, the most frequent eruptive style at Etna and other basaltic volcanoes such as Stromboli and Hawaiian volcanoes, involves lava flows and the ejection of tephra plumes that persist from hours to months and typically reach heights from several meters to hundreds of meters (Osservatorio Etneo, n.d.; Scollo et al., 2009). Sub-Plinian phases, though less frequent, are characterized by the emission of larger tephra plumes, which may reach altitudes near the tropopause and typically last from several minutes to a few hours.

Since 1990, over 150 violent explosive episodes have been recorded from summit and from fissures along the volcano's flanks (Branca & Carlo, 2005). These events have produced eruptive columns reaching 5 to 15 km above sea level and ejected tephra volumes ranging from 10^4 to 10^7 m^3 (Scollo et al., 2009). More than 70 flank eruptions have occurred over the past 420 years (Branca & Del Carlo, 2004). They are typically less frequent than summit eruptions but can last from a few hours to over a year (e.g., 1991-1993, 472 days; 2008-2009, 419 days) (Osservatorio Etneo, s. d.; Signorello et al., 2020).

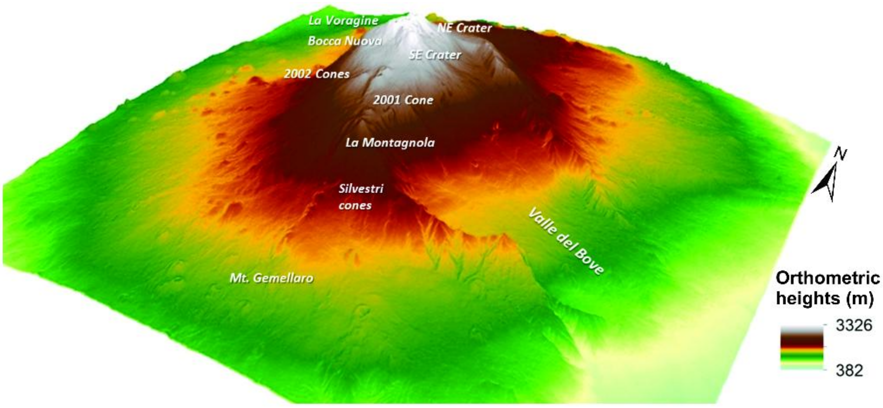

Figure 12. Digital surface model of Mount Etna from Pleiades satellite data in 3D perspective view (Palaseanu-Lovejoy et al., 2019). The eastern slope reveals the Valle del Bove, a vast depression formed by major landslides, which is now a primary accumulation are primary accumulation area for volcanic deposits (Soldati & Marchetti, 2017).

The 2002-2003 Eruption: A Case of Etna’s Explosive Potential

Among the most impactful recent events, the 2002-2003 flank eruption exemplifies the increasing explosivity of Etna. Originating from a fracture on the upper southeast flank (at 2750 m a.s.l.), it was characterized by continuous weak plumes reaching heights of 2.5 to 7 km and substantial tephra fallout over eastern Sicily (Figure 13) (Andronico et al., 2005, 2008) . The eruption involved both lava effusion and violent strombolian activity lasting several weeks, producing large quantities of tephra (Osservatorio Etneo, n.d.; Scollo et al., 2013).

The eruption had significant socioeconomic consequences. Approximately 80% of regional crops were damaged, numerous buildings sustained structural damage and transport systems were severely disrupted (Barnard, 2004; Scollo et al., 2013). Roads were covered in ash, reducing visibility and causing accidents, while Catania and Reggio Calabria airports were closed for several weeks. Alongside the 122 BCE Plinian eruption, the 2002-2003 event is considered one of the most disruptive in terms of impact on infrastructure and agriculture.

Figure 13. Eruption column produced during the activity of November 2002. Photo taken during the monitoring activity of INGV-CT (Scollo et al., 2013).

The Central Role of Agriculture in the Etna region’s landscape and economy

Mount Etna is not only the most active and a well-documented volcano in Europe, it is also a region where agricultural activity constitutes one of the prevailing economic sectors (Petino & Privitera, 2023), as in the rest of Sicily. In 2022, the sector employed 7.6% of the regional workforce, a proportion higher than in southern Italy (6.7%) and the national average (3.4%) (CREA, 2024a). Sicily also has the highest number of active agricultural enterprises among Italian regions, representing 11% of the national total. The region’s Utilized Agricultural Area (UAA) amounts to 1.3 million hectares, corresponding to 52% of Sicily’s total land area and 11% of the national UAA. In terms of economic output, the added value of the agricultural sector reached €3.8 billion in 2022, accounting for 4.4% of the region's total added value, a figure higher than the national average of 2.2%. These figures underline the deep-rooted agricultural identity of the region and its strong economic dependence on the primary sector.

On the slopes of Mount Etna, despite continuous cultivation since antiquity, agricultural activity has been maintained without major soil erosion or significant yield reduction (Soldati & Marchetti, 2017). Signorello et al. (2020) characterized land use within the territory of Mount Etna and produced a detailed land cover spatial distribution (Figure 14). According to these data, natural and semi-natural areas (mainly forests and shrublands) occupy approximately 35% of the study area and are predominant above 1,000 meters above sea level. Artificial surfaces account for around 10% of the territory, mostly concentrated in the south-eastern sector below 700 m a.s.l. Agricultural areas represent about 43% of the total land use and prevail below 1000 m a.s.l., amounting to approximately 57,000 hectares. These agricultural zones include both intensive crop systems and complex agroforestry mosaics.

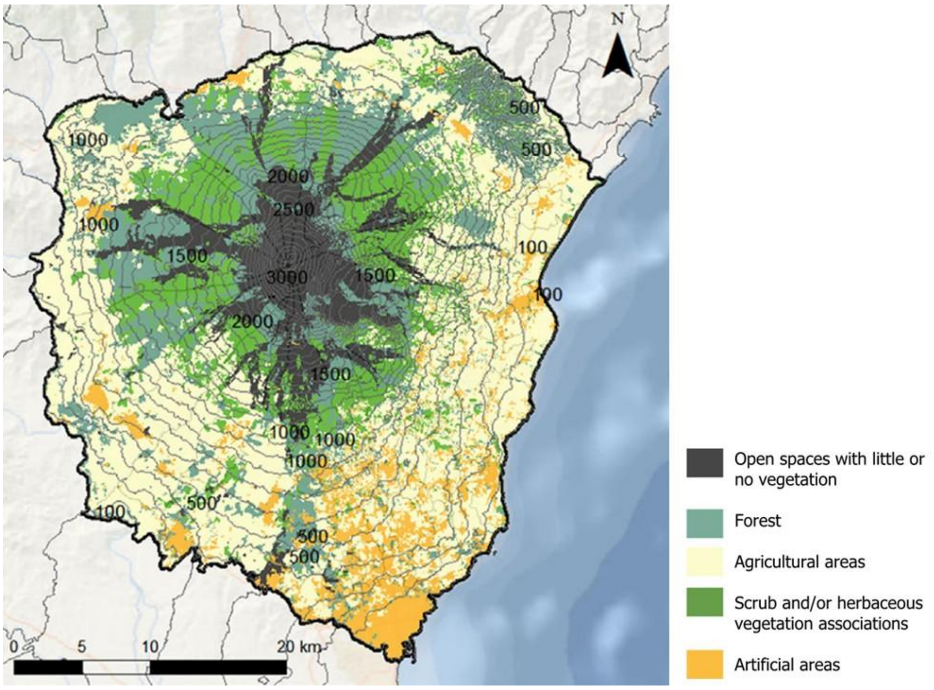

Figure 14. Land use/Land cover on Mount Etna (Signorello et al., 2020).

Climatic conditions on Mount Etna change with altitude, going from subtropical at lower levels to cold at higher altitudes, through temperate (Chester et al., 1985). While average annual temperatures at the coast are approximately 18 °C, they decline rapidly with height and heavy snowfall is common on the mountain's upper slopes. Significant temperature contrasts exist across the volcano's different sectors, with warmer conditions found in the northern, northwestern and western areas due to the exposure to the Ionian Sea (Soldati & Marchetti, 2017). Precipitation has a sharp seasonal variability being generally concentrated in the period October-April (Aiuppa et al., 2003). A persistent volcanic plume is deflected by predominantly westerly winds causing rainfall enhancement over the eastern and southeastern sectors (Soldati & Marchetti, 2017).

Land use and crop type distribution reflect a nuanced adaptation to environmental gradients and economic factors across the volcano's altitudinal and spatial sectors (Soldati & Marchetti, 2017). As noted by Dazzi (2007), three primary agro-ecological zones can be identified on Etna's flanks. Lower slopes range from 0 to 400 meters a.s.l. and are dominated by citrus groves and vineyards. The intermediate zone, from 400 to 800 meters a.s.l, is characterized by the cultivation of olives, cherries, peaches, figs and wheat. The upper slopes, between 800 and 1300 meters a.sl., are mainly used for grazing, along with niche crops such as hazelnuts and prickly pears.

Within these altitudinal zones, the types of crops and cultivars cultivated differ across the various flanks of Mount Etna, reflecting the influence of microclimatic conditions, soil variability and sun exposure. The northern slope is characterized by its gentle gradients and is favored by producers for its wider thermal range and relatively harsh climate, which benefit certain crops. The eastern flank, more exposed to maritime air masses and precipitation, supports different cultivation profiles. The southern side experiences the highest temperatures and presents a diverse patchwork of agricultural plots, each of roughly equal economic weight (Petino & Privitera, 2023).

In 2019, the estimated gross annual value of agricultural production on the volcano's slopes was €376 million (CREA, 2020). This figure highlights the economic significance of agriculture in the Etna region, not only in terms of output but also as a critical component of local livelihoods. Pollinator-dependent crops (such as vegetables, citrus, orchards, prickly pear, olive trees, and vineyards) covered around 45,000 hectares and accounted for €323 million of this total, highlighting their critical role in the region's agricultural economy (CREA, 2020; Signorello et al., 2020).

Signorello et al. (2020) characterized the spatial distribution of the "land use for pollination service" around Mount Etna. This work represents the most recent study to date on the spatial distribution of agricultural crops in the region (Figure 15). It will therefore be used as the reference in the present work to determine the geographic location of crops for which agricultural loss risk is assessed. Within the agricultural land use classification, Signorello et al. (2020) reports several crops: "prickly pear/olive tree", "prickly pear", "hazelnuts", "pistachios", "olive trees", "citrus", "grains", "vineyards", "irrigated crops", and "orchards".

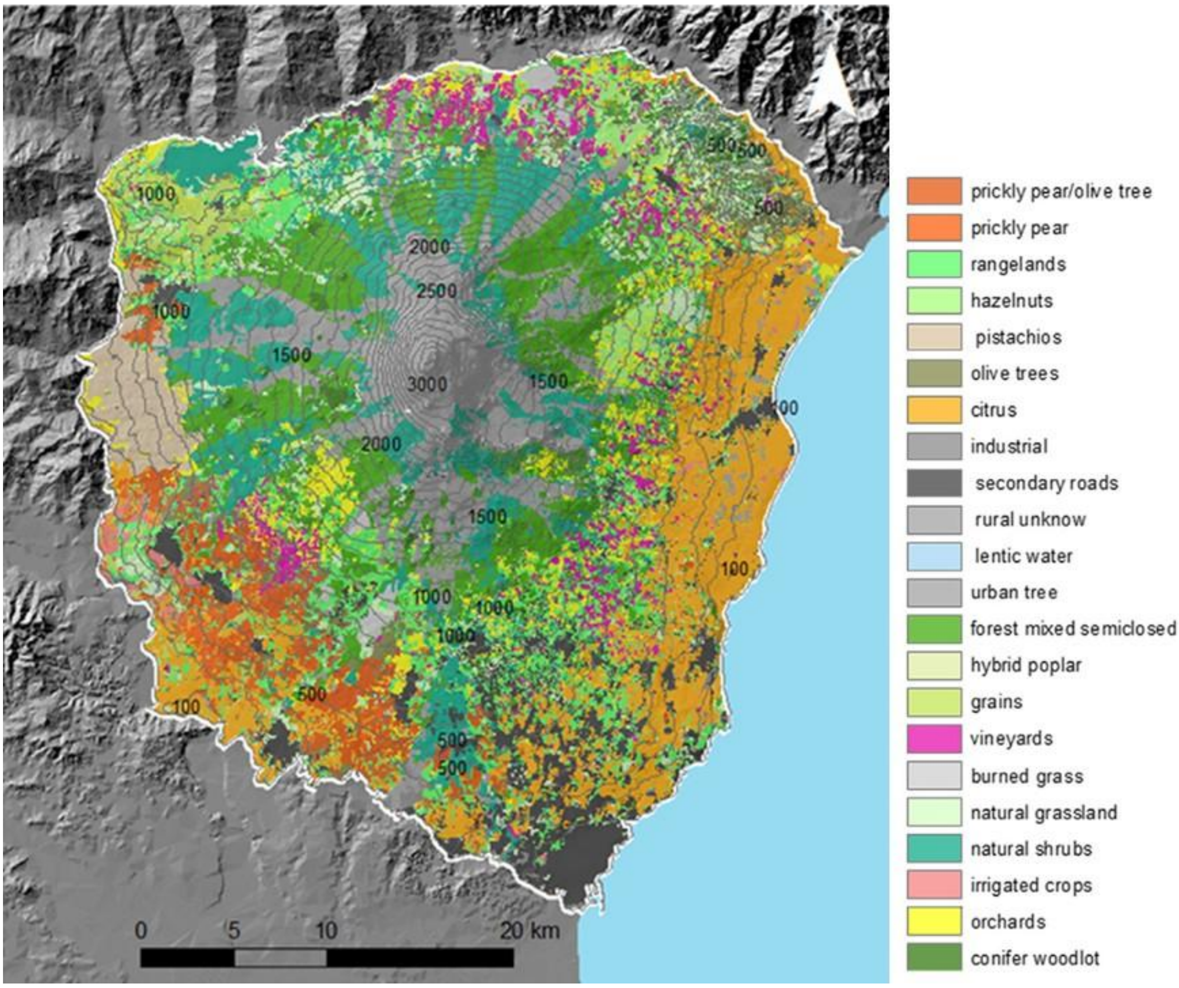

Figure 15. Land use for pollination service spatial distribution on Mount Etna (Signorello et al., 2020).

Although citrus crops account for a substantial portion of the agricultural land, the gross economic value of its production constitutes only 2.5% of the total gross value of the Etnean agricultural production. This discrepancy is primarily explained by two factors. First, the market prices of citrus, especially Etna lemons, have remained persistently low in recent years, often falling below production costs. This situation is exacerbated by competition from imported citrus products, notably from Spain, which are sold at more competitive prices due to lower labour and production costs (CREA, 2024; ISMEA, 2020). As a result, although citrus volumes are substantial, the local value added is limited. Second, the economic yield of citrus cultivation is lower compared to other Etnean crops. High-value crops such as wine grapes, pistachios and apples have significantly higher market prices and are better positioned in export and quality-driven market channels (CREA, 2024; Petino & Privitera, 2023). These crops, though sometimes occupying smaller areas, generate disproportionately higher gross production values than citrus.

Crop	Proportion of the Etnean agricultural area (%)	Proportion of the gross value of Etnean agricultural production (%)
Citrus	36.4	2.5
Orchards	13.6	14.3
Prickly pear and olive	8.5	1.6
Olive	8.3	48.3
Vineyards	8.2	11.3
Grains	7.4	Not specified
Pistachios	5.6	Not specified
Hazelnuts	3.7	Not specified
Prickly pear	2.4	5.1
Irrigated crops	1.8	2.9

Table 1. Proportion of the Etnean agricultural area (%) and proportion of the gross value of the Etnean agricultural production (%) for major crops cultivated on Mount Etna. Values were calculated based on a reference total agricultural area of 57,000 hectares and a total gross value of agricultural production of €376 million (CREA, 2020; Signorello et al., 2020).

The most economically valuable crops on Mount Etna are orchards, olive trees and vineyards. According to Signorello et al. (2020), the crop type labelled “orchards” includes apple trees (*Pyrus malus* L.), pear trees (*Pyrus communis* L.) and cherry trees (*Prunus avium* L.). The study does not specify the proportional distribution of each species within the total orchard area. Olive cultivation appears under two land use categories: “olive trees” and “prickly pear and olive”. This reflects a specific land management practice on Etna, where certain plots combine both olive trees (*Olea europaea L*) and prickly pear (*Opuntia ficus-indica*) cultivation. However, prickly pears are often planted as hedgerows or protective borders around olive groves, rather than cultivated as a primary crop (Barbera et al., 1992; Dazzi, 2007). For this reason, in the present study, both categories are grouped under the single crop type “olive trees” to better reflect their shared agronomic and spatial function.

4. Materials and methodology

To quantify the spatial and temporal risk of crop yield loss around Mount Etna, several layers of information are required. Risk is defined as the combination of hazard, exposure and vulnerability of the assets threatened by the hazard (Smith, 2013). In this case study, the hazard corresponds to the potential spatial distribution of tephra fallout following an eruption. Exposure refers to the geographical location of the cultivated areas surrounding the crater. Vulnerability is defined as the yield loss experienced by crops in relation to the amount of tephra deposited on them. The temporal dimension is introduced through vulnerability, which varies according to the crops' phenological stages. These phenological stages progress over the seasons and their timing differs for each crop type based on crop-specific calendars.

The following section presents the materials and methods used to assess each of these information layers. Section 4.5 describes how these layers are combined within the risk modelling framework.

4.1. Exposure: spatial distribution of the studied crops

This research is limited to the risk assessment of crop losses for olive trees, vineyards and orchards in the event of tephra fall. These crops were selected based on their local economic importance. Together, they cover a total area of 22,000 hectares (Figure 16).

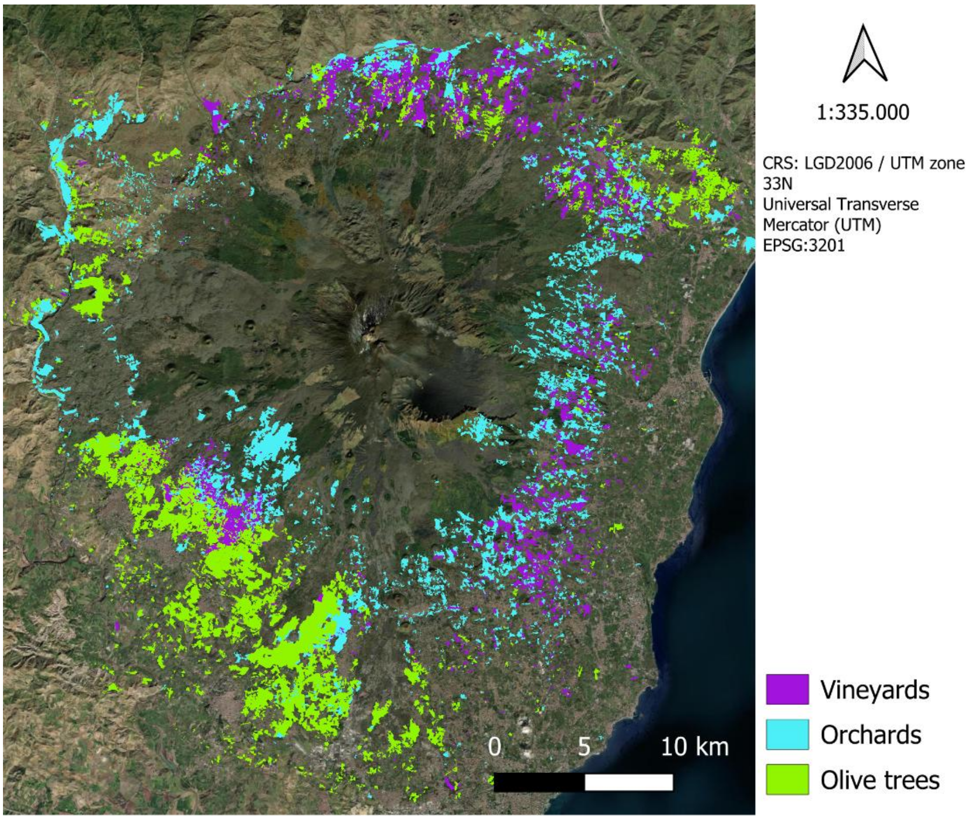

Figure 16. Spatial distribution of studied crops (Signorello et al., 2020).

The area occupied by vineyards forms a semicircular pattern that extends across nearly all flanks of the volcano but is especially concentrated along the northern, northeastern and eastern slopes. This pattern aligns with the official boundaries of the Etna DOC wine region, (Consorzio Tutela Vini Etna DOC, 2022). Orchards are also distributed around the volcano, but are most heavily concentrated along the entire eastern flank, where moderate elevations and fertile volcanic soils support fruit trees such as apples and pears (Petino & Privitera, 2023). Olive trees and prickly pear cacti (grouped here as a single crop type) are mainly distributed across the southern and southwestern sectors of the volcano, with additional scattered occurrences in the north and northeastern flanks. These species are particularly well adapted rocky soils with strong solar exposure (Barbera et al., 1992; Ferrara & Ingemark, 2023). Their occurrence at lower altitudes and in more arid microclimates highlights their resilience and suitability for cultivation in harsher conditions.

4.2. Hazard: tephra dispersion simulation

Tephra2 and TephraProb are two complementary tools particularly well suited for conducting spatial hazard assessments related to tephra fallout. Tephra2 is a semi-analytical dispersal model that estimates tephra accumulation on the ground using an analytical solution to the advection-diffusion-sedimentation equation (Bonadonna, Connor, Houghton, Connor, Byrne, Laing, Hincks, et al., 2005). TephraProb builds upon Tephra2 by embedding it within a probabilistic modelling framework. Implemented in Matlab, it enables stochastic sampling of eruptive and atmospheric parameters to account for the natural variability and uncertainty of future eruptions (Biass et al., 2016).

Running TephraProb requires three main inputs: a computational grid, wind data and an eruption scenario (Figure 17). The eruption scenario reflects the expected eruptive behaviour of a given volcano and is defined by ranges and/or distribution of eruption source parameters (ESPs) including plume height above sea level, erupted mass, duration and total grain-size distribution (TGSD). In TephraProb, TGSDs are expressed using the logarithmic φ (phi) scale, defined by

$$\varphi = -log_2(d) \tag{1}$$

where d is the particle diameter in millimetres. This transformation allows a continuous and standardized representation of a wide spectrum of particle sizes. TGSDs are further characterized by a φ range, a median φ value, a φ standard deviation and two parameters related to aggregation processes: the minimum and maximum fraction of fine particles likely to aggregate and the maximum particle diameter potentially affected by aggregation.

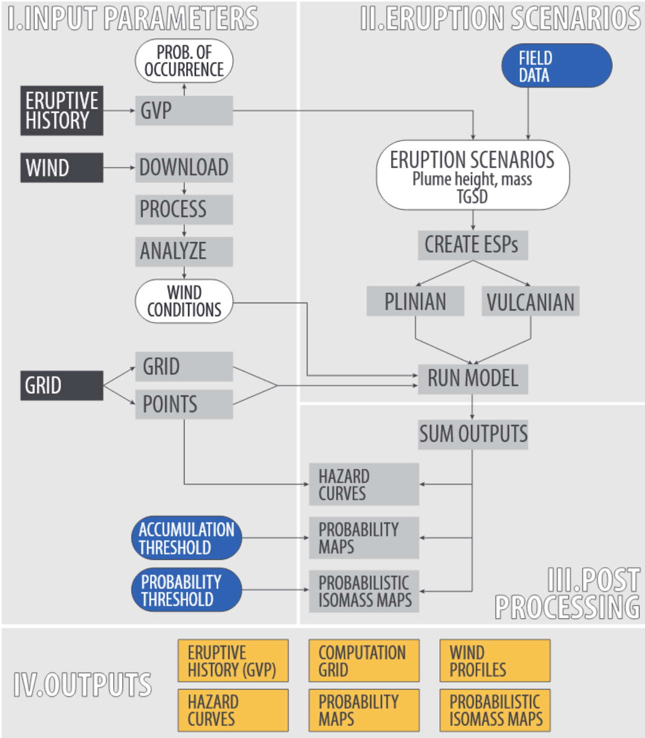

Figure 17. Overview of the TephraProb workflow, structured into four steps: input data access and pre-processing, probabilistic scenario simulation, post-processing and probabilistic outputs (Biass et al., 2016).

Eruption source parameters can be derived from the eruptive history of the volcano, field measurements or other volcanoes presenting an analogue behaviour. When the eruptive history is sufficiently comprehensive, it is possible to assign a long-term probability to the eruption scenario (Biass et al., 2016). However, this is not the case in the present study. The hazard is instead expressed as conditional upon the occurrence of a given scenario, without quantifying the probability of that scenario itself.

During a hazard assessment, a predefined number of model runs is set. For this hazard assessment, it was set to 1,000, balancing reliability against computational time. For each run, TephraProb performs a Monte Carlo sampling of both wind profiles and ESPs. Depending on the eruptive style considered (Plinian or Vulcanian), the modelling of plume dynamics and erupted mass as well as the handling of long-lasting eruptions differ accordingly. Each unique set of sampled parameters is used to run Tephra2, which simulates tephra dispersal across the domain. As a result, a set of 1000 tephra deposition outputs is produced.

These outputs are then post-processed to generate probability maps and probabilistic isomass maps. Probability maps display the spatial probability of exceeding a predefined tephra accumulation threshold (in kg/m²). Hazard curves represent the probability of exceeding any tephra accumulation at a given point, if specific locations have been defined. Probabilistic isomass maps, on the other hand, display the spatial distribution of tephra accumulation associated with specific exceedance probabilities. They represent tephra deposits that have a 10%, 25%, 50%, 75% or 90% chance of being exceeded, conditional on the eruption scenario considered.

In this study, the calculation grid was defined to match the agricultural study area surrounding Mount Etna with a resolution of 500 meters (Table 2). The wind data consists of local vertical profiles measured between 2014 and 2023, with three profiles recorded per day.

Parameter	Value
Left (Minimum Easting)	479.186, 251858
Right (Max Easting)	522.826, 251858
Bottom (Min Northing)	4.147.611, 043972
Top (Max Northing)	4.195.691, 043972
Vent easting	499474
Vent northing	4178190
Vent zone	33
Vent height	3000

Table 2. Spatial limits of the simulation domain and eruption source location used for the hazard simulations, including the coordinates of the calculation grid, the location of the eruption vent, its geographical UTM zone and its elevation above sea level. Spatial reference system: ED50 / UTM Zone 33N.

This study quantifies the risk of agricultural losses under the probable tephra fallout from two eruption scenarios capable of producing significant and widespread tephra deposition: a VEI 2 and a VEI 3 eruption (Table 3). The source parameters for these scenarios were derived from two historical basaltic eruptions at Mount Etna, namely the 2002-2003 strombolian event and the 1990 sub-Plinian event, both previously modelled by Scollo et al. (2013). The sampling distributions of the eruption source parameters for both eruption scenarios are provided in Appendix (Figure A1; Figure A2).

Eruption source parameters	VEI 2 strombolian eruption scenario	VEI 3 sub-Plinian eruption scenario
Plume height	3600 to 6000 m a.s.l	12,000 to 15,000 m a.s.l
Total erupted mass	1.5×10^{6} to 5×10^{9} kg	1×10^{10} to 4×10^{10} kg
Eruption duration	96 to 720 hours	30 min to 2 hours
Grain-size range (φ)	8 to -6	8 to -6
Median grain size (φ_{50})	-1.5 to -0.5	-1 to 0
Standard deviation ($\sigma\varphi$)	1.5 to 2	1.5 to 2
Aggregation coefficient	0.3 to 0.7	0.3 to 0.7

Table 3. VEI 2 strombolian and VEI 3 sub-Plinian eruption source parameters. Grain-size parameters are expressed in phi units (ϕ).

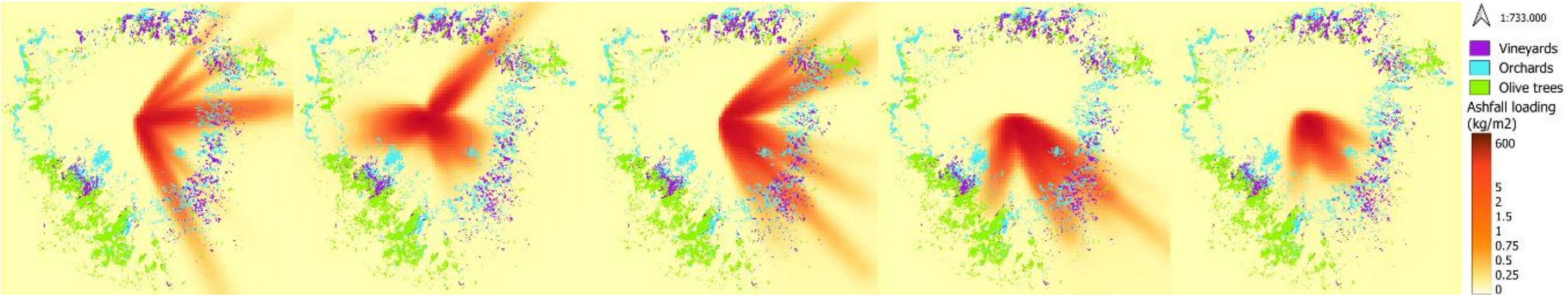

Figure 18. Five examples of ashfall loading maps (kg/m²) from single simulation runs of the VEI 2 eruption scenario, shown together with the studied crops. The simulations illustrated here were randomly selected. Red to yellow shading represents ashfall loading (kg/m²), with darker red indicating higher loads. Points represent the distribution of major crop types: vineyards (purple), orchards (blue) and olive trees (green).

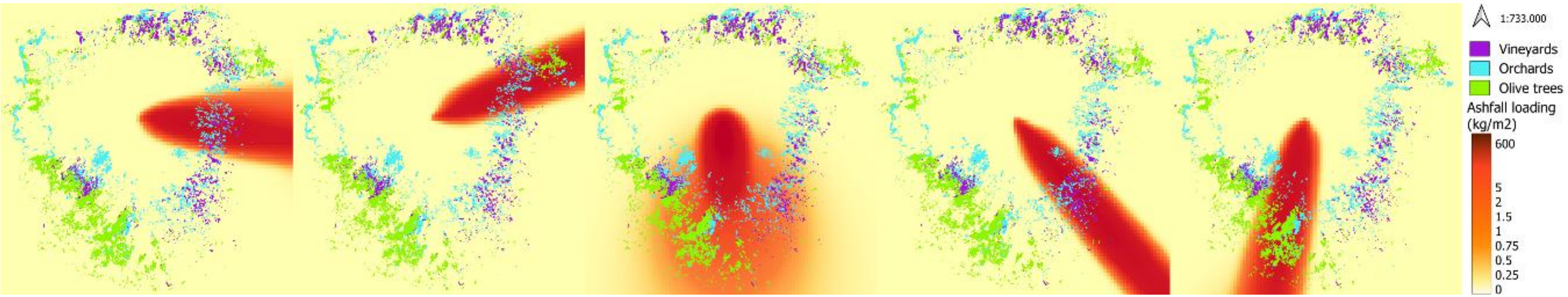

Figure 19. Five examples of ashfall loading maps (kg/m²) from single simulation runs of the VEI 3 eruption scenario, shown together with the studied crops. The simulations illustrated here were randomly selected.

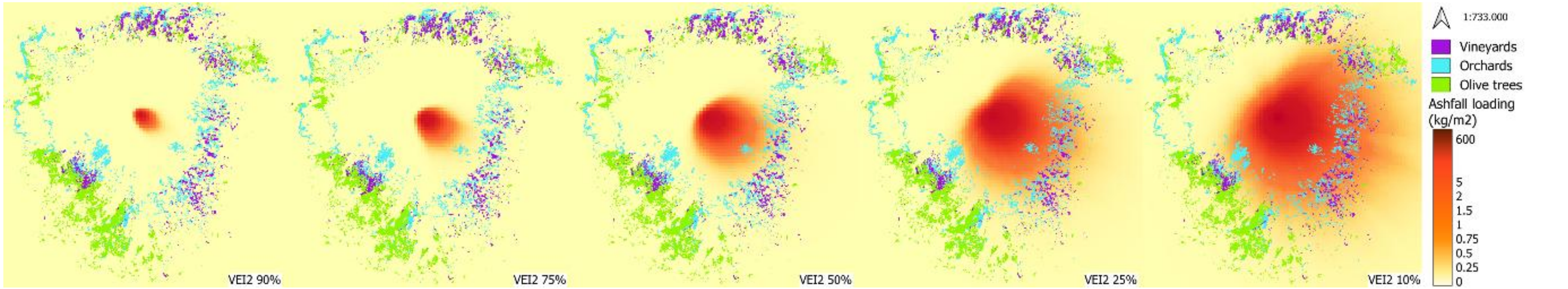

Figure 20. Five probabilistic ashfall loading isomass maps (kg/m^2) with a probability of exceedance of 90%, 75%, 50%, 25% and 10% for the VEI 2 eruption scenario, shown together with the studied crops.

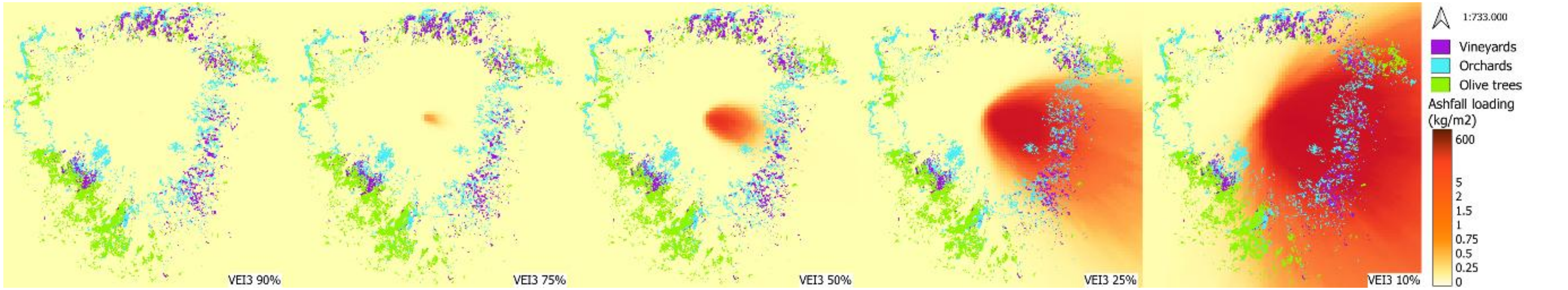

Figure 21. Five probabilistic ashfall loading isomass maps (kg/m^2) with a probability of exceedance of 90%, 75%, 50%, 25% and 10% for the VEI 3 eruption scenario, shown together with the studied crops.

4.3. Vulnerability assessment

As mentioned in Section 2.8, fragility functions are regarded as the most robust tool for assessing crop vulnerability. In addition to tephra mass loading, crop phenological stage and morphological traits are key determinants of yield loss (Craig et al., 2021; Ligot, Bogaert, et al., 2022; Ligot, Delmelle, et al., 2022; Ligot, Guevara, et al., 2022; Thompson et al., 2017; Wilson & Kaye, 2007; Wilson et al., 2015). Consequently, fragility functions are generally constructed by phenological stage and by crop groups that share similar morphological characteristics. Based on crop trait classifications from previous vulnerability studies (Craig et al., 2021; Ligot, Viera, et al., 2024; Wilson & Kaye, 2007), the crops studied in this work fall into two categories: fruit trees (olives and orchards) and viticulture (vineyards). Vineyards are woody climbing plants rather than fruit trees and therefore exhibit distinct crop traits, as will be detailed later.

Following a review of the limitations of the methodology and dataset used by Craig et al. (2021) to construct their fragility functions (Section 8.2), new functions were developed in this study using a post-impact assessment dataset. Ligot, Viera, et al. (2024) collected post-eruption crop yield loss data through farmer interviews in the vicinity of the Tungurahua volcano, Ecuador. Using this dataset to derive crop fragility functions for the present study requires a key assumption: Differences in climate, agricultural practices and crop varieties between the Tungurahua region and other volcanic regions (e.g., Mount Etna) do not significantly influence crop vulnerability to tephra fall. This assumption is a necessary approximation due to the lack of comparative data.

Dataset from post-impact assessment

Ligot, Viera, et al. (2024) do not specify whether yield losses refer to reductions in agricultural yield (i.e., production volume) or economic yield (i.e., market value). The dataset contains observations for fruit trees with traits similar or identical to those of the species considered in this study, including Ecuadorian apples, pears and cherries, but none for vineyards or other woody climbing plants. Consequently, fragility functions were developed for olive trees and orchards using the fruit tree data and subsequently adapted to vineyards by accounting for morphological differences and their influence on crop vulnerability to tephra fall.

Constructing fragility functions by phenological stage with non-linear regression

The aim of our fragility functions is to describe the relationship between tephra fall loading (kg/m^2) and crop yield loss (%). Craig et al. (2021) show that the probability of exceeding a damage threshold increases non-linearly with tephra thickness, with steep impacts at low loads and a plateau at higher values. To capture this shape, we tested a non-linear regression model incorporating a negative exponential term, inspired by the exponential variogram model (Matheron, 1963). In geostatistics, the variogram characterises the semivariance of the difference between random variable measurements as a function of their distance. Among existing variogram models, the exponential form was chosen for its curve, which closely resembles those of Craig et al. (2021): a steep initial slope followed by an asymptote (Figure

22). This reflects the strong crop vulnerability to even small tephra loads, as also reported in the literature (Ligot, De Tornaco, et al., 2024).

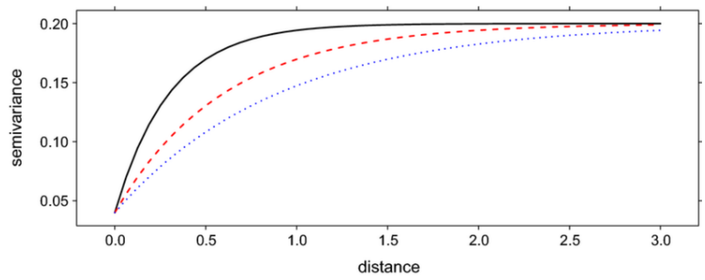

Figure 22. Example of exponential variogram model curves (Meilán-Vila et al., 2021). The curves are shown for different values of parameter a: 0.3 (solid line), 0.6 (dashed line) and 0.9 (dotted line). These examples illustrate how parameter a controls the rate of increase of semivariance with distance.

The model is defined as

$$y = b \cdot \left(1 - e^{-x/a}\right) \tag{2}$$

where *b* is the asymptotic value (here set to 100, representing maximum loss) and *a* controls the rate of increase: small *a* values yield steep curves, while larger *a* values produce more gradual slopes.

The shape of the fragility curves from Craig et al. (2021) was adopted despite differences in HIM and impact units. Tephra loading (kg/m^2) is directly convertible to tephra thickness (mm) following

$$Tephra\ loading \left[\frac{kg}{m^2}\right] \cdot Density^{-1} \left[\frac{m^3}{kg}\right] \cdot 10^{-3} \left[\frac{mm}{m}\right] = Tephra\ thickness\ [mm] \tag{3}$$

Assuming a typical bulk density of 10^3 kg/m^3 for tephra deposits (Eychenne & Le Pennec, 2012)

$$1 \left[\frac{kg}{m^2}\right] \cdot 10^{-3} \left[\frac{m^3}{kg}\right] \cdot 10^3 \left[\frac{mm}{m}\right] = 1\ [mm] \tag{4}$$

so that

$$1 \left[\frac{kg}{m^2}\right] = 1\ [mm] \tag{5}$$

Thus, hazard intensity measures are fully comparable. By contrast, loss metrics (y-axis) less directly comparable, since threshold exceedance probabilities and observed yield losses cannot be strictly equated.

Post-eruption fruit tree yield loss data treatment and manually adjusted fragility function curves from regression

A fragility function was developed for each phenological stage reported in the post-eruption fruit trees yield loss assessment of Ligot, Viera, et al. (2024) : growth, flowering, maturation and harvest. No function was defined for the "no growth" stage as losses are assumed to be null when tephra fall occurs during this period.

For each dataset grouped by phenological stage (Table 4), outliers were excluded prior to performing non-linear regression when they reported implausible yield losses given the associated tephra loading or deviated strongly from the general trend. Parameters *a* and *b* in the non-linear regression model (Equation 2) were subsequently adjusted manually, based on expert judgement. Parameter *b* was systematically fixed at 100, reflecting the assumption of total yield loss at high tephra loads. Parameter *a* was adjusted to ensure that the resulting curve both captured the empirical pattern and remained consistent with expected crop behaviour. As R^2 is not appropriate for evaluating non-linear fragility functions, it was not calculated here.

Phenological stage	Number of post-eruption fruit trees yield loss observations	Number of outliers	Parameter *a* as yielded by regression	Manually corrected *a*	Parameter *b* as yielded by regression	Manually corrected *b*
Growth	10	2	0.036	1.0	81	100
Flowering	21	0	0.088	0.090	98	100
Maturation	14	2	1.5	1.5	90	100
Harvest	18	1	0.3	0.30	86	100

Table 4. Number of post-eruption fruit trees yield loss observations from Ligot, Viera, et al. (2024) by phenological stage, with identified outliers and regression parameters before and after manual adjustment.

Ligot, Viera, et al. (2024) recorded ten observations for fruit trees in the growth stage (Table 4). Two records indicating 50% loss at a tephra load of 7.8 kg/m² were excluded as inconsistent with the overall trend. Regression with Equation 2 yielded parameters *a* = 0.036, *b* = 81. After fixing *b* at 100, parameter *a* was set to 1.0 to avoid an excessively steep slope and to better represent observed losses above 2 kg/m² (Figure A7).

They also recorded twenty-one observations for fruit trees in the flowering stage, with no outliers identified. Regression yielded parameters *a* = 0.088, *b* = 98. Parameters were standardised to *a* = 0.090 and *b* = 100 (Figure A8).

The same dataset includes fourteen observations for fruit trees in the maturation stage. Two data points showing complete yield loss at very low tephra loads (0.14 kg/m² and 1 kg/m²) were excluded from the analysis, as they were not consistent with the general trend. Regression with Equation 2 yielded parameters *a* = 1.5, *b* = 90 after which *b* was manually fixed at 100 to reflect the theoretical maximum loss (Figure A9). While this adjustment slightly underestimates the two observed values around 10 kg/m², it maintains overall consistency with the concentration of points on the left side of the curve and supports a more representative shape.

The same dataset includes eighteen observations for fruit trees in the harvest stage. One record of zero loss at 7.8 kg/m² was excluded as an outlier, as it appeared inconsistent with the overall dataset. Regression with Equation 2 yielded parameters a = 0.30, b = 86. Parameter *b* was automatically set to 100 and *a* was retained as the curve was consistent with the expected progression of losses (Figure A10).

Morphological traits influencing the adaptation of fruit trees fragility functions to vineyards

As explained in Section 2.8, crop morphological traits are key determinants of vulnerability to tephra fall. As vineyards differ morphologically from fruit trees, the fragility functions developed for fruit trees were adapted to vineyards by accounting for these differences and their influence on crop vulnerability. The crop traits most strongly affecting vulnerability at each phenological stage are presented in Table 5, following the methodology proposed by Lucie Heins (2025; in preparation), a master student working on crop vulnerability to tephra fallout under the supervision of Prof. Pierre Delmelle. In her approach, yield loss for each crop group and phenological stage is adjusted through phenological stage-specific correction coefficients that account for trait-driven differences in vulnerability. The coefficients are derived from the literature and refined through expert consultation. They are applied differently for each phenological stage, as each stage has specific plant traits that significantly influence final yield (Table 5. Key crop characteristics contributing to vulnerability to tephra fall according to the phenological stage at the time of deposition (Heins, 2025).Table 5). For instance, leaf morphology plays a greater role during the growth stage, whereas the duration of the flowering period is more determinative during flowering (Blong, 1984; Cook et al., 1981; Ligot, De Tornaco, et al., 2024).

Phenological stage	Crop traits contributing to vulnerability
Growth	Leaf inclination angle, Leaf pubescence, Leaf initiation rate
Flowering	Flowering duration
Maturation	Leaf inclination angle, Leaf pubescence, Fruit pubescence
Harvest	Fruit pubescence

Table 5. Key crop characteristics contributing to vulnerability to tephra fall according to the phenological stage at the time of deposition (Heins, 2025).

Development of adaptation coefficients based on morphological differences between the case-study vineyards and the fruit trees in the dataset from Ligot, Viera, et al (2024)

As mentioned above, the dataset collected by Ligot, Viera, et al (2024) includes post-eruption crop yield loss observations for fruit trees but not for woody climbing plants such as grapevines. Fragility functions were therefore developed directly from these fruit tree observations and subsequently adapted to vineyards. To achieve this, the morphological traits of the fruit tree species represented in the dataset were compared with those of the grapevine varieties cultivated on Mount Etna.

The most widely cultivated grapevine varieties on Etna include Carricante, Catarratto, Nerello Mascalese and Nerello Mantellato (also known as Nerello Cappuccio) (Ministro dell’agricoltura, della sovranità alimentare e delle foreste, 2022).

Leaf pubescence

All tree species exhibit glabrous (non-hairy) leaves, with the exception of apple trees whose foliage is pubescent only on the abaxial surface (Hernández Bermejo et al., 1994; Motooka et al., 2014; Rieger, 2006; Terwei, 2014; Tison et al., 2014). In grapevines, although some cultivars, such as Carricante, may possess a few hair, their density is typically very low (Ministero dell'agricoltura, della sovranità alimentare e delle foreste, 2024). As dust accumulation on the foliage is proportional to leaf hair density (Ram et al., 2014; Sæbø et al., 2012), both categories are treated as glabrous. Consequently, no corrective coefficient for pubescence is applied.

Fruit pubescence

Fruits are glabrous across both categories; however, a distinction must be made regarding grape clusters. They exhibit a dense morphology that favours the retention of particulate matter such as flower debris (Figure 23) (Hed et al., 2009). Their dense structure is known to limit airflow and create enclosed micro-environments, increasing the fruit's vulnerability to moisture-related diseases. While no study has directly measured the accumulation of fine particles on grape clusters, it can reasonably be inferred that compact grape clusters may retain ash more effectively due to their structural traits. Cluster compactness varies between cultivars. As cultivar-level distinctions are not available in the spatial data for the study area, we assume that all grapevine cultivars considered here exhibit this morphological characteristic.

In addition, because vineyards grapes are intended for vinification, any physical or chemical alteration of the berries can negatively affect the market value of the resulting wine (Neild et al., 1998). Ash deposition during fruit development and maturation may obstruct sunlight interception, potentially compromising grape composition and ripening dynamics (Neild et al., 1998). During harvest, ash represents a direct contaminant potentially affecting the wine quality (Neild et al., 1998). Ash would have to be removed by washing the grape clusters but the process is particularly difficult : rinsing with water is often insufficient, and effective cleaning typically requires costly manual labour (Barnard, 2004).

Figure 23. Photograph of a grape cluster from the Carricante variety (Firriato Winery, 2017)

No data are currently available on the influence of cluster-like fruit morphology on the retention of tephra. Craig et al. (2021) estimated that the difference between fully vulnerable and moderately vulnerable crops to tephra fall corresponds to a 15% variation in yield loss and used it as a correction coefficient. This value is therefore used as a corrective factor to account for the influence of the aforementioned traits on vulnerability. This correction is applied at an intermediate tephra load of 5 kg/m², considering that yield loss is null at 0 kg/m² and that beyond 10 kg/m², morphological and phenological traits exert decreasing influence compared to the effect of deposit thickness (Ligot, De Tornaco, et al., 2024).

<u>Leaf Inclination Angle</u>

Vine leaves generally exhibit a more vertical orientation compared to those of fruit trees such as apple, pear, cherry and olive trees. This is attributed to the climbing morphology of the vine and its cultivation on trellising systems (Figure 24) (Chasseloup, 2024; Khadatkar et al., 2025). Conversely, conventional fruit trees typically develop a more spreading canopy and a more horizontal habit, resulting in a predominantly horizontal leaf inclination angle (Haehnel, 2015; Institut Technique Horticole de Gembloux, n.d.; Quellier, 2003). A more vertical foliage is more likely to retain volcanic ash. As observed by Ligot, Bogaert, et al. (2023) on glabrous chili pepper leaves, *"leaf angle dictates whether ash particles remain on the leaf surface after deposition or slide off and relocate elsewhere"*. This increased retention leads to greater yield loss, as the presence of solid particles on foliage exerts a shading effect. This reduces light interception, which in turn decreases net photosynthetic rate and ultimately lowers total biomass production (Biscoe et al., 1977; Monteith, 1977; Weraduwage et al., 2015; Wilson, 1967).

Figure 24. Photograph of vineyards at the foot of Mount Etna, at the Romeo del Castello estate (Frankel, 2019).

To quantify the impact of leaf angle on ash-induced yield loss, a greenhouse experiment was conducted on lettuce and cabbage, two crops exhibiting contrasting leaf inclination angles (Ligot, De Tornaco, et al., 2024). The difference in average crop production loss between the two species, measured after volcanic application at maturity, was 23% at 5 kg/m², 35% at 10 kg/m², and 39% at 30 kg/m², with greater losses recorded for lettuce due to its more horizontally oriented leaves. The average difference in production loss is 32.3%.

However, lettuce and cabbage are annual, near-ground crops harvested for their foliage, making their yield highly sensitive to ash retention on leaves. In contrast, fruit trees produce edible organs that are less directly affected by foliage shading or ash cover. Therefore, it is assumed that the sensitivity of fruit trees productivity to leaf inclination is lower than that of leafy vegetables. To reflect this lower sensitivity, the coefficient is arbitrarily divided by three, yielding an adjusted value of 10.8% rounded to 11%. This adjustment remains a pragmatic approximation, given the absence of empirical data specific to fruit trees but the adjusted value is consistent with the order of magnitude of the 15% yield difference reported by the coefficient proposed by Craig et al. (2021). The correction is also applied at 5 kg/m².

Leaf initiation rate

According to the methodology proposed by Heins (2025), the criterion of leaf initiation rate is not considered applicable to perennial species such as fruit trees and grapevines.

Flowering duration

Flowering durations vary according to local climatic conditions. However, none of the species under consideration display a flowering period extending over several months, a criterion identified in Heins (2025) as relevant for adjusting sensitivity. Consequently, no coefficient is applied for this parameter.

Phenological stage	Yield loss adjustment coefficient
Growth	$y - 11$
Flowering	No adjustment needed
Maturation	$y(* 0.85) - 11$
Harvest	$y(* 0.85)$

Table 6. Adjustment coefficients for yield loss associated with tephra deposits of 5 kg/m² to be applied on fruit trees fragility function to obtain vineyards fragility function, according to the crop's phenological stage at the time of deposition.

The resulting fragility functions for fruit trees and vineyards are presented in Figure 25 to Figure 28.

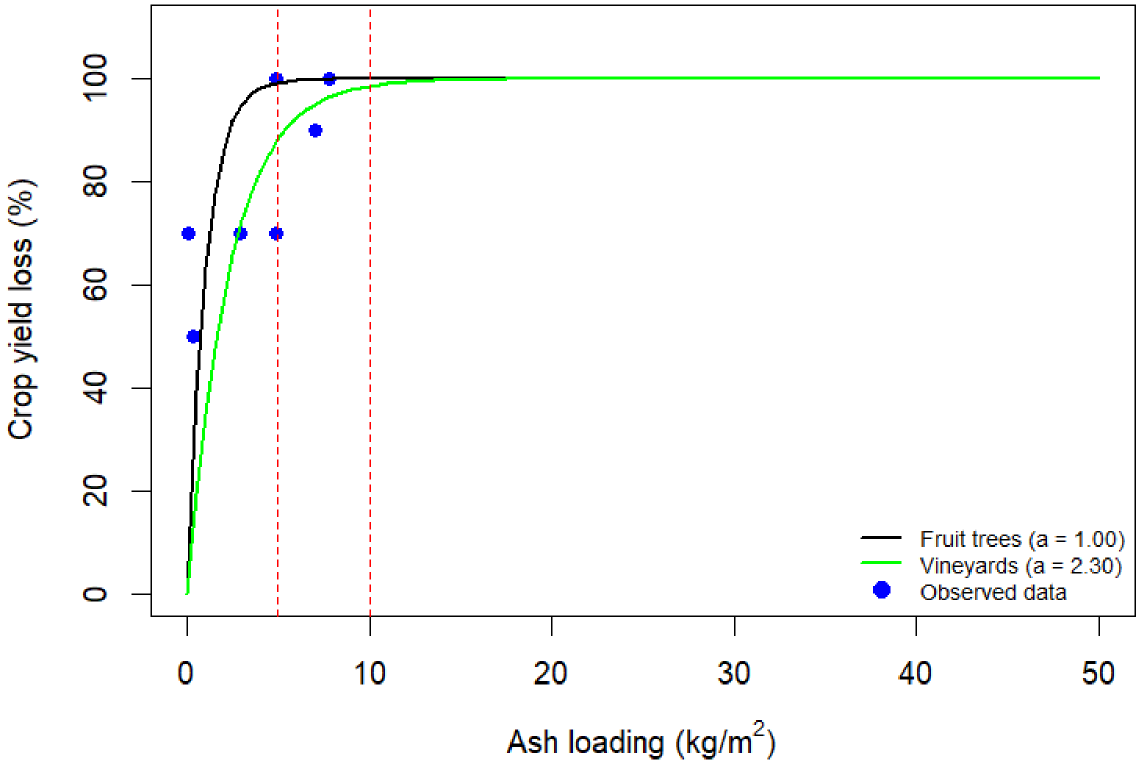

Figure 25. Fragility function for fruit trees and vineyards during the growth stage based on data from (Ligot, Viera, et al., 2024)

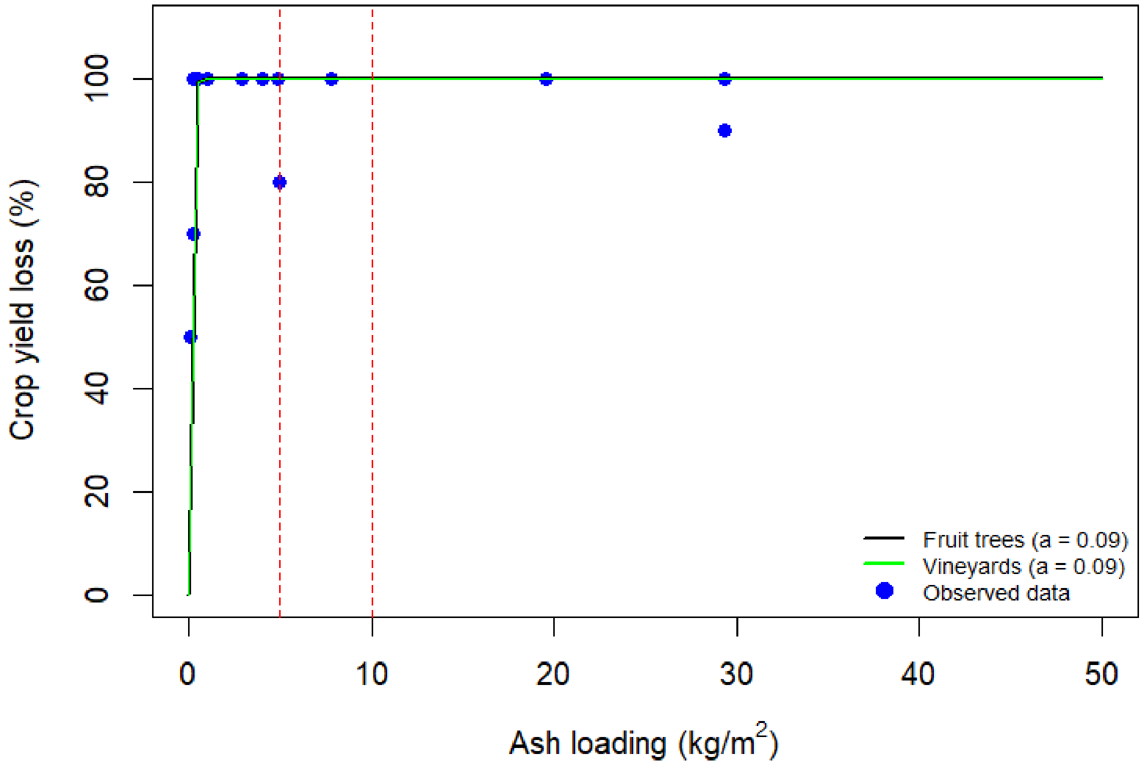

Figure 26. Fragility function for fruit trees and vineyards during the flowering stage based on data from (Ligot, Viera, et al., 2024)

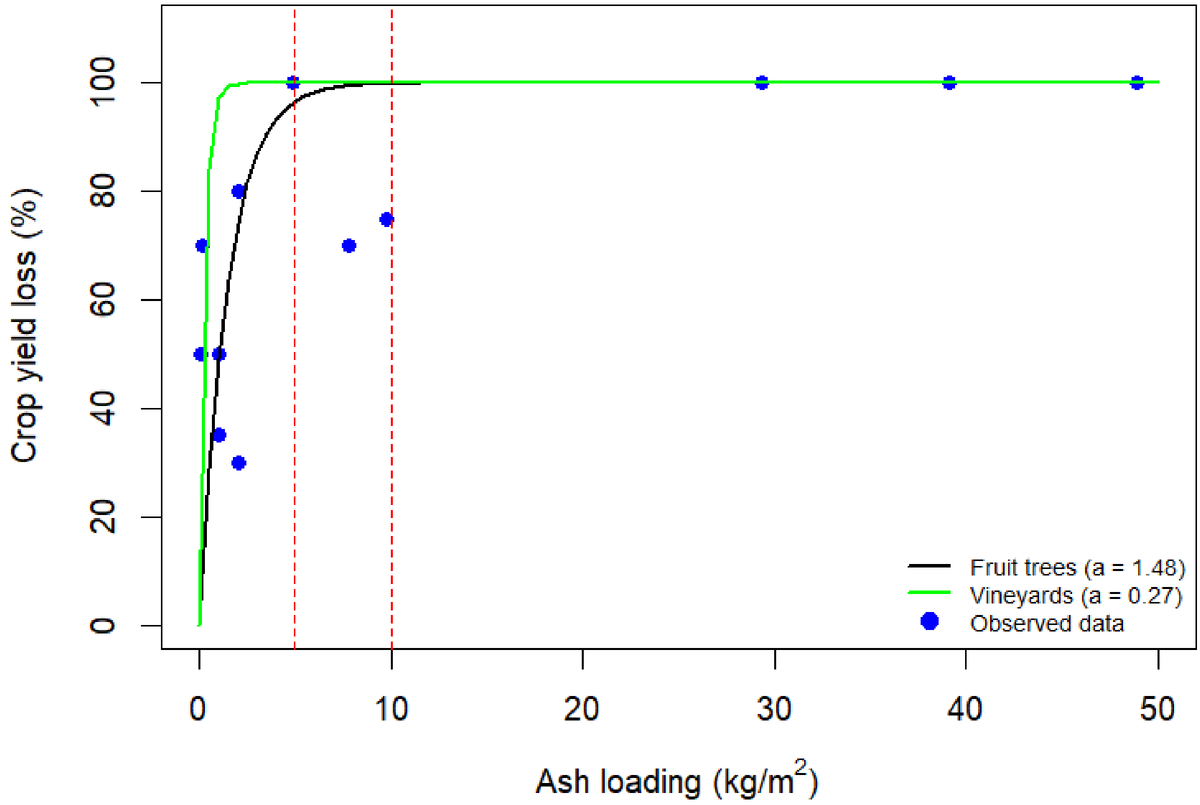

Figure 27. Fragility function for fruit trees and vineyards during the maturation stage based on data from (Ligot, Viera, et al., 2024)

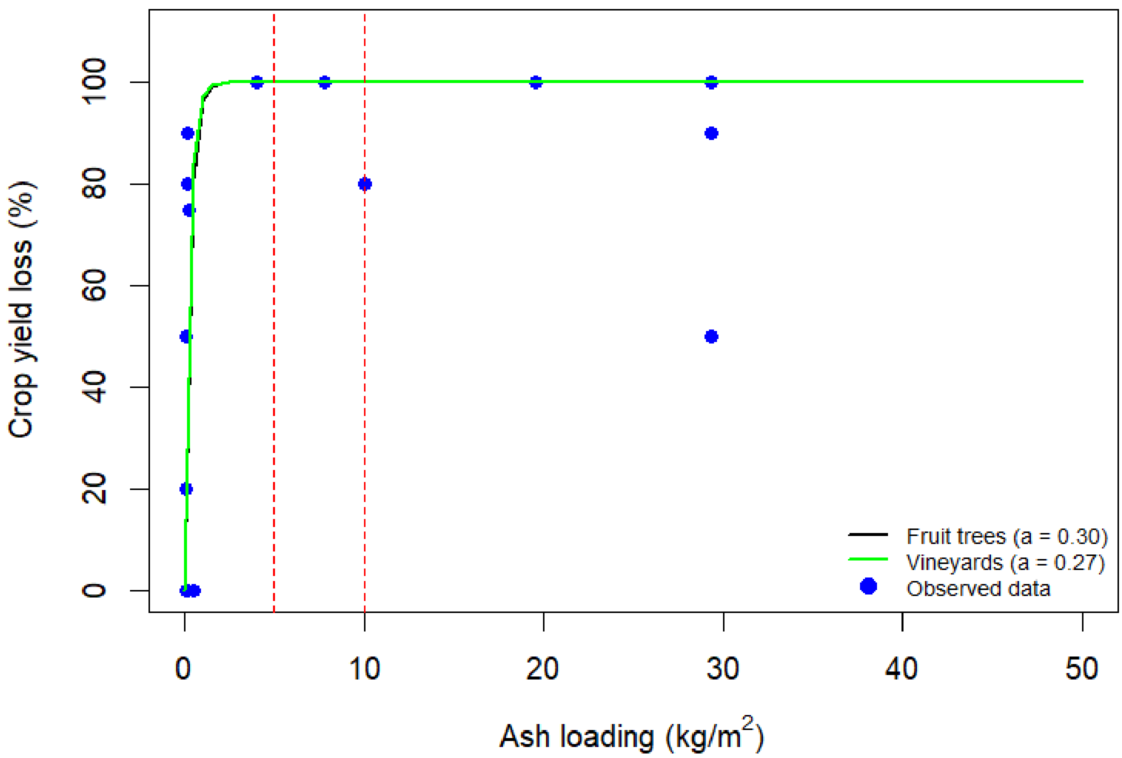

Figure 28. Fragility function for fruit trees and vineyards during the harvest stage based on data from (Ligot, Viera, et al., 2024)

4.4. Seasonality

To account for the temporal evolution of phenological stages, and therefore of crop vulnerability to yield loss following tephra fall, we developed a crop calendar. A crop calendar describes the development cycle of locally adapted crops (i.e., vegetative growth, reproductive, and ripening phases) and guides key agricultural operations such as sowing, ploughing, fertilising, weeding, and harvesting (FAO, 2023; Yulianti et al., 2016). In this work, we refer to it as a *phenological calendar*, acknowledging that our calendars are not exhaustive in their staging. They distinguish five stages, although in reality many more can be identified, as in the BBCH scale (Meier, 2001).

Based on the timing of phenological stages, a calendar was constructed for each crop, including the three species on Mount Etna classified as “orchards” by Signorello et al. (2020). Information was compiled from agricultural technical sheets, phenology progress reports and websites related to plant protection products, gastronomy or tourism (Angys, n.d.; Berud & Simler, 2018; BRAVOLEUM, n.d.; cyber, 2019; DALIVAL, n.d.; D’Arapri, n.d.; DRAAF Occitanie, 2023; *Fao Crop Calendar*, n.d.; Ferrara & Ingemark, 2023; Gambin, 2024; Italian food experience, 2018; La Praglia, 2014; LoSaiChe, 2021; Oukabli et al., 1998; Palmeri, 2009; Pierantozzi et al., 2017; Qualigeo, n.d.; Slow Food, n.d.; Viticabrol, n.d.). To construct Table 7, the calendars for apple, pear and cherry crops were merged under the “orchards” classification in the Etna land-use map (Signorello et al. 2020). At each time step, the most vulnerable stage among the three species was retained, consistent with the parameters of the fragility functions.

Season	Period		Phenological stage		
			Vineyards	Olive trees	Orchards
Winter	January	1	NG	NG	NG
	2nd half	2	NG	NG	NG
	February	3	NG	NG	NG
	2nd half	4	NG	NG	G
	March	5	NG	G	G
Spring	2nd half	6	G	G	G
	April	7	G	G	F
	2nd half	8	G	F	F
	May	9	F	F	M
	2nd half	10	F	M	M
	June	11	M	M	M
Summer	2nd half	12	M	M	H
	July	13	M	M	H
	2nd half	14	M	M	H
	August	15	M	M	H
	2nd half	16	M	M	H
	September	17	H	M	M
Autumn	2nd half	18	H	M	H
	October	19	H	M	H
	2nd half	20	NG	H	H
	November	21	NG	H	H
	2nd half	22	NG	H	NG
	December	23	NG	H	NG
Winter	2nd half	24	NG	H	NG

Table 7. Phenological stages of the three studied crops by biweekly period and season.
NG = no growth (dormancy); G = growth; F = flowering; M = maturation; H = harvest.

4.5. Risk assessment models

Figure 1 summarizes the structure of the risk assessment framework developed in this master's thesis and applied to the agricultural areas surrounding Mount Etna. Information on hazard, exposure and vulnerability is integrated within two types of risk models, depending on the format of the hazard data. When tephra deposits are provided as probabilistic isomass maps (IM), they are processed using the "IM" model. When provided as 1000 individual simulation runs distributed throughout the year (the format generated by TephraProb prior to aggregation into IM) tephra deposits are processed using the "1000 simulations" model. Exposure is defined by the spatial distribution of crops, while vulnerability is determined using fragility functions and crop calendars. Combining these components yields estimates of crop yield loss, expressed either as a single value (for the "1000 simulations" model) or for specified exceedance probability levels (for the "IM" model).

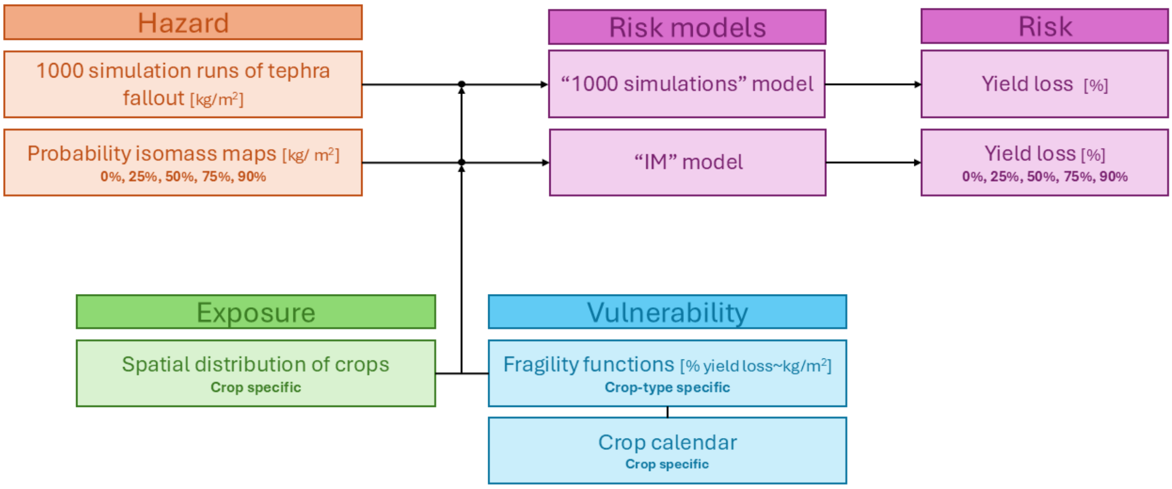

Figure 29. Workflow of tephra fall risk assessment for crop yield loss. Hazard (tephra fallout) is represented either by 1,000 simulation runs or probabilistic isomass maps, processed through the respective risk models. Exposure is defined by the spatial distribution of crops (olive trees, orchards, vineyards) and vulnerability by crop-type-specific fragility functions and phenological calendars. Crops: olive trees, orchards and vineyards. Crop types: fruit trees and vineyards. These components are combined to estimate yield loss.

Operation of the IM risk model

In the IM model, probabilistic isomass maps (500 m pixel size) are resampled to align with the land use/land cover (LULC) map (20 m pixel size) (Figure 15). For each pixel, location data are combined with the cultivated crop and the tephra load corresponding to each exceedance probability (10%, 25%, 50%, 75% and 90%). Tephra loads are assumed constant throughout the year as they represent probabilistic aggregations of tephra dispersion simulations (Section 4.2).

To calculate yield loss, the year is divided into 24 biweekly periods, following the crop calendar. For each pixel, the tephra load is combined with the fragility function corresponding to the crop type and phenological stage for that period, producing yield loss values. For each biweekly period, five yield loss values are obtained: one for each exceedance probability (10%, 25%, 50%, 75% and 90%). This process is repeated two eruption scenarios of different magnitudes (VEI 2 and VEI 3).

Operation of the 1000 simulations risk model

The 1000 simulations model follows the same initial data preparation but instead of relying on aggregated IMs, it processes the 1000 individual simulations per eruptive scenario, each tied to unique start and end dates. This way, the model captures both the seasonality of crop vulnerability and tephra fall spatial distribution driven by wind dynamics. The mean tephra load per period is calculated for each pixel in the agricultural area. Simulations from the same biweekly period are summed and divided by the number of simulations. If a simulation spans multiple periods, it is assigned to the most sensitive period (based on the fragility function parameters). Yield loss is then calculated for each period using the corresponding mean tephra load per pixel. For each period, one yield loss value is produced. As with the IM model, this process is repeated for two eruption scenarios of different magnitudes (VEI 2 and VEI 3).

Both approaches assume that the eruption scenarios could occur at any time of the year with equal probability, without considering the absolute annual probability of occurrence of such an eruption. It also treats the entire tephra fall as if it were deposited instantaneously, without accounting for multi-week or multi-month eruptive durations. While this simplification inherently limits the scope of the analysis, it highlights the period during which an eruption initiates as most critical, given the high sensitivity of crops to even minor tephra loads (Thompson et al., 2017).

4.6. Temporal and spatial aggregation of yield loss data

The two crop loss risk models developed in this study provide pixel-based estimates of yield loss per period (24 biweekly periods) and per eruptive scenario (VEI 2 and VEI 3). For a single agricultural pixel, this results in biweekly 24 periods × 2 eruption scenarios × (5 deposits with exceedance probabilities + 1 mean deposit) = 288 yield loss values.

These data can be aggregated in two complementary ways: spatially and temporally.

Spatial aggregation consists of computing the average yield loss over the studied area, either across the entire agricultural area or per crop, for each period. This aggregated value is referred to in this work as the Mean Yield Loss.

Temporal aggregation involves averaging the yield loss values across time for each agricultural pixel, either over the entire year or within seasons. These values are referred to as the Annualized Index of Yield Loss (AIYL) and the Seasonal Index of Yield Loss (SIYL), respectively.

The Annualized Index of Yield Loss (AIYL) represents the average expected yield loss across the 24 biweekly periods of the year, assuming the eruption could occur at any time with equal probability. This index captures spatial variations in crop vulnerability and exposure. However, it does not incorporate the actual annual probability of eruption and thus should not be interpreted as an Expected Annual Loss in a strict probabilistic sense. Rather, the AIYL serves as a standardized metric to compare average annualized impacts between eruption scenarios and crops.

It is calculated as

$$AIYL = \frac{1}{24}\sum_{p=1}^{24} yl_p \tag{6}$$

where yl_p is the estimated yield loss for a period *p*.

Likewise, the Seasonal Index of Yield Loss (SIYL) is defined as the average yield loss for a given pixel over a specific season (e.g., spring, summer), again assuming equal probability of eruption during any period within that season. It allows finer analysis of seasonal vulnerability and facilitates comparisons between the seasonal impact profiles of different scenarios. The SIYL is computed similarly to the AIYL, but the summation is restricted to the periods included in the corresponding season.

5.1. Mean Yield Loss and AIYL over the entire studied area in the IM Model

Average crop yield losses over the studied agricultural area obtained from the IM model under the VEI 2 eruption scenario (Figure 30; Table A5. Mean and standard deviation of crop yield loss (%) over the studied agricultural area, by biweekly period, from the IM model, associated with tephra fallout exceeding thresholds with 10%, 50%, and 90% probability under VEI 2 and VEI 3 eruption scenarios.) follow seasonal patterns and differ in magnitude depending on the exceedance probability associated with each isomass map used as hazard input. Losses are null during winter and early spring (periods 1 to 3) as crops remain in dormancy (Table 7). From the end of winter through early May (periods 4 to 9), losses increase progressively, peaking at period 8 when all the crops are flowering simultaneously. This trend coincides with the transition of crops from dormancy into vegetative growth and subsequently flowering, which is the stage of highest vulnerability. A drop in losses occurs from late May to early June (periods 10 and 11), as crops transition to maturation and become less sensitive to tephra fall exposure. From early summer until late autumn (periods 12 to 21), losses remain relatively stable, reflecting the maturation and harvest phases. An isolated drop at period 17 reflects the only two-week summer interval during which none of the orchard species are harvestable. After mid-November (period 22 onward), yield losses decline as only olives remain harvestable.

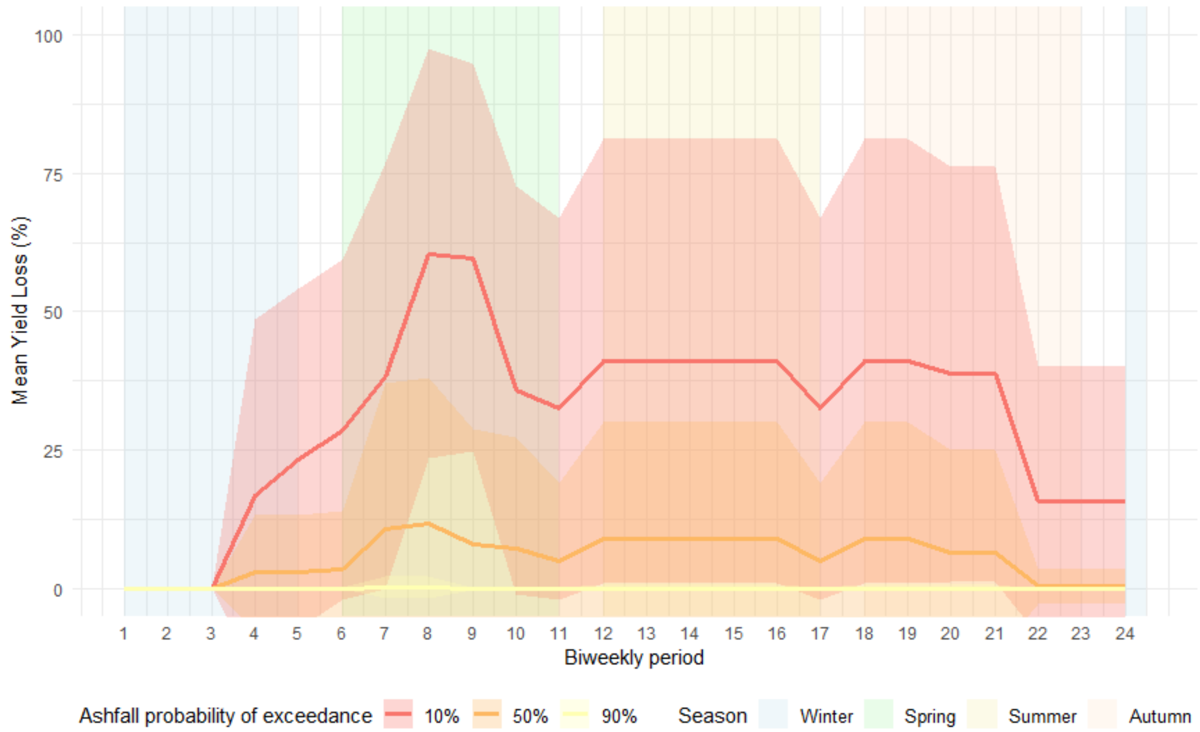

Figure 30. Mean and standard deviation of crop yield loss over the studied agricultural area, by biweekly period, from the IM model, associated with isomass maps of tephra fallout exceeding thresholds with 10%, 50%, and 90% probability of exceedance under the VEI 2 eruption scenario.

This seasonal progression is particularly evident in the curve associated with the 10% exceedance scenario but becomes less pronounced at the 50% level and nearly absent at 90%. Higher exceedance probabilities correspond to lower tephra loads levels and thus generate minimal impacts. At the 90% exceedance level, the tephra load is so limited that it barely reaches the crops and mean yield losses are negligible, ranging from 0% to 0.2%, with associated standard deviations between 0% and 1.9%. At the 50% exceedance level, mean losses range from 0.4% (SD = 3.1%) to 11.6% (SD = 26.5%) outside of dormancy periods, with seven periods (representing more than one-third of the year) consistently showing values of 9.1% (SD = 21%). At the 10% level, which corresponds to the heaviest tephra fall, mean losses range from 15.8% (SD = 24.4%) to 60.5% (SD = 37.0%) outside dormancy, with the same seven periods reaching 41.1% (SD = 40.1%). The lowest yield losses outside of dormancy periods are observed in periods 22, 23, and 24 for both the 50% and 10% exceedance curves, while the highest losses consistently occur in period 8.

While the previous analysis focused on the biweekly evolution of yield losses aggregated over the entire agricultural area (i.e., spatial aggregation by period), Figure 35 presents the spatial distribution of AIYL for tephra deposits with a probability of exceedance of 10%, 50% and 90%. Figure 31 illustrates the shape of this distribution through violin plots representing AIYL values across agricultural pixels, shown for tephra deposits with a probability of exceedance of 10%, 25%, 50%, 75% and 90%.

Under the 10% tephra fall exceedance scenario, the distribution of AIYL values is heterogeneous. Most agricultural pixels experience yield losses, with a wide range of outcomes observed, some exceeding 80%. The median AIYL lies around 25% (Figure 31), and frequent values are between 0% and 20%, with secondary peaks around 55% and 75%. Nevertheless, a proportion of the area still experiences no yield loss at all. In the 25% exceedance scenario, the distribution becomes narrower, with AIYL values ranging approximately from 0% to 75%. The majority of pixels exhibit losses below 20%, and the widest section of the distribution lies below 10%, indicating that low-impact outcomes are more prevalent. As the tephra fall exceedance probability increases (i.e., tephra fall intensity decreases), the range of observed AIYL values steadily contracts. Under the 90% scenario, losses do not exceed 10%, and the distribution becomes increasingly concentrated around zero, with only minor secondary peaks appearing below the 10% threshold. This progressive homogenization reflects the limited spatial extent and intensity of tephra fall associated with high exceedance probabilities. These observed distribution patterns confirm the trends discussed earlier: as tephra fall severity increases (i.e., when exceedance probability decreases), yield losses become not only more severe but also more spatially widespread (Figure 31). Conversely, for higher exceedance probabilities (50%, 75%, 90%), losses are increasingly marginal, with distributions sharply concentrated near zero, indicating a minimal agricultural impact.

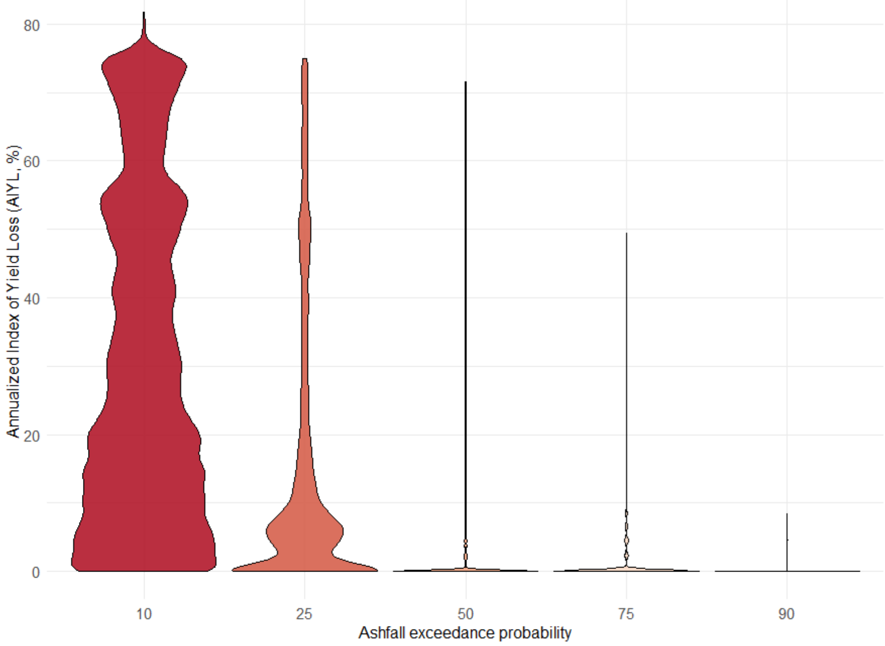

Figure 31. Distribution of the Annualized Index of Yield Loss (AIYL, %) over the agricultural area, from the IM model, for 10, 25, 50, 75 and 90% tephra load exceedance probabilities under the VEI 2 scenario.

The previous analysis focused on yield losses under the VEI 2 scenario in the IM model. Under the VEI 3 scenario within the same model, the evolution of the mean yield loss curve across the agricultural area follows the exact same pattern as that of the VEI 2 scenario: namely, it mirrors the seasonal evolution of crop vulnerability. However, the magnitude of the yield losses differs (Figure 32).

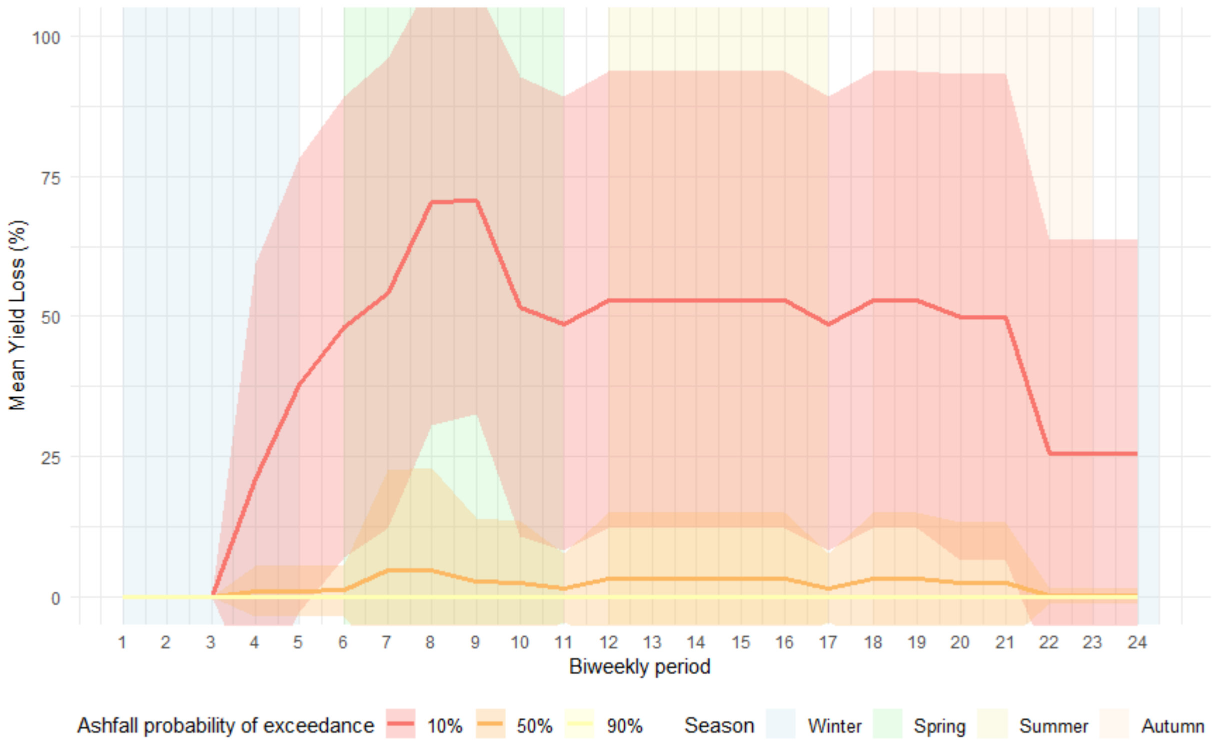

Figure 32. Mean and standard deviation of crop yield loss over the studied agricultural area, by biweekly period, from the IM model, associated with tephra fallout exceeding thresholds with 10%, 50%, and 90% probability under the VEI 3 eruption scenario.

Outside of dormancy, the 10% exceedance curve for the VEI 3 scenario ranges between 21.1% (SD = 38.4%) and 70.6% (SD = 38.1%), with more than one-third of the biweekly periods showing values of 53.0% (SD = 40.6%). Excluding dormancy, the mean VEI 3 10% curve is consistently higher than its VEI 2 counterpart, by an average of 12.3%. In contrast, the 50% VEI 3 curve is consistently lower than the 50% VEI 2 curve, with an average difference of 4.1% outside of dormancy periods. It ranges from 0.1% (SD = 1.5%) to 4.8% (SD = 18.1%), with more than one-third of the periods showing losses of 3.3% (SD = 11.7%).

For both the 10% and 50% VEI 3 curves, the maximum yield loss occurs in period 9, rather than period 8 as seen in the VEI 2 scenario. Similarly, the minimum is observed in period 4, instead of periods 22 to 24. The 90% exceedance curve under the VEI 3 scenario remains null throughout the year, along with its associated standard deviations.

5.2. Mean Yield Loss and AIYL over the entire studied area in the 1000 simulations model

The average crop yield losses over the studied agricultural area, as derived from the 1000 individual simulations model under the VEI 2 scenario (Figure 33; Table A6), are not associated with specific tephra loads exceedance probabilities, since they are calculated from the mean tephra deposit per biweekly period. These losses are influenced by both the seasonal variation in crop vulnerability and the seasonal dynamics of tephra deposition, which are primarily driven by wind patterns, an essential factor in tephra dispersal.

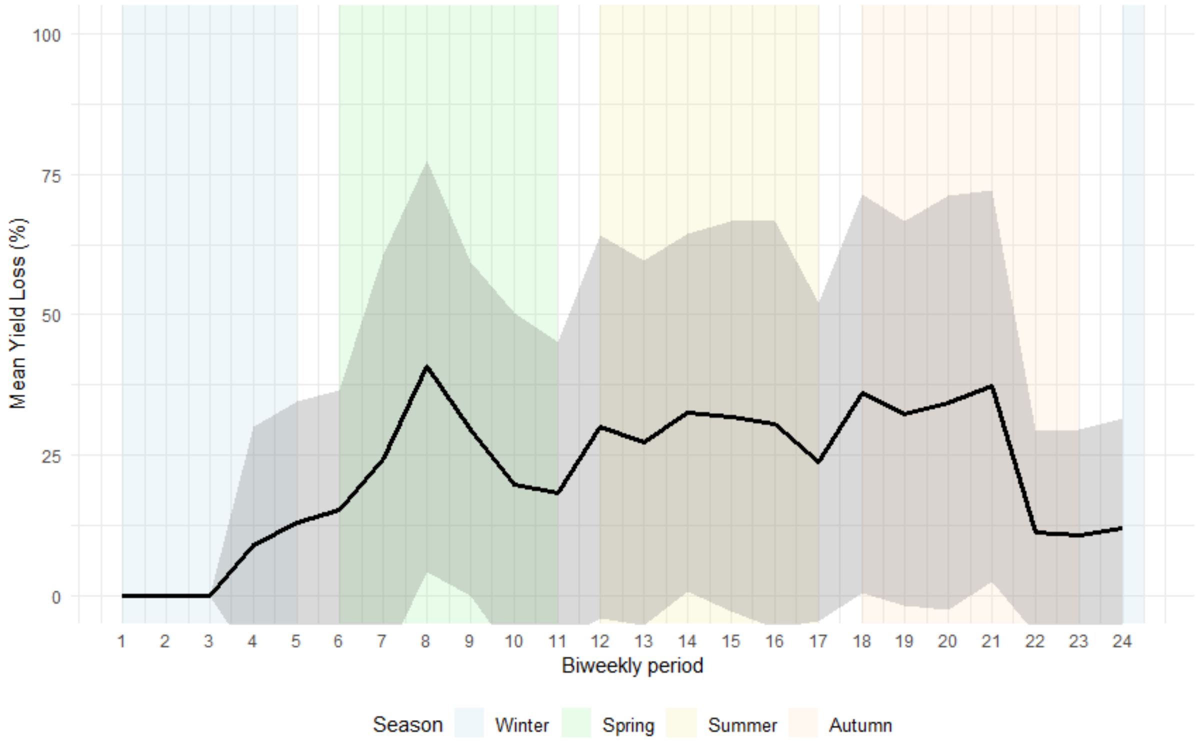

Figure 33. Mean and standard deviation of crop yield loss over the studied agricultural area, by biweekly period, from the 1000 simulations model under the VEI 2 eruption scenario.

As in the IM model, the influence of crop phenology remains evident, with no losses during winter (periods 1 to 3) and a sharp increase in spring. However, the more irregular, jagged shape of the 1000-simulation curve reflects the additional variability introduced by fluctuations in tephra fall intensity over time. Several successive periods feature constant phenological stages (e.g., periods 12 - 16, 18 - 19, 20 - 21, 22 - 24), during which the IM model yields flat curves, yet the 1000-simulation model still shows substantial variation. Notably, during summer, although phenological stages remain unchanged across all crop types for five consecutive periods, yield losses still vary, indicating that tephra deposition, rather than crop vulnerability, is driving these fluctuations.

The resulting curve lies between the 50% and 90% exceedance level curves from the IM model under the same scenario (Figure 30), consistent with the spatial tephra fall patterns (Figure 36). Outside of dormancy periods, the 1000-simulations curve is on average 10.5% lower than the 10% exceedance curve, and 18.4% higher than the 50% curve.

Beyond dormancy, yield losses range from 9.0% (SD = 21%) in period 4 to a peak of 40.8% (SD = 36.7%) in period 8. In total, 11 out of 24 periods exceed 25%, and 9 periods reach or exceed 30%.

Yield losses under the VEI 3 scenario in the 1000 simulations model are consistently higher than those observed under the VEI 2 eruption scenario (Figure 34; Table A6), on average 31.2% higher. This is due to both greater tephra loadings and a wider spatial extent of tephra deposition as Figure 37 shows with mean tephra loadings under the VEI 2 and VEI 3 eruption scenarios. Mean losses range from 13.0% (SD = 25.3%) in period 23 to a peak of 79.2% (SD = 29.7%) in period 14, with additional isolated maxima observed in periods 6, 9, 19, and 21.

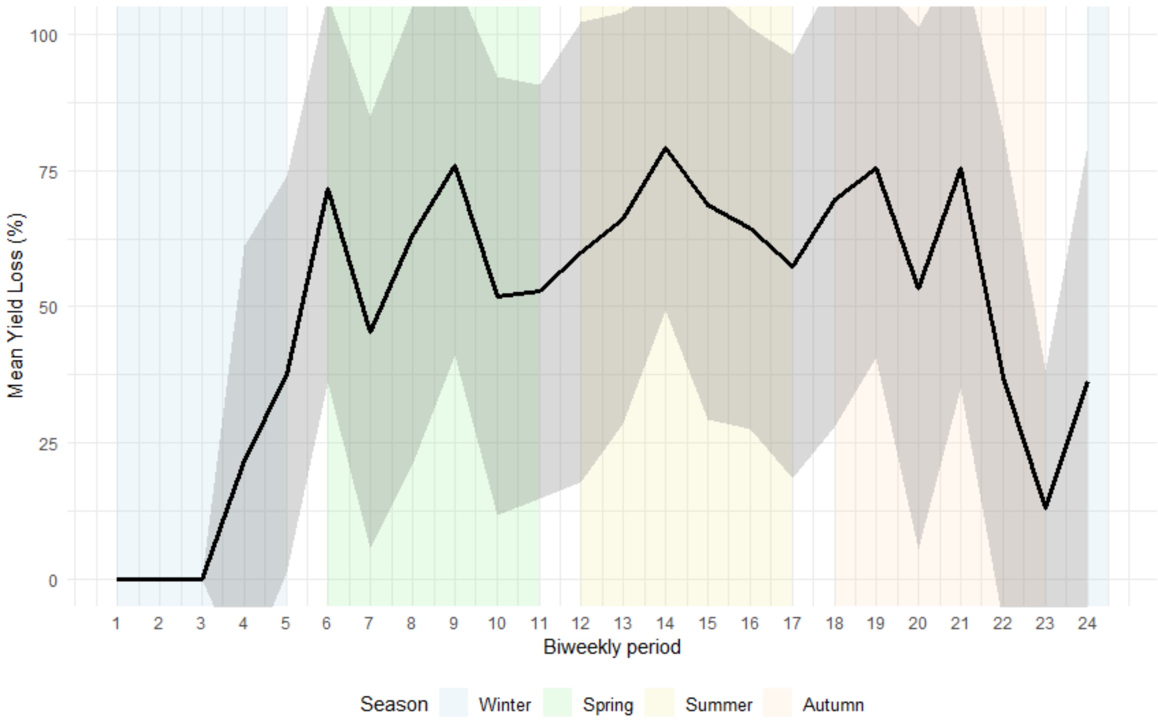

Figure 34. Mean and standard deviation of crop yield loss over the studied agricultural area, by biweekly period, from the 1000 simulations model under the sub Plinian eruption scenario.

Although yield losses in both scenarios are expected to reflect a combined influence of phenological sensitivity and tephra deposition, the VEI 3 curve departs noticeably from the crop vulnerability pattern. Unlike the VEI 2 curve, where loss fluctuations align relatively with phenological stages, the VEI 3 curve shows weaker correlation with crop sensitivity and greater irregularity. The phenological signal becomes harder to detect.

This is further evidenced by several periods during which the two eruption scenarios exhibit opposite trends in average yield loss, despite phenological stages remaining unchanged. For instance, between periods 12 and 13, and again between periods 18 and 19, yield losses increase under one scenario while decreasing under the other.

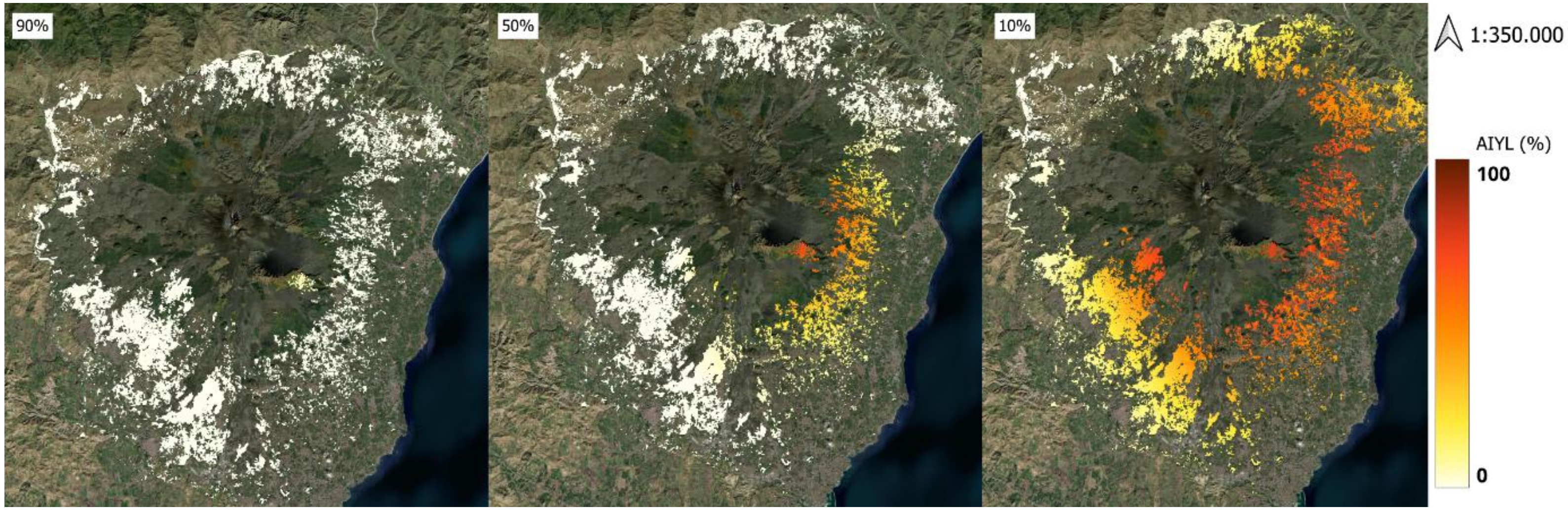

Figure 35. Spatial distribution of AIYL across the studied agricultural area from the IM model under the VEI 2 eruption scenario, for isomass deposit maps of tephra fallout with exceedance probabilities of 10%, 50%, and 90%.

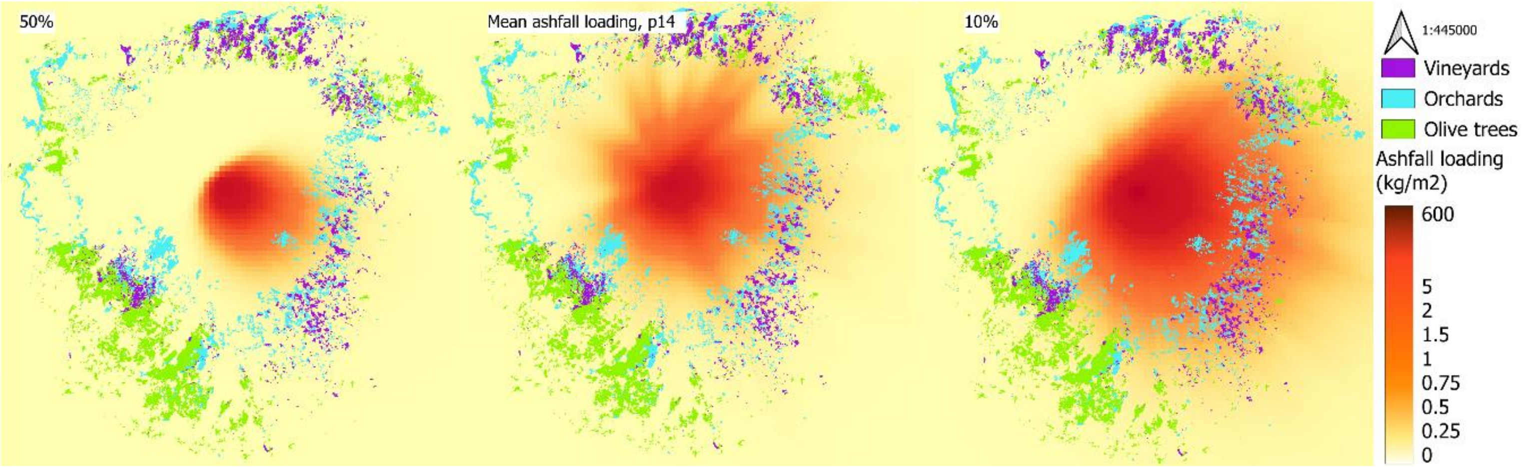

Figure 36. Maps showing the calculated distribution of ash fallout under the VEI 2 eruption scenario. Left: ash deposits with a 50% exceedance probability. Right: ash deposits with a 10% exceedance probability. Center: mean deposit from in dividual simulations during period 14. The spatial repartition of the three crops (vineyards, orchards and olive trees) is also shown.

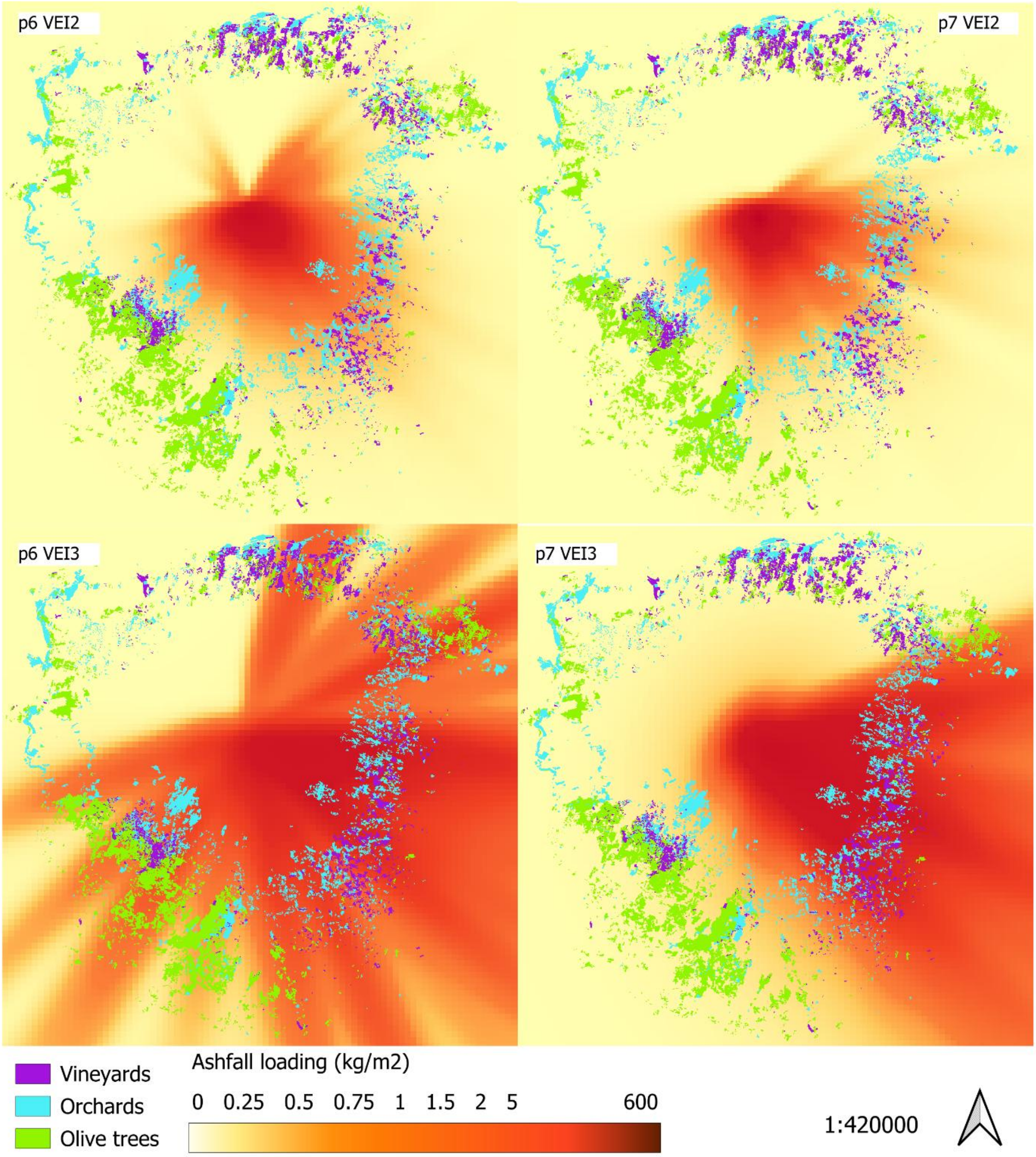

Figure 37. Distribution of crop types and mean ash loadings in periods 6 and 7 under the VEI 2 and VEI 3 eruption scenarios.

The average yield loss is directly influenced by the spatial extent of tephra deposition resulting from the simulations included in each biweekly period. In period 6, the contributing simulations exhibit varied dispersal directions around the crater, producing a more diffuse mean deposit that covers a broader agricultural area. In contrast, period 7 is characterized by simulations with more concentrated dispersal towards the northeast and southeast, resulting in a narrower deposit footprint. Consequently, the mean tephra load over croplands is lower in period 7, leading to a marked decrease in average yield loss. This explains the drop in losses between periods 6 and 7 in the 1000 simulations model for the VEI 3 scenario (Figure 34), a pattern not observed under the VEI 2 scenario (Figure 33).

5.3. Comparative analysis of eruption scenarios in the 1000 simulations model using the Annualized Index of Yield Loss

Regarding the AIYL distribution under the VEI 2 scenario in the 1000 simulations model (Figure 38; Figure 39), most agricultural pixels experience losses below 20%, although values exceeding 70% are still observed in some areas. The distribution is irregular and multimodal, with several small peaks spread across a wide range of values. Compared to the IM model (Figure 35) at the 10% exceedance level, this distribution is less homogeneous, yet more dispersed than the one observed at 25% exceedance probability.

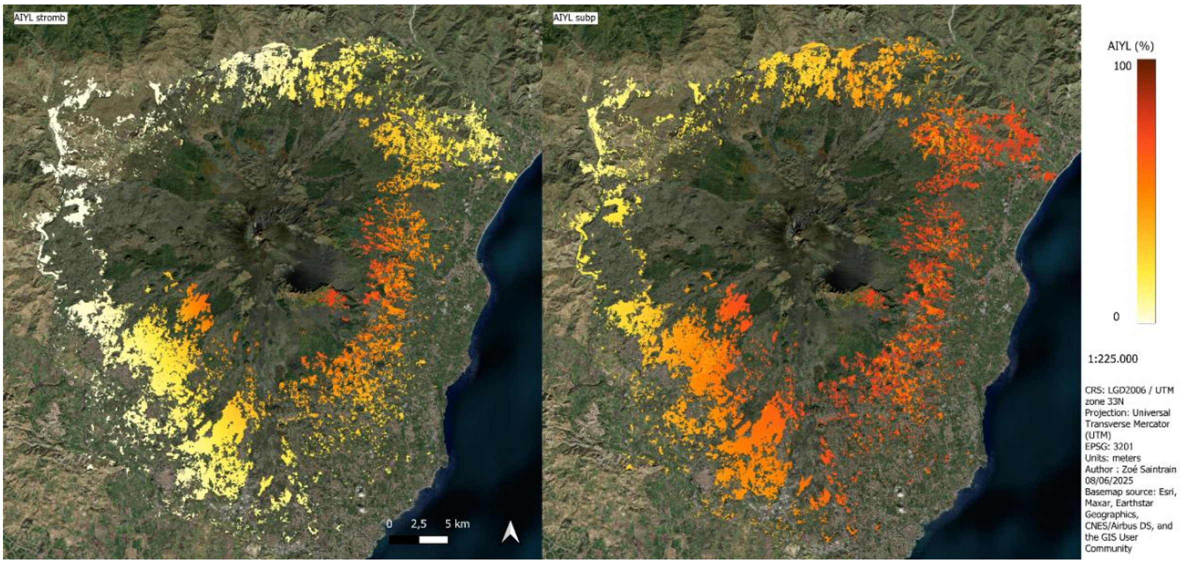

Figure 38. Spatial distribution of AIYL across the studied agricultural area from the 1000 simulations model, VEI 2 (left) and VEI 3 (right) eruption scenarios.

Figure 39. Distribution of the Annualized Index of Yield Loss (AIYL, %) over the agricultural area, from the 1000 simulations model under the VEI 2 and VEI 3 scenarios.

In contrast, the VEI 3 distribution (right) is both more symmetrical and more concentrated, with distinct peaks around 50%, 60%, and 75%. This pattern suggests that a large proportion of the agricultural area is repeatedly and significantly impacted under VEI 3 conditions, resulting in a more uniform exposure to high yield losses.

Overall, the comparison of AIYL distributions highlights two key distinctions: VEI 3 eruptions lead to higher and more consistently severe yield losses across space, whereas VEI 2 eruptions cause more variable but generally lower impacts. This visual contrast reinforces the greater spatial extent and intensity of the hazard associated with VEI 3 events.

5.4. Comparative analysis of crop types

After examining the average yield losses across the entire agricultural area, we then assessed the mean yield loss per crop type (Figure 40; Table A7). The results reveal distinct temporal patterns among olive trees, orchards, and vineyards, reflecting differences in phenological calendars, vulnerability profiles and spatial exposure to tephra fall.

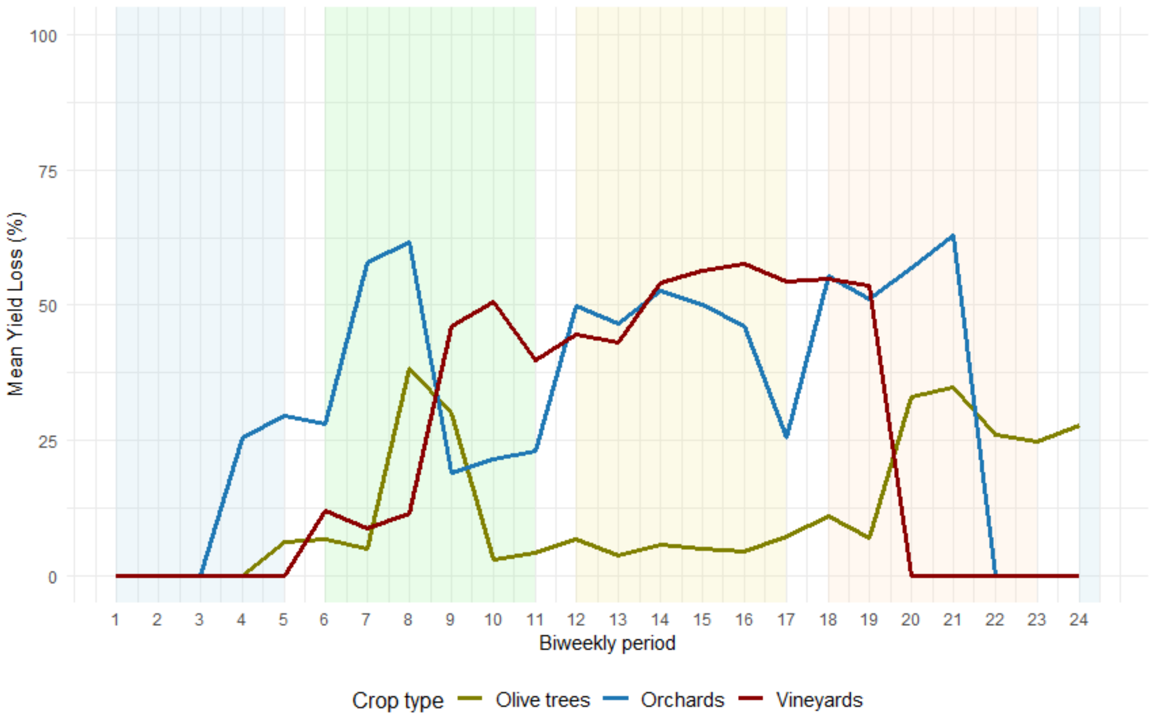

Figure 40. Mean and standard deviation of crop yield loss per studied crop, by biweekly period, from the 1000 simulations model under the VEI 2 scenario.

Orchards are the first to exit dormancy, entering the growth phase as early as period 4, followed by olive trees in period 5. Consequently, orchards are the initial contributors to yield loss, with marked impacts during early spring. In the first half of spring, orchards exhibit the highest losses, peaking throughout April (periods 7 to 8), which aligns with their flowering stage. A similar vulnerability-driven peak is then observed for olive trees in periods 8 to 9, and for vineyards in periods 9 to 10, both also coinciding with their respective flowering stages.

From late spring to early winter (periods 11 to 21), olive trees consistently show lower average yield losses, typically below 10%, despite sharing the same fragility function as orchards.

From mid-summer through early autumn (periods 14 to 19), vineyards experience the highest yield losses among all crops, despite orchards exhibiting comparable levels of vulnerability during this period. In the final phase of the year (periods 20 to 21), orchards again become the dominant contributor to yield losses, as their extended harvest period overlaps with the autumnal tephra fall exposure.

The distribution of the Annualized Index of Yield Loss (AIYL) varies markedly across the three crop types (Figure 41). Olive trees display a right-skewed distribution, with most values concentrated at low AIYL levels and a rapid tapering above 20%, indicating that most olive-growing areas experience limited annual losses. Vineyards exhibit a broader distribution, with most values remaining below 60% and a dominant concentration under 30%, suggesting more variability. In contrast, orchards show the most heterogeneous profile, with a notable proportion of pixels experiencing AIYL values exceeding 40%, despite a density peak near 0%.

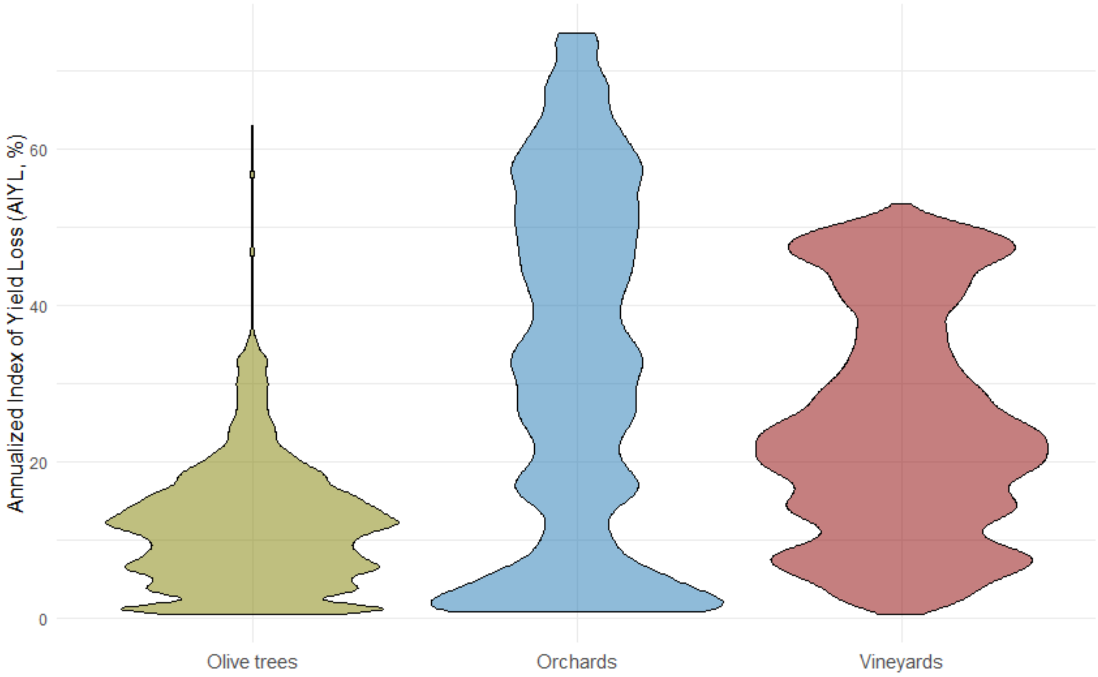

Figure 41. Distribution of the Annualized Index of Yield Loss (AIYL, %) over the different crops, from the 1000 simulations model under the VEI 2 eruption scenario.

The distribution of AIYL across different crop types is primarily driven by their geographic location, and therefore their exposure to tephra fall (Figure 16). Olive groves are predominantly located southwest of the crater, a region that is generally less affected by tephra deposition. In contrast, orchards and vineyards are situated in areas more frequently impacted by tephra fall. Orchards tend to be located at higher elevations and closer to the crater, particularly on its eastern flank, where tephra deposition is typically more intense. Although orchards are found all around the volcano, their concentration is highest to the east. Vineyards, on the other hand, are more evenly distributed between the eastern and northern sectors. Since the northern flank tends to receive less tephra, vineyards are comparatively less exposed to tephra fall than orchards. This spatial configuration explains the observed differences in average yield losses among the three crop types.

5.5. Comparative analysis of seasons

The distribution of the Seasonal Index of Yield Loss (SIYL) reveals clear seasonal differences in the severity and spatial extent of crop damage (Figure 42). Spring and summer are associated with the highest yield losses, with broad and heterogeneous distributions indicating a wide range of impacts across the agricultural landscape. The VEI 3 scenario shows particularly destructive effects during these seasons, with SIYL values frequently approaching 100%, while the VEI 2 scenario results in lower losses with a peak around 0.

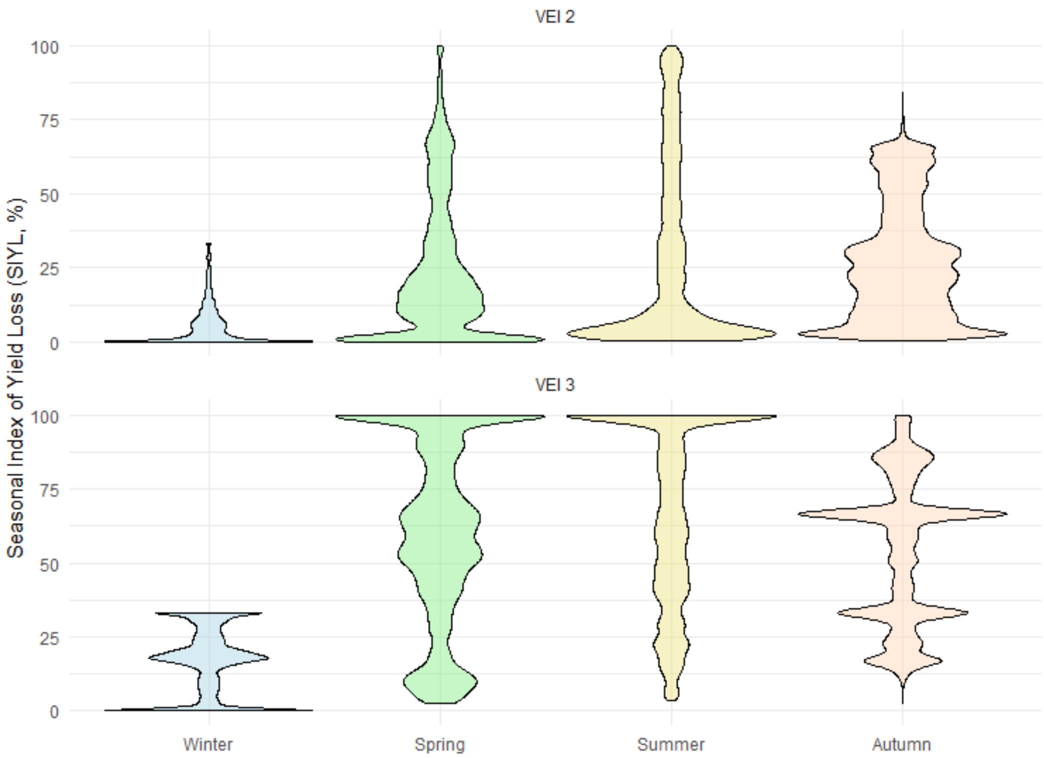

Figure 42. Distribution of the Seasonal Index of Yield Loss (SIYL, %) from the 1000 simulations model under the VEI 2 and VEI 3 scenarios.

Winter appears to be the least damaging season under both eruption scenarios, with SIYL values concentrated near zero and a maximum not exceeding 40%. However, under the VEI 3 scenario, a distinct density peak is observed around intermediate SIYL values, suggesting that some areas still experience moderate losses. In autumn, losses are generally lower for both eruption types, though the VEI 3 scenario again reaches values above 60% and extends up to 100%, whereas the VEI 2 scenario produces more moderate and narrowly.

6. Discussion

6.1. The integration of previously isolated datasets enables the spatial and temporal quantification of risk

Until now, data on crop vulnerability to tephra fall, phenological calendars, tephra deposition simulations and agricultural land use mapping existed but were used separately to assess impact of tephra fall on crops. The present study integrates these different datasets within a modelling framework, enabling the explicit spatial and temporal quantification of the risk of crop production loss from tephra fall. This combined approach, which goes beyond the mere juxtaposition of isolated information, allows the observation of several phenomena that were previously undetectable.

6.2. The model enables multi-scale risk assessment

Spatial risk assessment outperforms vulnerability- or hazard-only approaches and reveals both expected and unexpected patterns of agricultural loss

At the scale of the entire agricultural area, all AIYL spatial distributions (Figure 35; Figure 38) reveal that the eastern flank of Etna is the most frequently affected area, with AIYL values systematically higher than in other parts of the volcano. In the IM model at 50% exceedance probability, losses on this flank dominate the impact pattern, while the rest of the volcano shows AIYL values close to 0. This spatial asymmetry aligns with established knowledge on tephra dispersion around Mount Etna, where the eastern and southeastern flanks are most frequently exposed to tephra fallout due to the predominance of westerly winds and a thermal depression that channels the volcanic plume toward these slopes (Chester et al., 2010; Soldati & Marchetti, 2017). Such spatial differences in yield loss underscore the added value of spatial risk assessment over vulnerability-only approaches in addressing agricultural losses from tephra fall.

In addition, the results show that the eastern flank is not the only area at risk. The AIYL maps from the IM model for deposits with 10% of exceedance probability reveal losses of up to 70% on the southwestern and northeastern flanks. The 1000 simulations model confirms this broader spread, with high AIYL values extending from the eastern sector toward other slopes. This highlights another benefit of spatial assessment: identifying zones that might not initially be suspected to be at high risk, even when they fall outside the most frequently impacted areas.

Spatial and temporal assessment outperforms exposure information by identifying how each crop sector's contribution to total agricultural loss and evolves over time

Violin plots of AIYL by crop type from the 1000 simulations model show that different crops are impacted to varying degrees and therefore contribute differently to total agricultural loss. Orchards record the highest AIYL values, vineyards show a lower maximum AIYL but a higher proportion of pixels above 40%, and olive trees have mostly low AIYL values, with the majority below 40%. As mentioned in Section 5.4, this pattern is largely explained by their location around the crater.

The mean yield loss curves by crop type (Figure 40) provide another layer of analysis, showing that the hierarchy orchards > vineyards > olive trees in the contribution to global crop yield loss does not always hold. Each crop's contribution to total loss varies over time: orchards dominate in early spring, vineyards in late spring and olive trees in late autumn, with several periods where the curves intersect. These variations can only be observed through the spatial projection of combined crop-specific fragility functions and phenological calendars, which captures both the temporal shifts in vulnerability and the geographic distribution of crops.

At the agricultural plot scale, spatial and temporal risk assessment reveals yield loss differences under identical tephra load conditions

At an even finer scale, the model makes it possible to detect differences in risk between individual agricultural parcels within a zone receiving a homogeneous tephra deposit. Figure 30 illustrates this for the tephra deposit from the 10% probability isomass map alongside the resulting losses in periods 4, 9, 12, and 23. The common feature of these periods is that the three studied crops are not at the same phenological stages (Table 7). As a result, crops subjected to the same deposit experience different levels of yield loss. Such detailed insights at the parcel scale are only possible through the integration of spatial and temporal dimensions in the risk assessment framework.

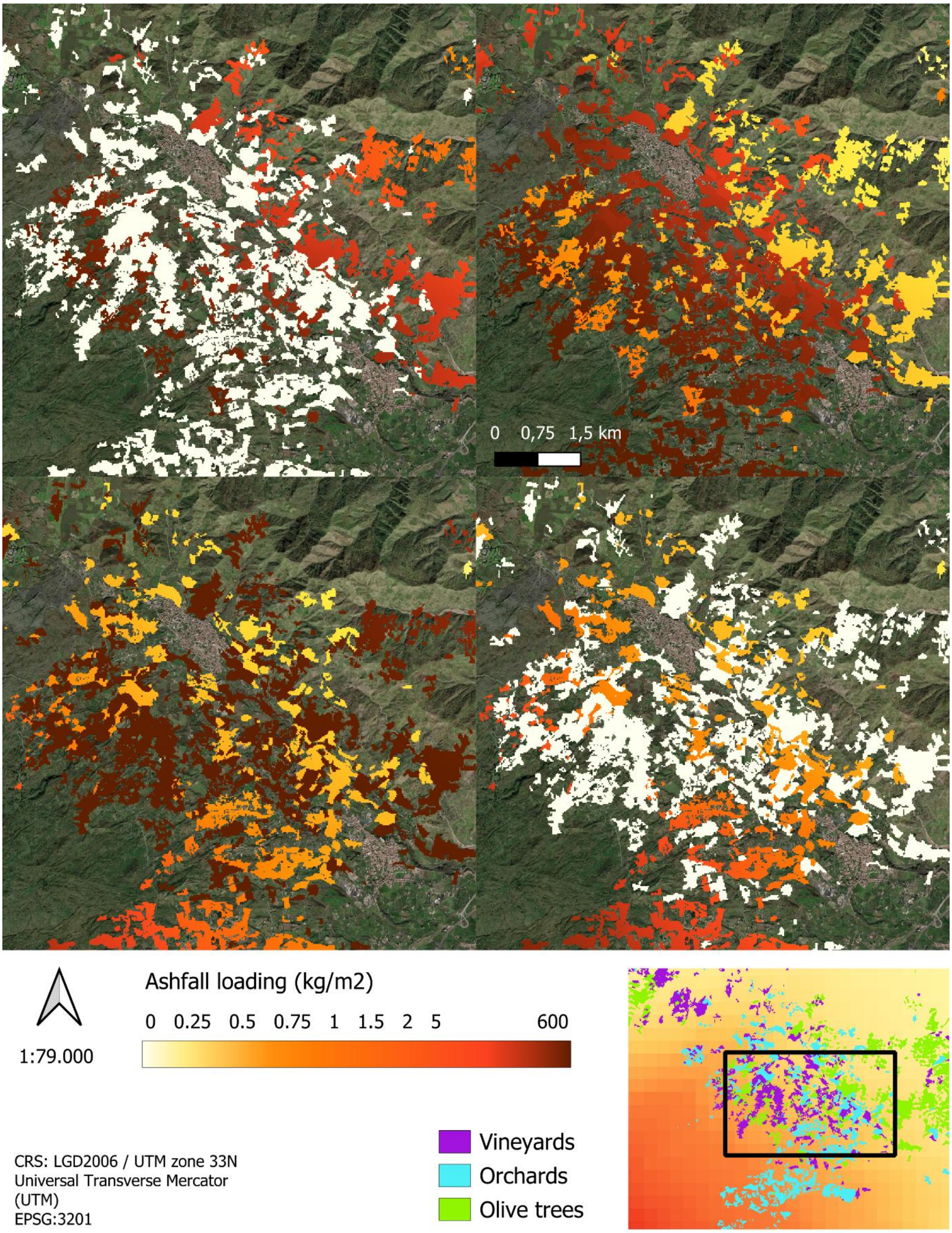

Figure 43. Ashfall deposit from 10% probability isomass map, VEI2 eruption scenario (bottom right) and resulting yield losses from the IM model in periods 4, 9, 12, and 23. (23 top-left, 12 top-right, 9 bottom left, 4 bottom right)

6.3. Incorporating wind dynamics in spatial and temporal risk assessment reveals more realistic loss spatial distribution and loss variability within periods of constant vulnerability

Effects on Mean Yield Loss

On the graph of mean crop yield loss across the agricultural area from the IM model (Figure 43; Figure 32), the mean remains constant during consecutive periods with unchanged phenological stages. This is expected because, in this model, tephra deposits (probability isomass maps) are fixed throughout the year. As a result, loss variations are solely dictated by changes in vulnerability. The influence of seasonal wind patterns on tephra dispersion (and therefore yield loss) is not visible.

In contrast, in the 1000 simulations model, mean losses vary even within periods of constant vulnerability, reflecting changes in the spatial distribution of tephra deposits over time. This can be observed in Figure 33 showing mean losses for the VEI 2 eruption scenario and is even more pronounced in Figure 34 for the VEI 3 scenario. Within periods 12 to 16, phenological stages remain constant, yet mean losses range from a maximum of 79.1% to a minimum of 57.5%, a difference of more than 20% despite identical vulnerability. This highlights the significant influence of wind-driven tephra fall variability on mean yield losses, even when crop vulnerability remains unchanged.

Difference in models' output

Although they do not incorporate wind dynamics, probability isomass maps in the IM model have the key advantage of providing a probabilistic quantification of losses: yield losses are associated with exceedance probabilities for several severity levels (10 %, 25 %, 50 %, 75 %, and 90 %). In contrast, the 1,000 simulations model produces yield loss estimates for mean tephra loadings per period without associated probabilities. The key distinction between risk assessment and impact assessment lies in this probabilistic approach: in risk assessment, a range of possible impact scenarios is provided, each with an associated probability (Wilson et al., 2014). In this regard, the 1000-simulations model in its current form aligns more closely with an impact assessment than a risk assessment.

Effect on yield loss spatial distribution

Although probability isomass maps accurately depict the likelihood of tephra deposits exceedance, they do not reflect the actual spatial pattern of tephra fall from an individual eruption. In reality, the tephra deposit distribution from a specific event will never match the probabilistic aggregation of 1,000 simulated deposits. In this regard, the 1,000 simulations model has the advantage of representing losses from realistic tephra deposition patterns. It also enables a finer prediction of how losses evolve spatially from one period to the next, as deposition patterns change with seasonal wind conditions.

This is illustrated in Figure 44, which shows the spatial distribution of crop yield loss from the 1000 simulations model for the VEI 2 eruption scenario during periods 12, 13, 14, and 15 on the north-eastern flank of the volcano. Unlike the periods shown in Figure 43 (periods 4, 9, 12, 23), these four consecutive periods share identical phenological stages across all crops. In Figure 43, we demonstrated that crops exposed to the same tephra deposit exhibit different yield losses due to differences in phenological stage. In Figure 44 the observed spatial variations in yield loss are instead driven by changes in the spatial distribution of tephra deposition.

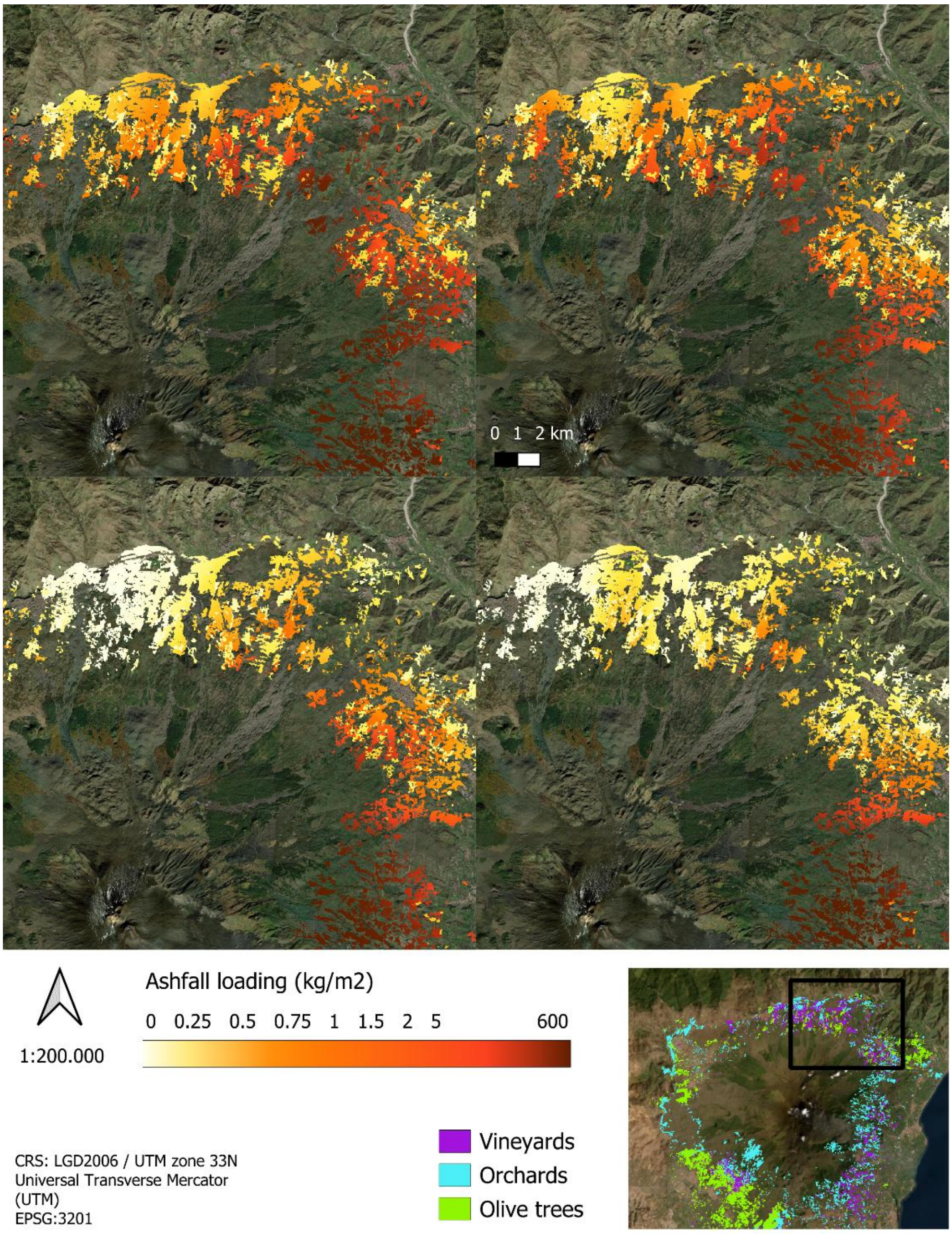

Figure 44. Crop yield losses from the 1000 simulations model, VEI2 eruption scenario, in periods 15, 14, 13, and 12. (15 top-left, 14 top-right, 13 bottom left, 12 bottom right). Unlike Figure 43, these periods have the same vulnerability and do not feature varying combinations of phenological stages.

This pattern is also showing at the scale of the entire study area as shown in Figure 45, which shows the spatial distribution of crop yield loss from the 1000 simulations model for the VEI 3 eruption scenario during periods 12, 13, 14, and 15. Apart from the eastern flank, which consistently experiences the highest possible losses from the southeast to the northeast, the other flanks display yield loss levels that vary significantly between periods despite having the same vulnerability.

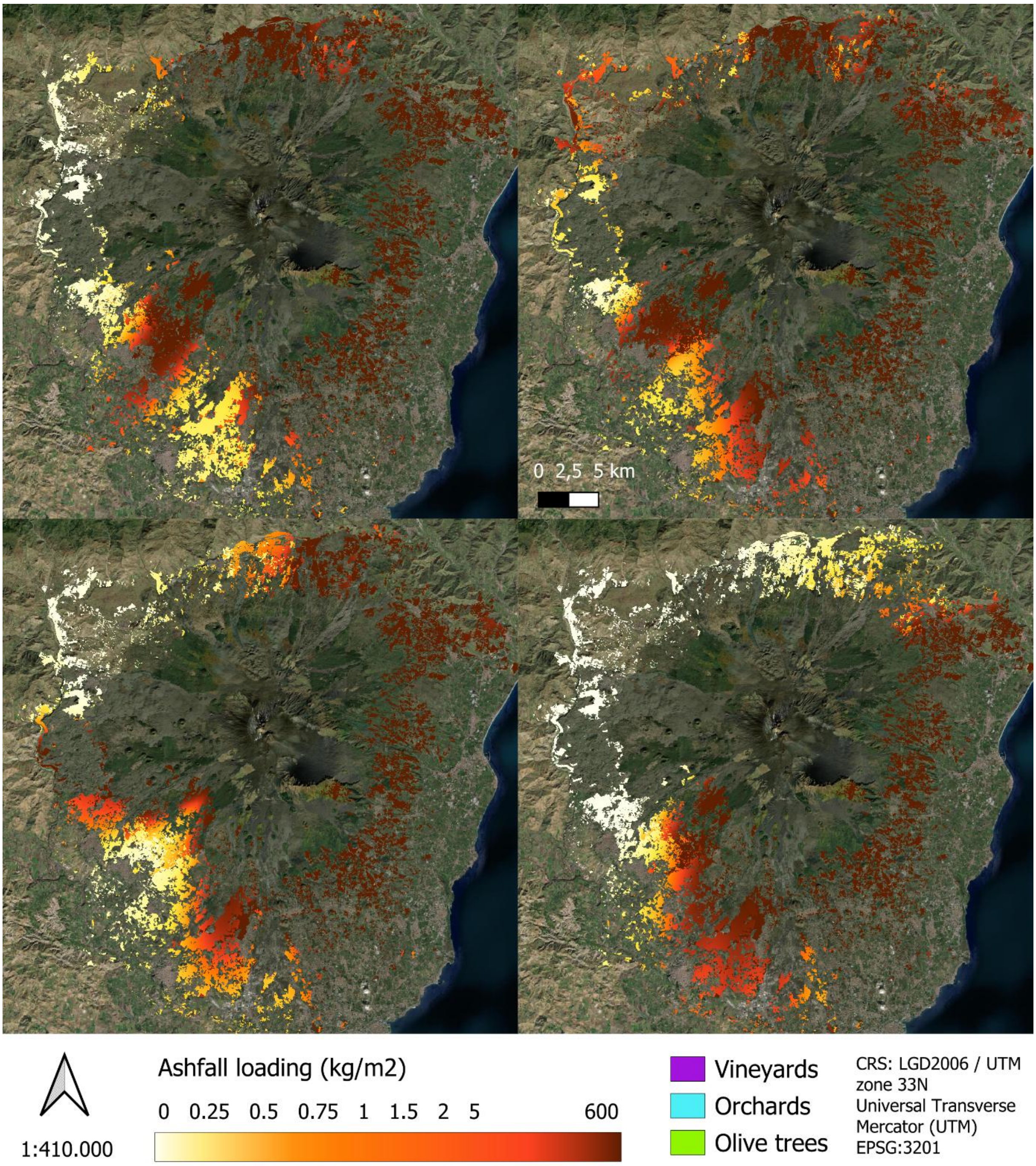

Figure 45. Crop yield losses from the 1000 simulations model, VEI3 eruption scenario, in periods 15, 14, 13, and 12. (15 top-left, 14 top-right, 13 bottom left, 12 bottom right).

Using the mean of individual tephra fall simulations as hazard provides a more realistic representation of the spatial distribution of losses compared to those from the IM model. In addition, integrating wind seasonality dynamics into spatial and temporal risk assessment enables the detection of yield loss variability driven solely by changes in tephra deposition patterns, even when crop vulnerability remains constant, both at the flank scale and across the entire agricultural area. This demonstrates the added value of the 1000 simulations model over probabilistic isomass map-based approaches.

6.4. The 1000 simulations model tends to overestimate crop yield losses

Regarding the average yield loss results over the agricultural area in the 1000-simulations model, a bias is introduced by the method used to calculate mean tephra fall. For each agricultural pixel, the deposits from all simulations who falls within a given two-week period are summed and then divided by the number of simulations in that period. Two simulations within the same period driven by different wind conditions may deposit tephra over entirely different agricultural areas. In this case, the averaging process then extends the tephra-affected zone to the combined area covered by both simulations, with lower tephra fall values assigned to each pixel.

In the case of the strombolian eruptive scenario used to simulate the tephra fall from a VEI 2 event, this effect is negligible. This scenario is long-lasting, with a minimum duration of 96 hours, which is well above the 6-hour maximum single-simulation duration in TephraProb before wind data are updated. As a result, even within a single simulation, wind direction can shift, producing naturally diffuse and spatially extensive tephra deposits (Figure 18). Consequently, the averaged tephra deposit per period causes a minor expansion of the affected area (Figure 46).

By contrast, sub-Plinian eruptions are short-lived, here lasting no more than 2 hours. In TephraProb, short-lasting events are fully simulated using a single wind dataset, resulting in narrow, concentrated tephra deposit footprints (Figure 19). When deposits from multiple sub-Plinian simulations in the same period are averaged, the affected area is artificially enlarged to include the union of all footprints, while deposit values are reduced (Figure 47). Given the fragility functions' sensitivity to low tephra loads, this artificial spatial expansion produces yield loss estimates that are higher than what would be expected from a single, isolated sub-Plinian event.

This suggests that the differences in mean yield losses over the agricultural area within periods sharing the same phenological stages for the VEI 3 sub-Plinian scenario are more likely influenced by the extent of footprint expansion: that is, whether the simulations occurring within the same two-week period are oriented very differently around the crater. A more appropriate approach would be to calculate the mean loss over the agricultural area for each period by averaging the yield losses from individual simulations rather than computing losses from mean tephra loads. However, this does not include the possibility of producing spatial representations of mean loss. A promising future direction would be to adapt the 1000-simulations model into a probabilistic framework by generating probability isomass maps for each biweekly period, based on all simulations occurring within that timeframe. This would preserve spatial information while addressing the overestimation bias in short-duration eruptive scenarios.

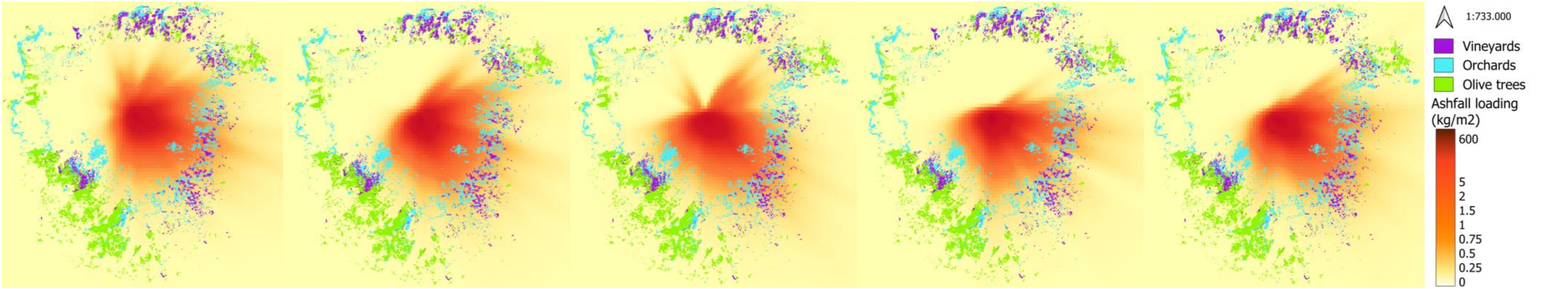

Figure 46. Mean ashfall deposits (kg/m²) for biweekly periods 4 to 8 from the VEI 2 strombolian eruption scenario.

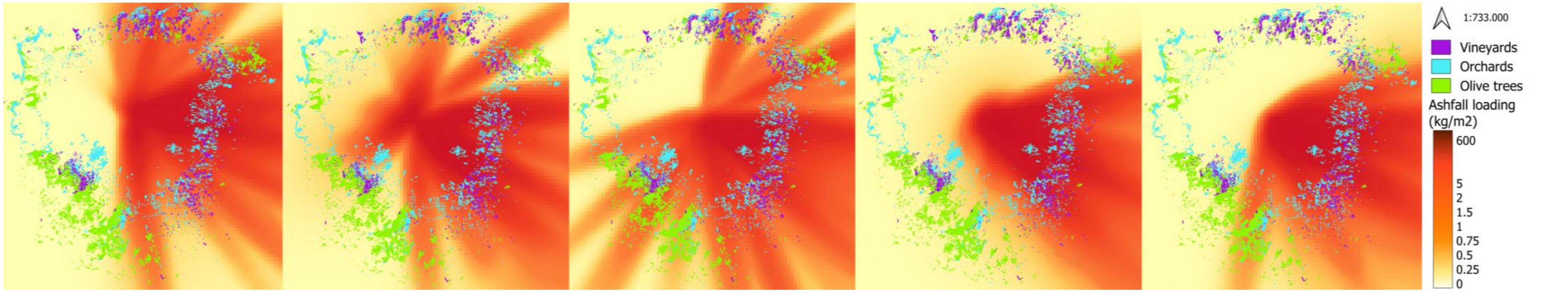

Figure 47. Mean ashfall deposits (kg/m²) for biweekly periods 4 to 8 from the VEI 3 sub-Plinian eruption scenario. Compared to the narrow and concentrated single-event footprints, these mean deposit maps illustrate how averaging across multiple simulations within the same period artificially enlarges the affected area while lowering ashfall intensity per pixel, a process that can overestimate yield losses when using fragility functions sensitive to low ashfall loads.

6.5. The vulnerability assessment also introduces sources of uncertainty

The main challenge in conducting the seasonality and vulnerability assessment was first the limited availability of data.

Crop calendars

The development of crop calendars for the crops in the studied area would have ideally required recent, locally sourced crop calendars. In the absence of such data, we relied on a variety of alternative sources, including technical documents on the cultivation of the same species in other Mediterranean climates, as well as information from gastronomic and wine tourism sectors. Furthermore, Craig et al. (2021) did not provide details on the relative proportions of the three species grouped under the category "orchards". Consequently, when constructing the orchard crop calendar, we combined the calendars of the three species, retaining the most sensitive growth stage for each period. This approach likely led to an overestimation of orchard vulnerability, as grouping the three species in this way systematically selects the most vulnerable stage present. For example, if in a given period one-third of the orchard area (one species) is in the harvest stage and the remaining two-thirds (two species) are in maturation, the method records the entire orchard area as being in harvest. In reality, only a fraction corresponding to the actual cultivated area of that species is in that highly sensitive stage.

Fragility functions

The fragility functions developed in this work based on the Ligot et al. (2024) post-impact assessment dataset reveal fundamentally different levels of crop vulnerability to tephra fall with those proposed by Craig et al. (2021), which are the most comprehensive and recent fragility functions available in the literature. Regarding fruit trees fragility functions for moderate vulnerability stages (growth, maturation, and harvest), Craig et al. (2021) indicate that at a tephra deposit of 100 mm, the probability of reaching 76.5% production loss remains below 20% (Figure A5). In contrast, our functions indicate that such levels of yield loss are reached with tephra loads of less than 10 kg/m² (Figure 25; Figure 27; Figure 28). Given that 1 mm of tephra corresponds to 1 kg/m² (Eychenne & Le Pennec, 2012) and that yield and production loss are equivalent in Craig et al. (2021), this reflects a much higher vulnerability in the functions derived from the Ligot et al. (2024) dataset. At the maximum vulnerability stage (flowering), Craig et al. (2021) report that at 100 mm of tephra, the probability of reaching 90% loss remains below 20% (Figure A3). In contrast, our fragility functions during the flowering stage indicate that such losses occur at just 1 kg/m², again pointing to a substantially greater vulnerability (Figure 26). A similar pattern emerges for viticulture: the functions of Craig et al. (2021) indicate lower overall vulnerability than those developed here. Moreover, Craig et al. (2021) consistently show vineyards to be more vulnerable than fruit trees at all phenological stages, whereas the present functions indicate that vineyards may be equally, less or more vulnerable than fruit trees depending on the phenological stage. A review of the material and methods of Craig et al. (2021), available in the Appendix, provides some explanation for these differences (Section 8.2).

Although effort was made to develop fragility functions that approximate the real-world vulnerability of crops to tephra fall, the model remains open to improvement. While the dataset used here is somewhat more extensive and more methodologically consistent in data collection than that employed by Craig et al. (2021), it is still too limited in size to be considered an objective representation of reality. In particular, the available data are restricted to relatively low tephra loads, making it difficult to determine the precise threshold at which 100% loss occurs. In the present model, the parameter *b* was fixed at 100, resulting in a steep progression toward total loss. In reality, losses may plateau before reaching 100%, especially in the absence of observations at higher deposit levels. Addressing this limitation will require future work based on substantially larger and more comprehensive datasets.

Another limitation of this work is that it does not account for all components of agricultural yield loss risk, whether volcanic or non-volcanic. Factors such as tephra grain size, environmental conditions, plant traits and crop phenological stage have been identified as key factors of crop yield loss (Ayris & Delmelle, 2012; Ligot, Bogaert, et al., 2022; Ligot, Delmelle, et al., 2022; Ligot, Guevara, et al., 2022; Wilson et al., 2015), yet their effects remains insufficiently quantified. This may be due to a lack of observational data and incomplete descriptions of tephra fallout properties, where tephra thickness is typically the only HIM reported (Ligot, Viera, et al., 2024).

6.6. Applications

Tailoring insurance schemes

Identifying the general risk level for broad zones, as provided by AIYL estimates, can enable insurance companies to adapt their coverage options according to a client's position around the crater. For such purposes, insurers do not require high-resolution, month-to-month variations in impact risk. Instead, they need an assessment of the overall damage level to which assets are exposed over extended time horizons, along with the probability of such damage occurring (Friedman, 1984). This information is essential for designing compensation schemes, evaluating the financial viability of insuring a given area, and determining whether risk levels are so high that coverage would be prohibitively expensive. In this context, the IM model is particularly well suited, as it produces yield loss estimates for different tephra fall severities, each linked to a specific probability of exceedance, thereby providing the probabilistic framework required for insurance-related decision-making.

Public impact management

For public aid allocation, identifying which agricultural sectors are most affected during the year, as provided by the mean yield loss for each crop type, enables authorities to adjust compensation schemes between different agro-industrial sectors impacted by hazardous events. Given the significant contribution of the agri-food sector to the local economy (CREA, 2024a), it is essential to determine which sectors will be most affected so that support measures can be prioritised accordingly. Such information can help optimise the distribution of public resources, ensuring that the most vulnerable sectors receive adequate compensation and that recovery strategies are tailored to the specific structure of local agricultural production.

Agricultural management

Identifying high-risk parcels within an agricultural area is particularly valuable for farmers, who are primarily concerned with the risks to their own holdings. This knowledge allows them to prioritise investments in costly mitigation measures, ensuring they are implemented where they will be most effective rather than uniformly across all fields. For this purpose, the 1,000-simulations model is especially suited, as it provides a fine-scale risk analysis that incorporates seasonal wind dynamics and crop phenology. This enables farmers to assess whether their specific parcel is likely to be affected and to time their protective actions accordingly.

7. Conclusion

This study presents a methodology for spatial and temporal quantification of crop yield loss risk from tephra fall, integrating the three core components of risk assessment: exposure, vulnerability, and hazard. Two models are developed, differing in hazard data treatment. The "IM" model uses probabilistic isomass maps to estimate yield loss for various tephra deposit levels, each with an associated probability of exceedance. The "1000 simulations" model applies biweekly mean tephra deposits, producing yield loss estimates without probability values but incorporating wind seasonality.

This approach enables the first quantification of crop yield loss risk from tephra fall at the scale of an entire agricultural area within 30 kilometres of a volcano. Results analysis show that the integrated framework outperforms the isolated use of hazard, exposure or vulnerability data in impact assessment.

The AIYL spatial distribution highlights the eastern flank as consistently most impacted, with a decreasing gradient of AIYL from east to west and from proximal to distal crop areas. This improves upon vulnerability assessments, which assume equal impact for different areas of the same crop at the same phenological stage and upon hazard assessments, which typically identify only the eastern flank near the Valle del Bove as high-risk. Biweekly yield loss maps reveal that agricultural plots within a homogenous hazard zone can be affected to different extents, surpassing hazard maps that only indicate tephra fall spatial distribution without intra-zone impact variability. Violin plots of AIYL by crop type (olive trees, orchards, vineyards) highlight sector-specific impact differences, while biweekly mean crop yield losses over the entire area of study show how each crop type's contribution to total loss varies seasonally. This demonstrates that impact is not solely determined by a crop's proximity to the volcano.

Results from the 1000 simulations model demonstrate that integrating wind seasonality increases variability in yield loss magnitude and spatial distribution patterns, showing that losses depend not only on hazard magnitude and phenological stage but also on wind conditions. However, analysis reveals a bias from using biweekly mean deposits: if tephra fall simulations within a period are driven by differing wind directions, the resulting impacted area (and average crop yield loss) can be overestimated.

A promising improvement would be to adapt the 1000 simulations model into a probabilistic framework by generating period-specific probability isomass maps from all simulations within each biweekly interval, thus preserving spatial detail while reducing overestimation in short-duration eruptions. Further enhancements include refining vulnerability assessment with fragility functions of lower uncertainty and incorporating additional impact factors, volcanic or non-volcanic (e.g., rainfall before/after tephra fall, grain size, temperature, drought). A final step would be to make fully probabilistic, namely considering the probability of occurrence of eruption scenarios with different magnitudes.

8. Appendix

8.1. Eruption source parameters sampling distribution

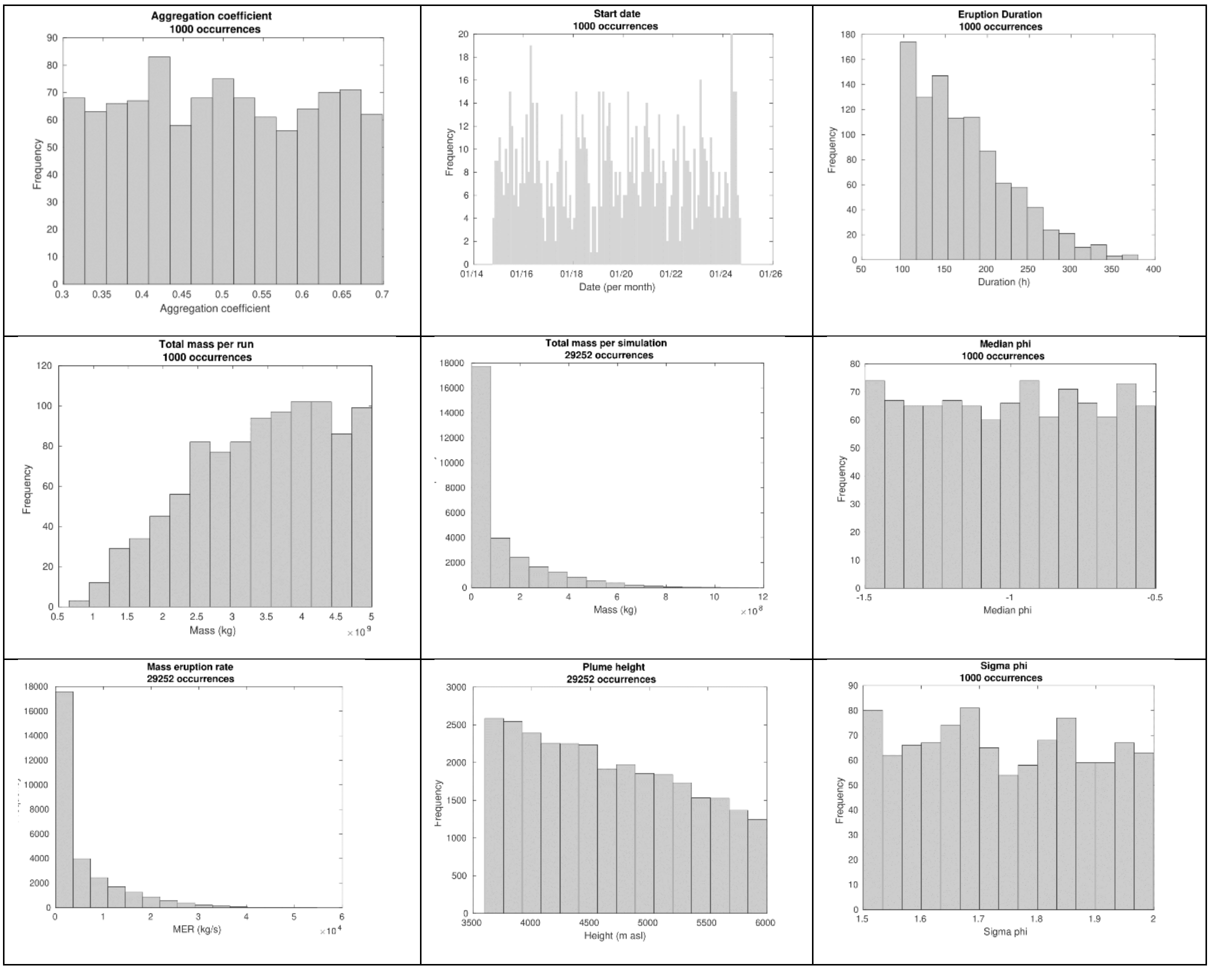

Figure A1. VEI2 eruption scenario eruption source parameters sampling distribution

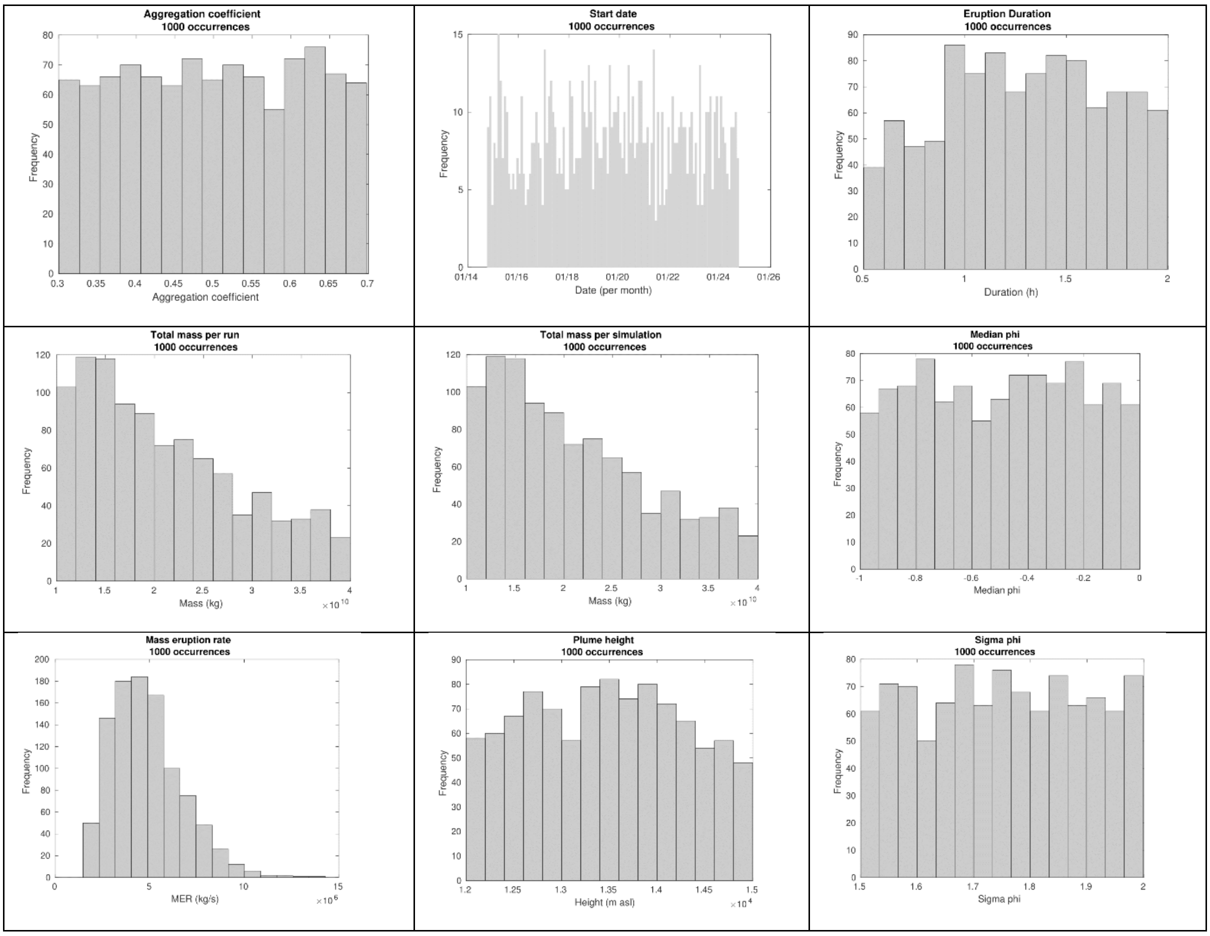

Figure A2. VEI3 eruption scenario eruption source parameters sampling distribution.

8.2. Review of the methodology and dataset underpinning fragility functions from Craig et al. (2021)

Craig et al. (2021) divided the agricultural sector into three sub-sectors: pastoral farms, forestry and horticulture. The horticulture sub-sector includes seven crop types according to plant morphology and edible part: non-tree fruits, tree fruits, leafy vegetables, cereals, root vegetables, viticulture and paddy. The authors developed Impact State (IS) schemes for each sub-sector. They define multiple levels of crop disruption severity, based on the magnitude of observed production loss. They were developed "based on previous empirical data and impact assessments" (Cook et al., 1981; Craig et al., 2016; Cronin et al., 1998; Eggler, 1963; Thorarinsson & Sigvaldason, 1972; Wilson & Kaye, 2007; Wilson et al., 2011). Table A1 presents the IS scheme defined for the horticultural sub-sector (Craig et al., 2021).

IS	Description	Effects on production	Damages
0	No disruption	No production change.	No damage.
1	Some disruption	Slightly lower productivity but recoverable harvest.	<75% vegetation covered.
2	Moderate disruption	Up to 30% production loss	Some plant breakage and damage to crops within the impacted farm; possible acid burns (due to acidic leachates coating the tephra and damaging plant tissue when in contact) and abrasion.
3	High disruption	Rinsing/mitigation needed, ~60% production loss.	Most crops within impacted farms sustain some physical damage (i.e. breakages, vegetation damage, etc.).
4	Total loss of capabilities	>90% reduction in yield; >1 season to recover.	All crops within the impacted farm damaged in some way. Possible damage to farm buildings.

Table A1. Impact state scheme for the horticultural sub-sector. Adapted from Craig et al. (2021).

Production and yield loss percentages associated with each IS were determined "by groupings of empirical data and the production losses reported, rather than being arbitrarily defined" (Craig et al., 2021). Details on the methodology underpinning these estimates is not available.

Based on data derived from post-impact assessment studies that report both the thickness of the tephra deposit (HIM) and the associated production losses (impact measure), the authors determine the probability of reaching or exceeding specific IS.

Data processing and probability calculation for reaching or exceeding Impact States (IS)

The data points were categorized depending on the crop's vulnerability level at the time the eruption occurred: Low, Moderate or Full. Only full vulnerability data points were used to develop the fragility functions. They were organized by decreasing compacted tephra thickness (mm) and grouped into 'bands'. The bands represent intervals of tephra thickness, each designed to contain approximately the same number of observations (Table A2). For each tephra thickness interval, the proportion of observations reaching or exceeding a given IS provided the probability value (y-axis). The median tephra thickness within each band served as the corresponding Hazard Intensity Measure (HIM) (x-axis).

Crop type	Tephra thickness (mm)		Number of observations per IS						Observation origins (eruptive vent)
	Intervals	Median	0	1	2	3	4	Total	
Tree fruit	1-20	13	3	1	0	1	0	5	Tungurahua, Ecuador; Merapi, Indonesia
	21-99	50	0	1	2	3	0	6	Merapi, Indonesia
	100-500	350	0	0	1	3	2	6	Mt. St. Helens, USA; Merapi, Indonesia
Viticulture	1-10	2	1	1	1	0	0	3	Etna, Italy; Ruapehu, NZ
	11-100	50	0	0	2	1	1	4	Etna, Italy
	101-500	200	0	0	0	1	3	4	Etna, Italy

Table A2. Tephra thickness bands and data observed within each band for tree fruits and viticulture. Adapted from Craig et al. (2021).

To create the functions' equations, the probability of reaching or exceeding a given impact state for each band was plotted against the band's median tephra thickness. A linear interpolation was then used to derive a function between each data point. Consequently, for each horticultural crop type, a function was developed with one curve per IS. Each of these curves is made up of 3-4 discrete linear segments, representing the relationship across the intervals between the calculated median tephra thicknesses (Figure A3Figure A4).

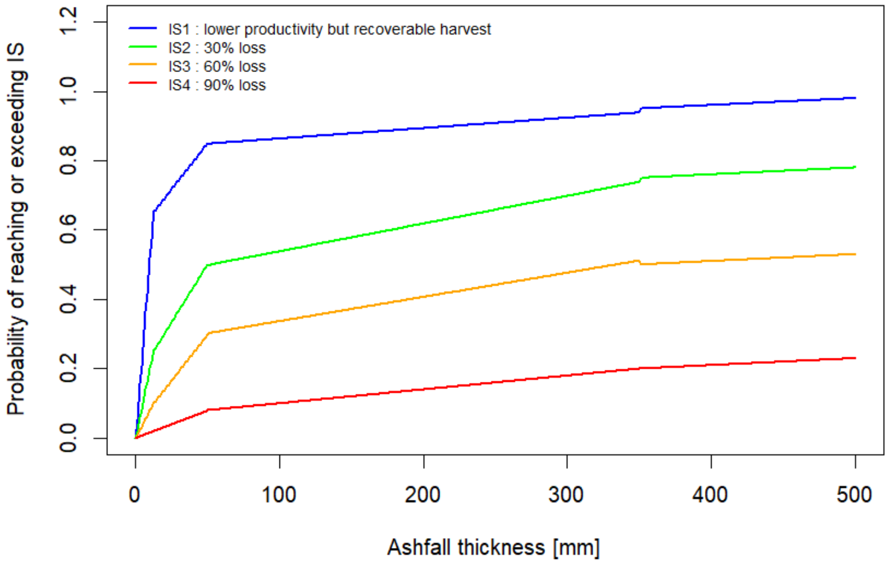

Figure A3. Fragility functions of fruit trees during the flowering stage. Vulnerability level: full. Adapted from Craig et al. (2021).

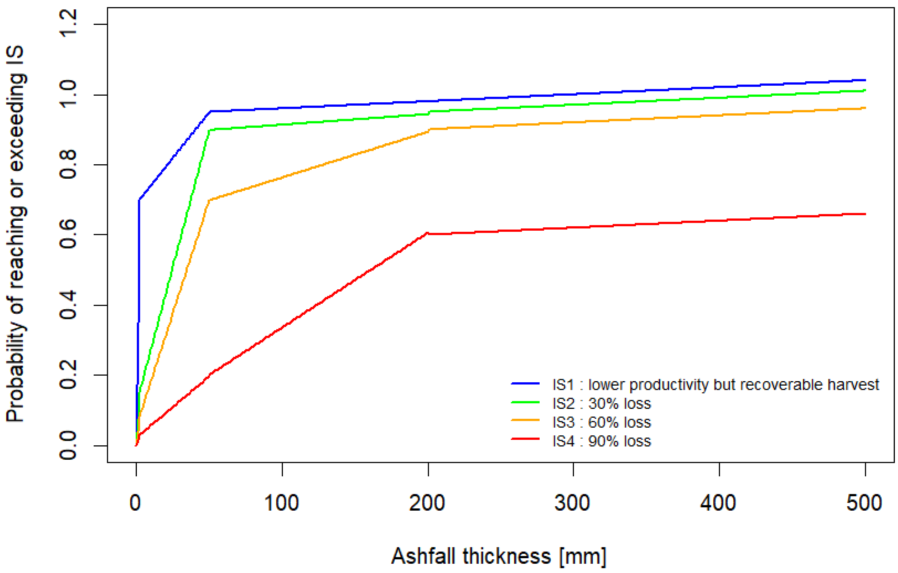

Figure A4. Fragility functions of viticulture during the flowering stage. Vulnerability level: full. Adapted from Craig et al. (2021).

Accounting for seasonality

As phenological stage is a key determinant of vulnerability, the authors account for seasonality by providing seasonal adjustment coefficients (Table A3Table A4). They are to be applied to the loss percentages associated with each IS, depending on the crop development stage or ongoing "farm activity", resulting in fragility functions adapted for every vulnerability level (Low, Moderate or Full) (Figure A5Figure A6). The methodology used to determine these coefficients is not provided in the paper.

Farm activity	Vulnerability level	Seasonal coefficient
Frost protection in place	Low	0.8
Bud burst	Moderate	0.85
Harvesting	Moderate	0.85
Pruning	Full	1
Flowering	Full	1
Germination	Full	1

Table A3. Vulnerability levels and associated seasonal coefficients, based on the New Zealand agricultural calendar, for different phenological stages and farming types for fruit trees. Adapted from Craig et al. (2021).

Farm activity	Vulnerability level	Seasonal coefficient
Pruning and maintenance (during winter)	Low	0.8
Harvesting	Moderate	0.85
Insecticide spraying	Full	1
Trimming, leaf plucking, irrigation	Full	1

Table A4. Vulnerability levels and associated seasonal coefficients, based on the New Zealand agricultural calendar, for different phenological stages and farming types for the viticulture. Adapted from Craig et al. (2021).

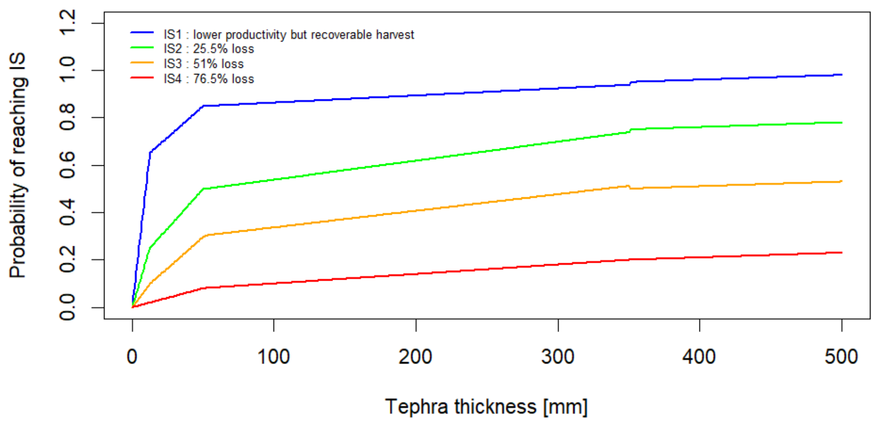

Figure A5. Fragility functions of fruit trees during the growth, maturation and harvest stages. Vulnerability level: moderate. Adapted from Craig et al. (2021).

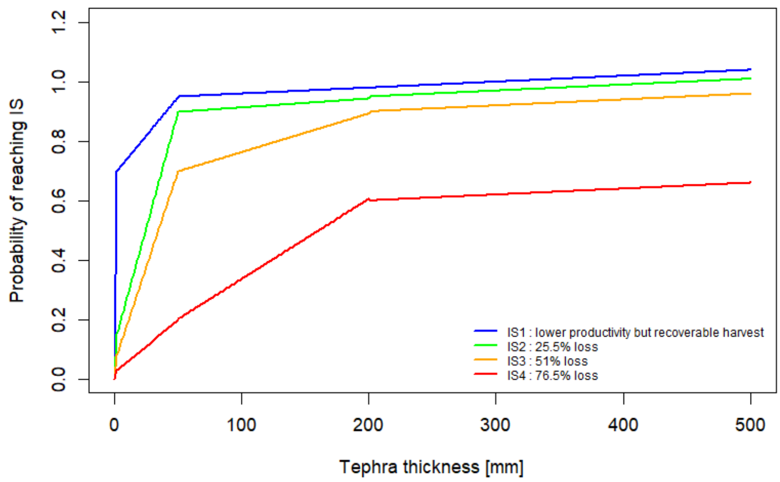

Figure A6. Fragility functions of viticulture during the growth, maturation and harvest stages. Vulnerability level: moderate. Adapted from Craig et al. (2021).

The limited dataset, specifically the small number of data points per tephra thickness interval, required adjustment of the fragility functions according to a set of rules established by experts : *"1) lines representing the probability of each IS being reached or exceeded cannot bisect each other; 2) where the tephra thickness equals zero, there is no impact, therefore no probability of the IS being reached or exceeded; 3) the probability of each IS being reached or exceeded must increase as tephra thickness increases; and 4) the probability of an IS being reached or exceeded (when tephra thickness greater than zero) cannot be zero or one, as it is not possible to know whether an impact will absolutely occur or not occur."*

As the Etna crops studied in this work are olive trees, orchards, and vineyards, the dataset used for the development of the fragility functions for fruit trees and viticulture is reviewed below.

Dataset used in Craig et al. (2021)

Fruit Trees

The fragility functions for fruit trees are based on 17 post-eruption impact data points, compiled from studies conducted around Tungurahua (Ecuador) (Sword-Daniels et al., 2011), Merapi (Indonesia) (Wilson et al., 2007) and Mount St. Helens (USA) (Cook et al., 1981). The number of data points per impact state (IS) ranges from 5 to 6, with some states observed only once (Table A2).

Data from (Sword-Daniels et al. (2011) integrates field observations, informal interviews with local farmers and governmental reports from the National Secretariat. Damage assessments covered both total and partial crop losses, though fruit trees made up a minor portion of local agriculture. Data from Wilson et al. (2007) provided field-based observations and local authority reports. Impacted crops included bananas, citrus and tomatoes, in a context of small-scale, year-round subsistence farming. Cook et al. (1981) documented limited tephra fall but noted significant effects on tree fruits, the region's primary crop.

Viticulture

Viticulture fragility function creation was based on previous vulnerability studies (Pevreal, 1993; Wilson & Kaye, 2007) and data from one empirical study on Mount Etna (Barnard, 2004), resulting in 3 to 4 data points per IS.

Data about crop loss around Mount Etna from Barnard (2004) are based on an INGV report and local media (*La Sicilia*).

Outcome of the review of the fragility functions in Craig et al. (2021)

While the fragility functions developed by Craig et al. (2021) provide a first approximation of crop vulnerability to tephra fall, they are constrained by several significant limitations. The low number of observations per impact state (often only 3 to 6) makes it difficult to derive statistically robust probabilities, especially for higher damage states. As noted by Wilson et al. (2014), fragility functions are most appropriate when all damage states are well-represented across a broad range of hazard intensities, and when datasets are sufficiently large to support statistical validity.

Impact data were partly sourced from local newspapers and governmental reports. While valuable for capturing local perceptions, such sources may be biased due to incentives to overstate agricultural losses, particularly in the aftermath of an eruption, when securing compensation or funding is a concern. This potential overestimation must be considered when interpreting fragility curves derived from such datasets.

Overall, although the functions offer a useful comparative framework, their probabilistic reliability remains limited and they should be regarded as preliminary tools, subject to refinement as more consistent and quantitatively robust datasets become available.

8.3. Fragility function curves from non-linear regression and expert adjustment

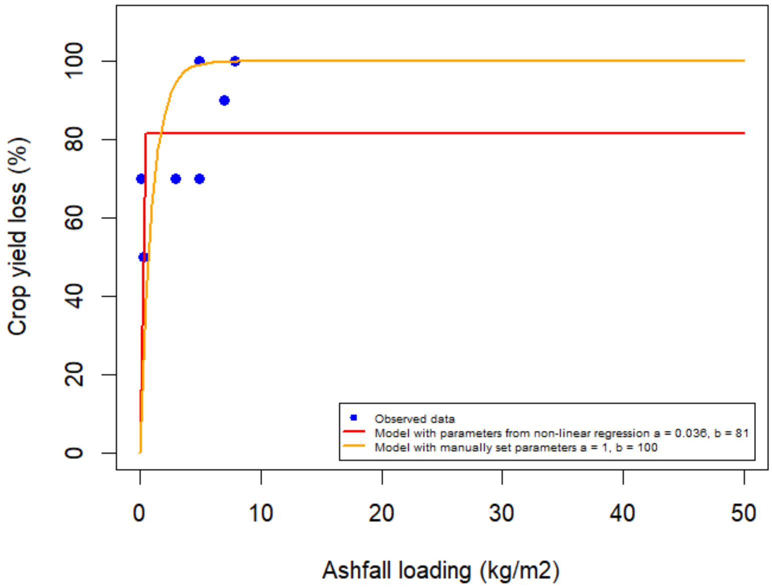

Figure A7. Fragility function for fruit trees at the growth phenological stage, generated by non-linear regression from the dataset of Ligot, Viera, et al. (2024) and manually adjusted by expert judgement.

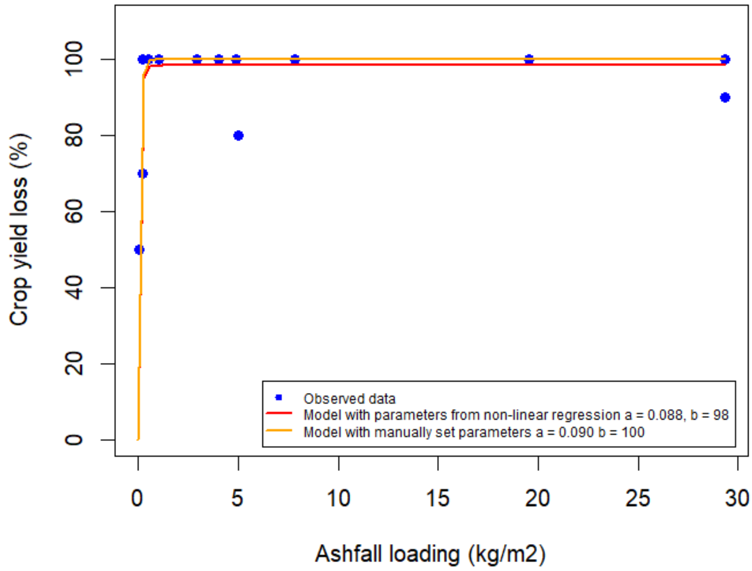

Figure A8. Fragility function for fruit trees at the flowering phenological stage, generated by non-linear regression from the dataset of Ligot, Viera, et al. (2024) and manually adjusted by expert judgement.

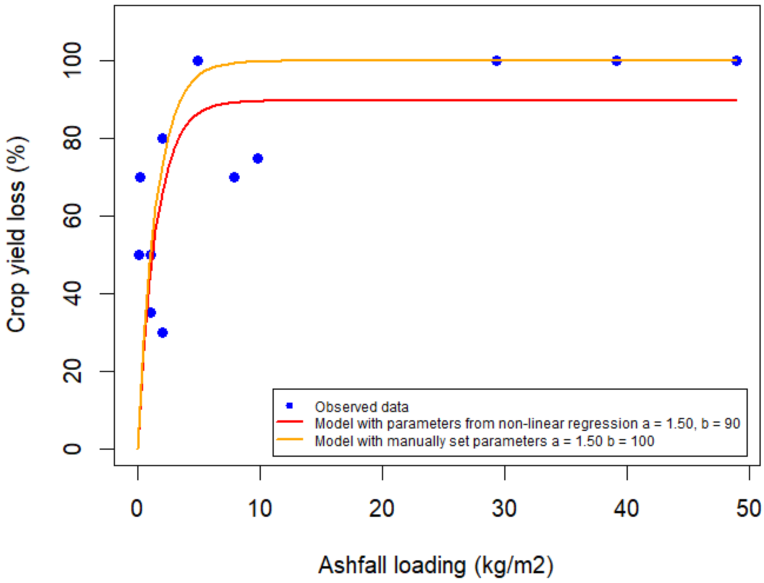

Figure A9. Fragility function for fruit trees at the maturation phenological stage, generated by non-linear regression from the dataset of Ligot, Viera, et al. (2024) and manually adjusted by expert judgement.

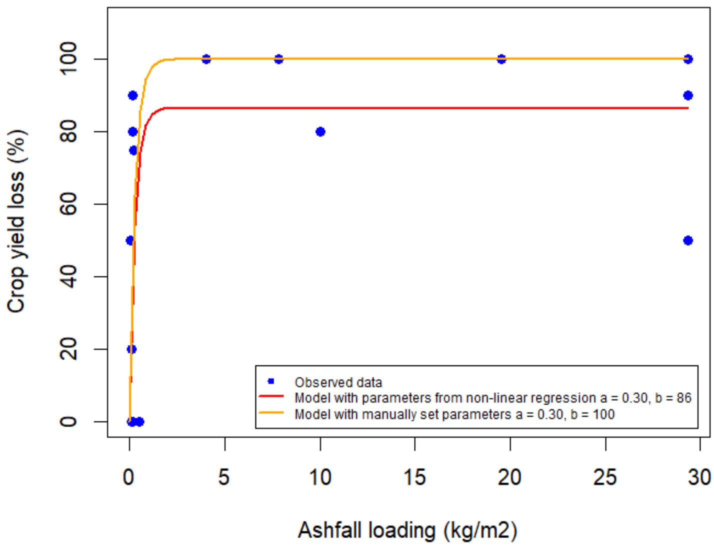

Figure A10. Fragility function for fruit trees at the harvest phenological stage, generated by non-linear regression from the dataset of Ligot, Viera, et al. (2024) and manually adjusted by expert judgement.

8.4. Link to the GitHub repository for risk model codes

Isomass maps model: https://github.com/zoesaintrain/Master-thesis/blob/main/Risque_IM.R

1000 simulations model: https://github.com/zoesaintrain/Master-thesis/blob/main/Risque_simulations_individuelles.R

8.5. Supplementary results

Period (biweekly)	VEI 2 eruption scenario			VEI 3 eruption scenario		
	10%	50%	90%	10%	50%	90%
1	0.0 ± 0.0	0.0 ± 0.0	0.0 ± 0.0	0.0 ± 0.0	0.0 ± 0.0	0.0 ± 0.0
2	0.0 ± 0.0	0.0 ± 0.0	0.0 ± 0.0	0.0 ± 0.0	0.0 ± 0.0	0.0 ± 0.0
3	0.0 ± 0.0	0.0 ± 0.0	0.0 ± 0.0	0.0 ± 0.0	0.0 ± 0.0	0.0 ± 0.0
4	16.8 ± 31.8	2.8 ± 10.3	0 ± 0.2	21.1 ± 38.4	0.9 ± 4.5	0.0 ± 0.0
5	23.3 ± 30.6	3.0 ± 10.4	0 ± 0.2	37.7 ± 40.6	1.0 ± 4.5	0.0 ± 0.0
6	28.7 ± 30.6	3.5 ± 10.5	0 ± 0.2	48.1 ± 41.2	1.1 ± 4.6	0.0 ± 0.0
7	38.4 ± 38.6	10.8 ± 26.2	0.2 ± 1.9	54.0 ± 41.9	4.7 ± 17.9	0.0 ± 0.0
8	60.5 ± 37.0	11.6 ± 26.5	0.2 ± 1.9	70.3 ± 39.7	4.8 ± 18.1	0.0 ± 0.0
9	59.7 ± 35.0	8.1 ± 20.7	0 ± 0.2	70.6 ± 38.1	2.7 ± 11.3	0.0 ± 0.0
10	35.8 ± 36.9	7.2 ± 20.1	0 ± 0.2	51.7 ± 41.1	2.5 ± 10.8	0.0 ± 0.0
11	32.5 ± 34.5	5.1 ± 13.9	0 ± 0.1	48.7 ± 40.5	1.5 ± 6.1	0.0 ± 0.0
12	41.1 ± 40.1	9.1 ± 21.0	0.1 ± 0.6	53.0 ± 40.6	3.3 ± 11.7	0.0 ± 0.0
13	41.1 ± 40.1	9.1 ± 21.0	0.1 ± 0.6	53.0 ± 40.6	3.3 ± 11.7	0.0 ± 0.0
14	41.1 ± 40.1	9.1 ± 21.0	0.1 ± 0.6	53.0 ± 40.6	3.3 ± 11.7	0.0 ± 0.0
15	41.1 ± 40.1	9.1 ± 21.0	0.1 ± 0.6	53.0 ± 40.6	3.3 ± 11.7	0.0 ± 0.0
16	41.1 ± 40.1	9.1 ± 21.0	0.1 ± 0.6	53.0 ± 40.6	3.3 ± 11.7	0.0 ± 0.0
17	32.5 ± 34.5	5.1 ± 13.9	0.1 ± 0.1	48.7 ± 40.5	1.5 ± 6.1	0.0 ± 0.0
18	41.1 ± 40.1	9.1 ± 21.0	0.1 ± 0.6	53.0 ± 40.6	3.3 ± 11.7	0.0 ± 0.0
19	41.1 ± 40.1	9.1 ± 21.0	0.1 ± 0.6	53.0 ± 40.6	3.3 ± 11.7	0.0 ± 0.0
20	38.7 ± 37.5	6.5 ± 18.5	0.1 ± 0.6	49.8 ± 43.3	2.5 ± 10.7	0.0 ± 0.0
21	38.7 ± 37.5	6.5 ± 18.5	0.1 ± 0.6	49.8 ± 43.3	2.5 ± 10.7	0.0 ± 0.0
22	15.8 ± 24.4	0.4 ± 3.1	0.0 ± 0.0	25.5 ± 38.0	0.1 ± 1.5	0.0 ± 0.0
23	15.8 ± 24.4	0.4 ± 3.1	0.0 ± 0.0	25.5 ± 38.0	0.1 ± 1.5	0.0 ± 0.0
24	15.8 ± 24.4	0.4 ± 3.1	0.0 ± 0.0	25.5 ± 38.0	0.1 ± 1.5	0.0 ± 0.0

Table A5. Mean and standard deviation of crop yield loss (%) over the studied agricultural area, by biweekly period, from the IM model, associated with tephra fallout exceeding thresholds with 10%, 50%, and 90% probability under VEI 2 and VEI 3 eruption scenarios.

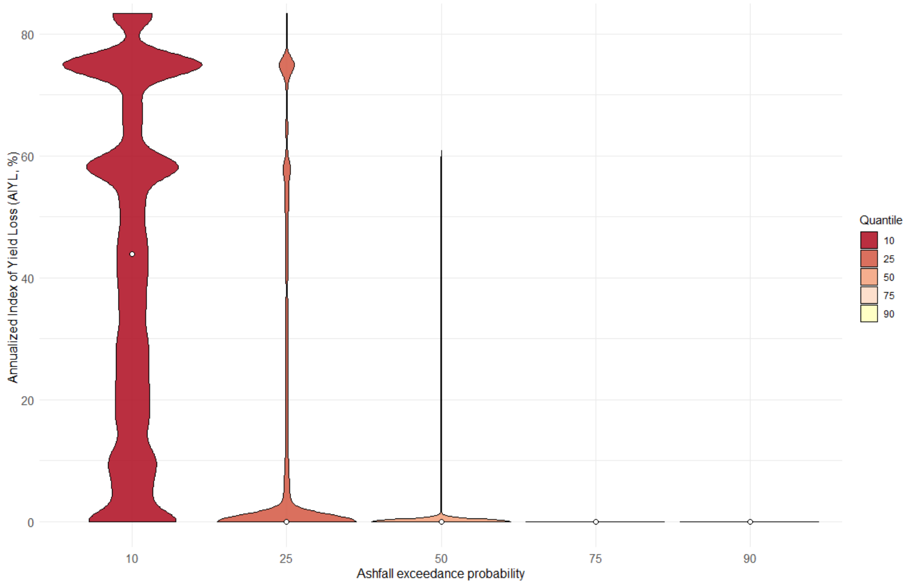

Figure A11. Distribution of the Annualized Index of Yield Loss (AIYL, %) over the agricultural area, from the IM model, for different tephra loads exceedance probabilities under the VEI 3 scenario.

Period (biweekly)	VEI 2 eruption scenario	VEI 3 eruption scenario
1	0.0 ± 0.0	0.0 ± 0.0
2	0.0 ± 0.0	0.0 ± 0.0
3	0.0 ± 0.0	0.0 ± 0.0
4	9.0 ± 21.0	21.7 ± 39.4
5	13.1 ± 21.5	37.7 ± 36.4
6	15.3 ± 21.2	71.6 ± 35.6
7	24.3 ± 36.4	45.4 ± 39.6
8	40.8 ± 36.7	63.1 ± 42.2
9	29.6 ± 29.7	75.8 ± 34.8
10	19.7 ± 30.5	52.0 ± 40.3
11	18.4 ± 26.6	52.8 ± 38.0
12	30.0 ± 34.2	60.0 ± 42.2
13	27.2 ± 32.5	66.3 ± 37.7
14	32.5 ± 31.8	79.1 ± 29.7
15	31.9 ± 34.7	68.6 ± 39.3
16	30.5 ± 36.2	64.3 ± 36.9
17	23.7 ± 28.3	57.5 ± 38.9
18	35.9 ± 35.6	69.6 ± 41.5
19	32.4 ± 34.3	75.3 ± 34.7
20	34.4 ± 36.9	53.4 ± 47.9
21	37.3 ± 35.0	75.3 ± 40.3
22	11.3 ± 18.1	37.0 ± 45.2
23	10.8 ± 18.6	13.0 ± 25.3
24	12.1 ± 19.4	36.3 ± 43.6

Table A6. Mean and standard deviation of crop yield loss (%) over the studied agricultural area, by biweekly period, from the 1000 simulations model under VEI 2 and VEI 3 eruption scenarios.

Period (biweekly)	VEI 2 eruption scenario			VEI 3 eruption scenario		
	Olive trees	Orchards	Vineyards	Olive trees	Orchards	Vineyards
1	0.0 ± 0.0	0.0 ± 0.0	0.0 ± 0.0	0.0 ± 0.0	0.0 ± 0.0	0.0 ± 0.0
2	0.0 ± 0.0	0.0 ± 0.0	0.0 ± 0.0	0.0 ± 0.0	0.0 ± 0.0	0.0 ± 0.0
3	0.0 ± 0.0	0.0 ± 0.0	0.0 ± 0.0	0.0 ± 0.0	0.0 ± 0.0	0.0 ± 0.0
4	0.0 ± 0.0	25.6 ± 28.7	0.0 ± 0.0	0.0 ± 0.0	61.8 ± 44.0	0.0 ± 0.0
5	6.2 ± 7.0	29.4 ± 28.8	0.0 ± 0.0	33.1 ± 25.9	66.0 ± 35.2	0.0 ± 0.0
6	6.8 ± 6.8	27.9 ± 28.6	11.9 ± 15.2	70.0 ± 32.5	75.1 ± 39.1	69.0 ± 35.0
7	4.8 ± 6.7	58.0 ± 43.1	8.6 ± 12.8	21.6 ± 21.2	79.9 ± 28.9	37.0 ± 43.3
8	38.3 ± 26.9	61.7 ± 42.6	11.5 ± 15.8	69.4 ± 37.3	70.6 ± 41.4	37.9 ± 43.4
9	30.2 ± 22.2	18.9 ± 22.6	46.2 ± 42.6	87.8 ± 22.7	59.9 ± 43.0	77.7 ± 29.3
10	3.1 ± 4.9	21.6 ± 26.5	50.7 ± 40.4	28.8 ± 30.0	58.4 ± 42.1	88.5 ± 19.1
11	4.1 ± 5.3	22.9 ± 26.6	39.9 ± 34.6	37.0 ± 25.5	63.0 ± 41.8	68.0 ± 40.9
12	6.6 ± 6.5	50.0 ± 38.3	44.6 ± 31.4	51.2 ± 39.8	68.5 ± 43.6	63.6 ± 41.1
13	3.7 ± 4.9	46.5 ± 35.4	43.1 ± 29.2	46.0 ± 35.1	80.3 ± 34.1	84.3 ± 27.2
14	5.7 ± 5.5	52.5 ± 31.2	54.0 ± 22.0	59.5 ± 31.3	92.2 ± 20.1	97.5 ± 8.3
15	5.0 ± 8.0	50.2 ± 35.3	56.5 ± 29.0	44.6 ± 37.3	81.4 ± 34.8	96.3 ± 13.7
16	4.5 ± 9.2	46.0 ± 36.8	57.7 ± 34.9	38.9 ± 34.0	81.0 ± 27.9	88.7 ± 19.6
17	7.1 ± 8.3	25.5 ± 23.4	54.5 ± 34.7	37.8 ± 32.3	66.1 ± 39.8	83.5 ± 27.8
18	10.9 ± 9.9	55.5 ± 37.6	54.8 ± 33.8	68.8 ± 38.1	75.0 ± 41.2	62.4 ± 46.9
19	6.9 ± 7.3	51.1 ± 35.5	53.6 ± 31.2	58.6 ± 37.6	85.5 ± 29.5	92.6 ± 17.2
20	33.0 ± 30.3	57.0 ± 38.7	0.0 ± 0.0	66.1 ± 44.3	70.2 ± 43.4	0.0 ± 0.0
21	34.8 ± 23.7	63.0 ± 35.6	0.0 ± 0.0	95.2 ± 10.8	96.5 ± 9.6	0.0 ± 0.0
22	25.9 ± 19.2	0.0 ± 0.0	0.0 ± 0.0	85.1 ± 24.5	0.0 ± 0.0	0.0 ± 0.0
23	24.9 ± 21.2	0.0 ± 0.0	0.0 ± 0.0	29.9 ± 31.1	0.0 ± 0.0	0.0 ± 0.0
24	27.8 ± 20.8	0.0 ± 0.0	0.0 ± 0.0	83.6 ± 20.6	0.0 ± 0.0	0.0 ± 0.0

Table A7. Mean and standard deviation of crop yield loss (%) by crop, by biweekly period, from the 1000 simulations model under VEI 2 and VEI 3 eruption scenarios.

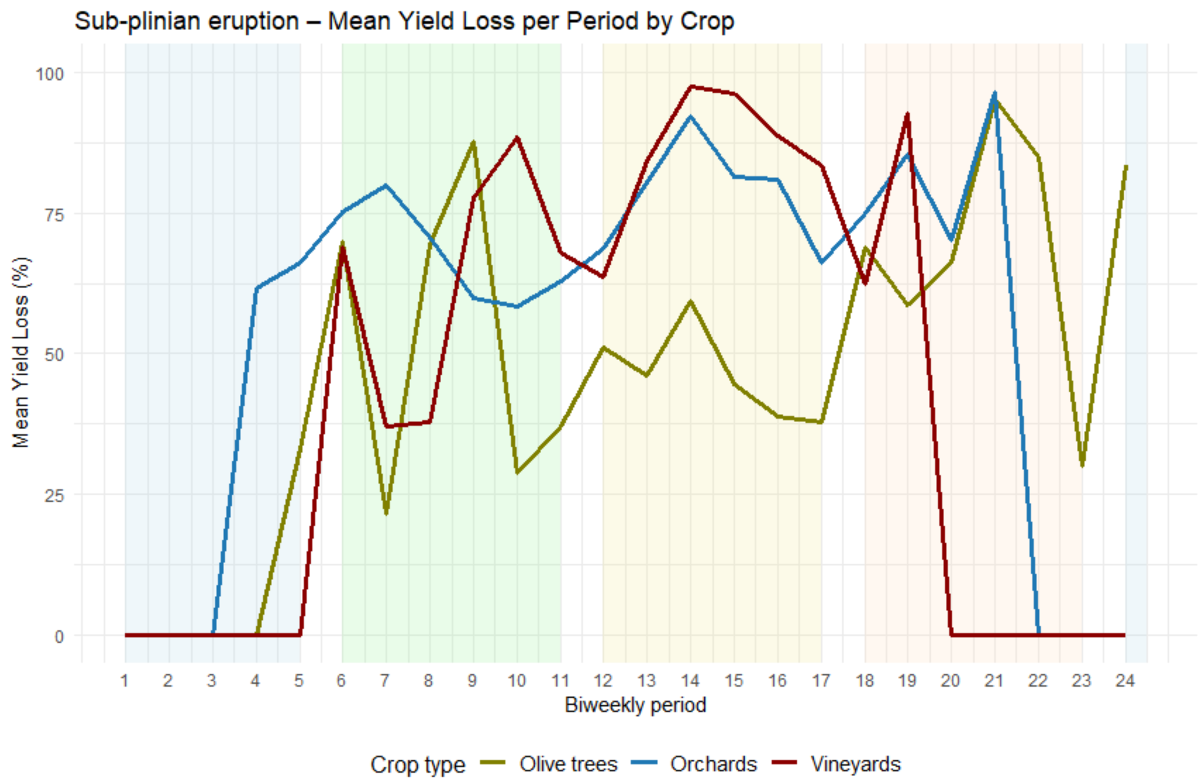

Figure A12. Mean and standard deviation of crop yield loss over the studied agricultural area per studied crop, by biweekly period, from the 1000 simulations model under the VEI 3 eruption scenario.

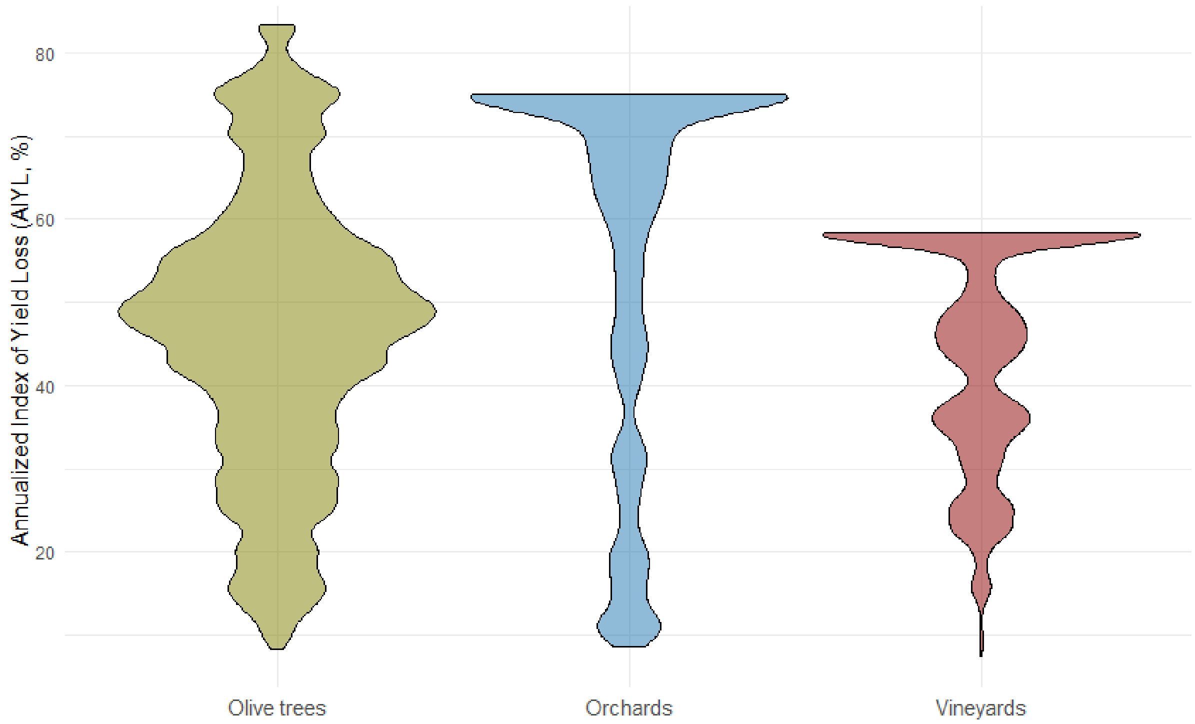

Figure A13. Distribution of the Annualized Index of Yield Loss (AIYL, %) over the different crops, from the 1000 simulations model under the VEI 3 eruption scenario.

References

Aiuppa, A., Bellomo, S., Brusca, L., D'Alessandro, W., & Federico, C. (2003). Natural and anthropogenic factors affecting groundwater quality of an active volcano (Mt. Etna, Italy). *Applied Geochemistry*, *18*(6), 863–882. https://doi.org/10.1016/S0883-2927(02)00182-8

Andronico, D., Branca, S., Calvari, S., Burton, M., Caltabiano, T., Corsaro, R. A., Del Carlo, P., Garf�, G., Lodato, L., Miraglia, L., Mur�, F., Neri, M., Pecora, E., Pompilio, M., Salerno, G., & Spampinato, L. (2005). A multi-disciplinary study of the 2002?03 Etna eruption: Insights into a complex plumbing system. *Bulletin of Volcanology*, *67*(4), 314–330. https://doi.org/10.1007/s00445-004-0372-8

Andronico, D., Scollo, S., Caruso, S., & Cristaldi, A. (2008). The 2002–03 Etna explosive activity: Tephra dispersal and features of the deposits. *Journal of Geophysical Research: Solid Earth*, *113*(B4). https://doi.org/10.1029/2007JB005126

Angys. (n.d.). *Pere dell'Etna, le varietà di pera siciliane | Pera Angys*. Retrieved April 30, 2025, from https://www.angys.net/pere-delletna-le-varieta-di-pera-siciliane/

Aspinall, W., & Blong, R. (2015). Volcanic Risk Assessment. In *The Encyclopedia of Volcanoes* (pp. 1215–1231). Elsevier. https://doi.org/10.1016/B978-0-12-385938-9.00070-5

Ayris, P., & Delmelle, P. (2012). Volcanic and atmospheric controls on ash iron solubility: A review. *Physics and Chemistry of the Earth, Parts A/B/C*, *45–46*, 103–112. https://doi.org/10.1016/j.pce.2011.04.013

Ayris, P. M., & Delmelle, P. (2012). The immediate environmental effects of tephra emission. *Bulletin of Volcanology*, *74*(9), 1905–1936. https://doi.org/10.1007/s00445-012-0654-5

Barbera, G., Carimi, F., & Inglese, P. (1992). Past and present role of the Indian-fig prickly-pear (Opuntia ficus-indica (L.) Miller, Cactaceae) in the agriculture of sicily. *Economic Botany*, *46*(1), 10–20. https://doi.org/10.1007/BF02985249

Barnard, S. T. (2004). Results of a reconnaissance trip to Mt. Etna, Italy. *Bulletin of the New Zealand Society for Earthquake Engineering*, *37*(2), 47–61. https://doi.org/10.5459/bnzsee.37.2.47-61

Berud, M., & Simler, O. (2018). *Arboriculture—Bilan de campagne 2018* (No. 27; Bulletin de santé du végétal, p. 23). DRAAF Service Régional de l'ALimentation PACA. chrome-extension://efaidnbmnnnibpcajpcglclefindmkaj/https://draaf.paca.agriculture.gouv.fr/IMG/pdf/BSV_PACA_Arbo_27_BILAN2018_21_decembre_2018_cle8ec67c.pdf

Biass, S., Bonadonna, C., Connor, L., & Connor, C. (2016). TephraProb: A Matlab package for probabilistic hazard assessments of tephra fallout. *Journal of Applied Volcanology*, *5*(1), 10. https://doi.org/10.1186/s13617-016-0050-5

Biscoe, P. V., Gallagher, J. N., Landsberg, J. J., & Cutting, C. V. (1977). Weather, dry matter production and yield. In J. J. Landsberg & C. V. Cutting (Eds.), *Environmental Effects on Crop Physiology* (pp. 75–100). AcademicPress.

Black, R. A., & Mack, R. N. (1984). Aseasonal leaf abscission in Populus induced by volcanic ash. *Oecologia*, *64*(3), 295–299. https://doi.org/10.1007/BF00379124

Blaikie, P. (Ed.). (1994). *At risk: Natural hazards, people's vulnerability, and disasters* (1. publ). Routledge.

Blong, R. J. (1984). *Volcanic hazards. A sourcebook on the effects of eruptions*. https://www.osti.gov/biblio/7057586

Blong, R. J. (Russell J.) (with Internet Archive). (1984). *Volcanic hazards: A sourcebook on the effects of eruptions*. Sydney ; Orlando, Fla. : Academic Press. http://archive.org/details/volcanichazardss0000blon

Bonadonna, C., Connor, C. B., Houghton, B. F., Connor, L., Byrne, M., Laing, A., & Hincks, T. K. (2005). Probabilistic modeling of tephra dispersal: Hazard assessment of a multiphase rhyolitic eruption at Tarawera, New Zealand. *Journal of Geophysical Research: Solid Earth*, *110*(B3), 2003JB002896. https://doi.org/10.1029/2003JB002896

Bonadonna, C., Connor, C., Houghton, B., Connor, L., Byrne, M., Laing, A., Hincks, T., & Probabilistic. (2005). Probabilistic modeling of tephra dispersal: Hazard assessment of a multiphase rhyolitic eruption at Tarawera, New Zealand. *Geology Faculty Publications. Paper*, *18*. https://doi.org/10.1029/2003JB002896

Bonadonna, C., & Costa, A. (2013). Plume height, volume, and classification of explosive volcanic eruptions based on the Weibull function. *Bulletin of Volcanology*, *75*(8), 742. https://doi.org/10.1007/s00445-013-0742-1

Bonadonna, C., Costa, A., Folch, A., & Koyaguchi, T. (2015). Tephra Dispersal and Sedimentation. In *The Encyclopedia of Volcanoes* (pp. 587–597). Elsevier. https://doi.org/10.1016/B978-0-12-385938-9.00033-X

Bonadonna, C., Ernst, G. G. J., & Sparks, R. S. J. (1998). Thickness variations and volume estimates of tephra fall deposits: The importance of particle Reynolds number. *Journal of Volcanology and Geothermal Research*, *81*(3), 173–187. https://doi.org/10.1016/S0377-0273(98)00007-9

Bonadonna, C., & Houghton, B. F. (2005). Total grain-size distribution and volume of tephra-fall deposits. *Bulletin of Volcanology*, *67*(5), 441–456. https://doi.org/10.1007/s00445-004-0386-2

Bosi, V., & MIAVITA group. (2012). *Handbook for volcanic risk management: Prevention, crisis management and resilience*. https://doi.org/10.13140/2.1.2167.0083

Branca, S., & Carlo, P. D. (2005). Types of eruptions of Etna volcano AD 1670–2003: Implications for short-term eruptive behaviour. *Bulletin of Volcanology*, *67*(8), 732–742. https://doi.org/10.1007/s00445-005-0412-z

Branca, S., & Del Carlo, P. (2004). Eruptions of Mt. Etna during the past 3,200 Years: A revised compilation integrating the historical and stratigraphic records. In A. Bonaccorso, S. Calvari, M. Coltelli, C. Del Negro, & S. Falsaperla (Eds.), *Geophysical Monograph Series* (Vol. 143, pp. 1–27). American Geophysical Union. https://doi.org/10.1029/143GM02

BRAVOLEUM. (n.d.). *Olive phenological stages | Noticias Aceite de Oliva*. BRAVOLEUM. Retrieved December 16, 2024, from https://www.bravoleum.com/en/blog/olive-phenological-stages

Brown, S. K., Auker, M. R., & Sparks, R. S. J. (2015). Populations around Holocene volcanoes and development of a Population Exposure Index. In S. C. Loughlin, S. Sparks, S. K. Brown, S. F. Jenkins, & C. Vye-Brown (Eds.), *Global Volcanic Hazards and Risk* (1st ed., pp. 223–232). Cambridge University Press. https://doi.org/10.1017/CBO9781316276273.006

Burket, S. D., Furlow, E. P., Golding, P. R., Grant, L. C., Lipovsky, W. A., & Lopp, T. G. (1980). *The economic effects of the eruptions of Mt. St. Helens, United States International Trade Commission, Washington, D.C*. 84.

Bursik, M. I., Sparks, R. S. J., Gilbert, J. S., & Carey, S. N. (1992). Sedimentation of tephra by volcanic plumes: I. Theory and its comparison with a study of the Fogo A plinian deposit, Sao Miguel (Azores). *Bulletin of Volcanology*, *54*(4), 329–344. https://doi.org/10.1007/BF00301486

Capitanio, F., & De Pin, A. (2018). Measures of Efficiency of Agricultural Insurance in Italy, Economic Evaluations. *Risks*, *6*(4), Article 4. https://doi.org/10.3390/risks6040126

Carey, S., & Bursik, M. (2015). Volcanic Plumes. In *The Encyclopedia of Volcanoes* (pp. 571–585). Elsevier. https://doi.org/10.1016/B978-0-12-385938-9.00032-8

Carey, S., & Sparks, R. S. J. (1986). Quantitative models of the fallout and dispersal of tephra from volcanic eruption columns. *Bulletin of Volcanology*, *48*(2), 109–125. https://doi.org/10.1007/BF01046546

Carrão, H., Naumann, G., & Barbosa, P. (2016). Mapping global patterns of drought risk: An empirical framework based on sub-national estimates of hazard, exposure and vulnerability. *Global Environmental Change*, *39*, 108–124. https://doi.org/10.1016/j.gloenvcha.2016.04.012

Chasseloup, M. (2024). *Tout savoir sur la taille de la vigne: Quand, comment et pourquoi ?* Millesima. https://www.millesima.be/blog/tout-savoir-sur-la-taille-de-la-vigne-quand-comment-et-pourquoi.html

Chester, D. K., Duncan, A. M., Guest, J. E., & Kilburn, C. R. J. (1985). Etna and the Etna region. In D. K. Chester, A. M. Duncan, J. E. Guest, & C. R. J. Kilburn (Eds.), *Mount Etna: The anatomy of a volcano* (pp. 37–64). Springer Netherlands. https://doi.org/10.1007/978-94-009-4079-6_2

Chester, D. K., Duncan, A. M., & James, P. A. (2010). Mount Etna, Sicily: Landscape Evolution and Hazard Responses in the Pre-industrial Era. In I. P. Martini & W. Chesworth (Eds.), *Landscapes and Societies* (pp. 235–253). Springer Netherlands. https://doi.org/10.1007/978-90-481-9413-1_15

Coltelli, M., Del Carlo, P., & Vezzoli, L. (1998). Discovery of a Plinian basaltic eruption of Roman age at Etna volcano, Italy. *Geology*, *26*(12), 1095. https://doi.org/10.1130/0091-7613(1998)026<1095:DOAPBE>2.3.CO;2

Consorzio Tutela Vini Etna DOC. (2022). *Terroir*. Consorzio Tutela Vini Etna DOC. https://thewinesofetna.com/terroir/

Cook, R. J., Barron, J. C., Papendick, R. I., & Williams, G. J. (1981). Impact on agriculture of the mount st. Helens eruptions. *Science (New York, N.Y.)*, *211*(4477), 16–22. https://doi.org/10.1126/science.211.4477.16

Craig, H. (2015). *Agricultural vulnerability to tephra fall impacts*. University of Canterbury.

Craig, H., Wilson, T., Magill, C., Stewart, C., & Wild, A. J. (2021). Agriculture and forestry impact assessment for tephra fall hazard: Fragility function development and New Zealand scenario application. *Volcanica*, *4*(2), Article 2. https://doi.org/10.30909/vol.04.02.345367

Craig, H., Wilson, T., Stewart, C., Villarosa, G., Outes, V., Cronin, S., & Jenkins, S. (2016). Agricultural impact assessment and management after three widespread tephra falls in Patagonia, South America. *Natural Hazards*, *82*(2), 1167–1229. https://doi.org/10.1007/s11069-016-2240-1

CREA. (2024a). *L'agricoltura in Sicilia in cifre 2024*. Consiglio per la ricerca in agricoltura e l'analisi dell'economia. https://www.crea.gov.it/documents/68457/0/Sicilia_InCifre_2024_WEB_DEF.pdf/e67d66cc-c517-37f8-63d5-4579b19f8a53?t=1729168040949

CREA, C. di ricerca P. e B. (2020). *Annuario dell'Agricoltura italiana*. chrome-extension://efaidnbmnnnibpcajpcglclefindmkaj/https://www.fondazionesviluppososte nibile.org/wp-content/uploads/dlm_uploads/Annuario_CREA_2020_Volume_LXXIV.pdf

CREA, C. di ricerca P. e B. (2024b). *L'agricoltura in Sicilia in cifre 2024*. https://pti.regione.sicilia.it/portal/page/portal/PIR_PORTALE/PIR_LaStrutturaRegionale/PIR_AssessoratoEconomia/PIR_DipBilancioTesoro/PIR_Areetematiche/PIR_ServizioStatistica/PIR_cofanetto

Cronin, S. J., Hedley, M. J., Neall, V. E., & Smith, R. G. (1998). Agronomic impact of tephra fallout from the 1995 and 1996 Ruapehu Volcano eruptions, New Zealand. *Environmental Geology*, *34*(1), 21–30. https://doi.org/10.1007/s002540050253

Cronin, S. J., Neall, V. E., Lecointre, J. A., Hedley, M. J., & Loganathan, P. (2003). Environmental hazards of fluoride in volcanic ash: A case study from Ruapehu volcano, New Zealand. *Journal of Volcanology and Geothermal Research*, *121*(3–4), 271–291. https://doi.org/10.1016/S0377-0273(02)00465-1

cyber. (2019, September 4). Les fruits de la vallée de l'Etna. *Excellence de Sicile*. https://excellencedesicile.com/les-fruits-de-la-vallee-de-letna/

Dahlgren, R. A., Saigusa, M., & Ugolini, F. C. (2004). The Nature, Properties and Management of Volcanic Soils. In *Advances in Agronomy* (Vol. 82, pp. 113–182). Elsevier. https://doi.org/10.1016/S0065-2113(03)82003-5

DALIVAL. (n.d.). *Calendario di raccolta ciliegia*. DALIVAL. Retrieved April 30, 2025, from https://www.dalival.com/i-nostri-consigli-pratici/calendario-raccolta/calendario-di-raccolta-ciliegio/

D'Arapri. (n.d.). *LE CYCLE ANNUEL DE LA VIGNE - d'Araprì*. Retrieved April 29, 2025, from https://www.darapri.it/approfondimenti/il-ciclo-della-vite/

Dazzi, C. (2007). Environmental features and land use of Etna (Sicily—Italy). In Ó. Arnalds, H. Óskarsson, F. Bartoli, P. Buurman, G. Stoops, & E. García-Rodeja (Eds.), *Soils of Volcanic Regions in Europe* (pp. 629–644). Springer Berlin Heidelberg. https://doi.org/10.1007/978-3-540-48711-1_44

Diaz, F., Jimenez, C. C., & Tejedor, M. (2005). Influence of the thickness and grain size of tephra mulch on soil water evaporation. *Agricultural Water Management*, *74*(1), 47–55. https://doi.org/10.1016/j.agwat.2004.10.011

DRAAF Occitanie. (2023). *Comment intégrer le changement climatique dans l'accompagnement des agriculteurs ? Etat de l'art pour une approche par filière en Occitanie*. https://draaf.occitanie.agriculture.gouv.fr/comment-integrer-le-changement-climatique-dans-l-accompagnement-des-a8989.html

Durant, A. J., Bonadonna, C., & Horwell, C. J. (2010). Atmospheric and Environmental Impacts of Volcanic Particulates. *Elements*, *6*(4), 235–240. https://doi.org/10.2113/gselements.6.4.235

ECORYS. & Wageningen Economic Research. (2017). *Study on risk management in EU agriculture: Final report.* Publications Office. https://data.europa.eu/doi/10.2762/387583

Edwards, K. J., Dugmore, A. J., & Blackford, J. J. (2004). Vegetational response to tephra deposition and land-use change in Iceland: A modern analogue and multiple working hypothesis approach to tephropalynology. *Polar Record*, *40*(2), 113–120. https://doi.org/10.1017/S0032247403003000

Eggler, W. A. (1948). Plant Communities in the Vicinity of the Volcano El Paricutin, Mexico, After Two and A Half Years of Eruption. *Ecology*, *29*(4), 415–436. https://doi.org/10.2307/1932635

Eggler, W. A. (1963). Plant Life of Paricutin Volcano, Mexico, Eight Years After Activity Ceased. *American Midland Naturalist*, *69*(1), 38. https://doi.org/10.2307/2422843

EM-DAT. (2017). *The international disaster database*. https://www.emdat.be/

Eswaran, H., Van Den Berg, E., & Reich, P. (1993). Organic Carbon in Soils of the World. *Soil Science Society of America Journal*, *57*(1), 192–194. https://doi.org/10.2136/sssaj1993.03615995005700010034x

Eychenne, J., & Le Pennec, J.-L. (2012). Sigmoidal particle density distribution in a subplinian scoria fall deposit. *Bulletin of Volcanology*, *74*(10), 2243–2249. https://doi.org/10.1007/s00445-012-0671-4

FAO. (2018). *The impact of disasters and crises on agriculture and food security 2017*. Food and Agriculture Organization of the United Nations.

FAO. (2021). *The impact of disasters and crises on agriculture and food security: 2021*. FAO. https://doi.org/10.4060/cb3673en

FAO. (2023). *Crop calendar—Information Tool for Crop Production*. (Food and Agriculture Organisation). https://cropcalendar.apps.fao.org/#/home

Fao Crop Calendar. (n.d.). Retrieved April 29, 2025, from https://cropcalendar.apps.fao.org/#/home?id=&crops=0245

Fernández, V., & Eichert, T. (2009). Uptake of Hydrophilic Solutes Through Plant Leaves: Current State of Knowledge and Perspectives of Foliar Fertilization. *Critical Reviews in Plant Sciences*, *28*(1–2), 36–68. https://doi.org/10.1080/07352680902743069

Ferrara, V., & Ingemark, D. (2023). The Entangled Phenology of the Olive Tree: A Compiled Ecological Calendar of Olea Europaea L. Over the Last Three Millennia With Sicily as a Case Study. *GeoHealth*, *7*. https://doi.org/10.1029/2022GH000619

Fiantis, D., & Minasny, B. (2017, October 13). Mount Agung: Light will shine out of darkness. *Digital Soil Mapping*. https://www.digitalsoilmapping.com/articles-in-english/mount-agung-light-will-shine-out-of-darkness/

Fierstein, J., & Nathenson, M. (1992). Another look at the calculation of fallout tephra volumes. *Bulletin of Volcanology*, *54*(2), 156–167. https://doi.org/10.1007/BF00278005

Firriato Winery. (2017). *Carricante*. Firriato Winery, Authentic Terroir. https://firriato.it/carricante/?lang=en

Fischer, G., Almanza-Merchán, P. J., & Ramírez, F. (2013). Source-sink relationships in fruit species: A review. *Revista Colombiana de Ciencias Hortícolas*, *6*(2), 238–253. https://doi.org/10.17584/rcch.2012v6i2.1980

Fisher, R. V. (1997). *Volcanic activity and eruptions*. UC Santa Barbara. https://volcanology.geol.ucsb.edu/erupt.htm

Folch, A., Costa, A., & Macedonio, G. (2009). FALL3D: A computational model for transport and deposition of volcanic ash. *Computers & Geosciences*, *35*(6), 1334–1342. https://doi.org/10.1016/j.cageo.2008.08.008

Foulser-Piggott, R., Bevington, J., & Vicini, A. (2014). End-to-end demonstration of the Inventory Data Capture Tools [Pdf]. *GEM Technical Report 2014-06*, 26 pages. https://doi.org/10.13117/GEM.DATA-CAPTURE.TR2014.06

Frankel, C. (2019). *Volcanoes and Wine: From Pompeii to Napa*. University of Chicago Press.

Friedman, D. G. (1984). Natural Hazard Risk Assessment for an Insurance Program. *The Geneva Papers on Risk and Insurance*, *9(30)*, 57–128.

Fuchs, S., Birkmann, J., & Glade, T. (2012). Vulnerability assessment in natural hazard and risk analysis: Current approaches and future challenges. *Natural Hazards*, *64*(3), 1969–1975. https://doi.org/10.1007/s11069-012-0352-9

Gambin, E. (2024, January 6). Mois par mois, tous les travaux de l'oliveraie en 2024. *l'OlivoNews*. https://olivonews.it/fr/mois-par-mois-tous-les-travaux-de-l%27oliveraie-en-2024/

Griggs, R. F. (1919). The beginnings of revegetation in Katmai Valley: In Scientific Results of the Katmai Expedition of the National Geographic Society Paper. *The Ohio Journal of Science*, *v. 19*, . 318-342.

Haehnel, S. (2015, November 26). Comment arquer, pour former vos fruitiers. *Ma passion du verger*. https://mapassionduverger.fr/taille-et-forme-fruitiere/comment-arquer-vos-arbres-fruitiers/

Hed, B., Ngugi, H. K., & Travis, J. W. (2009). Relationship Between Cluster Compactness and Bunch Rot in Vignoles Grapes. *Plant Disease*, *93*(11), 1195–1201. https://doi.org/10.1094/PDIS-93-11-1195

Heins, L. (2025). *Titre du mémoire de Lucie*. UCLouvain.

Heliker, C. (Ed.). (2003). *The Puʿu ʿŌʿō-Kūpaianaha eruption of Kīlauea Volcano, Hawaiʿi: The first 20 years*. U.S. Dept. of the Interior.

Hernández Bermejo, J. E., Jardín Botánico de Córdoba, & FAO (Eds.). (1994). *Neglected crops: 1492 from a different perspective*. Food and Agriculture Organization of the United Nations.

Horwell, C. J., & Baxter, P. J. (2006). The respiratory health hazards of volcanic ash: A review for volcanic risk mitigation. *Bulletin of Volcanology*, *69*(1), 1–24. https://doi.org/10.1007/s00445-006-0052-y

Hurst, A. W., & Turner, R. (1999). Performance of the program ASHFALL for forecasting ashfall during the 1995 and 1996 eruptions of Ruapehu volcano. *New Zealand Journal of*

Geology and Geophysics, *42*(4), 615–622. https://doi.org/10.1080/00288306.1999.9514865

Institut Technique Horticole de Gembloux. (n.d.). *Chapitre 4 Arbres Fruitiers*.

ISMEA, I. di servizi per il mercato agricolo alimentare. (2020). *Report sulla competitività della filiera agrumicola italiana*. https://www.ismea.it/flex/cm/pages/ServeBLOB.php/L/IT/IDPagina/11046

ISTAT, I. nazionale di statistica. (2024). *Commissione parlamentare di inchiesta sulle condizioni di sicurezza e sullo stato di degrado delle città e delle loro periferie—Report Comune di Catania*.

Italian food experience. (2018, May 28). *Pomme de l'Etna: Caractéristiques, production et festivals organisés*. https://blog.foodit.it/prodotti/mela-etna/

Jenkins, S. F., Spence, R. J. S., Fonseca, J. F. B. D., Solidum, R. U., & Wilson, T. M. (2014). Volcanic risk assessment: Quantifying physical vulnerability in the built environment. *Journal of Volcanology and Geothermal Research*, *276*, 105–120. https://doi.org/10.1016/j.jvolgeores.2014.03.002

Jenkins, S., Wilson, T., Magill, C., Miller, V., Stewart, C., Blong, R., Marzocchi, W., Boulton, M., Bonadonna, C., & Costa, A. (2015). Volcanic ash fall hazard and risk. In *Global Volcanic Hazards and Risk* (pp. 173–221). https://doi.org/10.1017/CBO9781316276273.005

Kennedy. (2023). *UCx: Volcanology field science and society.* edX. https://www.edx.org/learn/volcanoes/university-of-canterbury-volcanology-fieldscience-and-society

Khadatkar, A., Sawant, C. P., Thorat, D., Gupta, A., Jadhav, S., Gawande, D., & Magar, A. P. (2025). A comprehensive review on grapes (Vitis spp.) cultivation and its crop management. *Discover Agriculture*, *3*(1), 9. https://doi.org/10.1007/s44279-025-00162-2

Kondo, J. (1988). *Volcanic Eruptions, Cool Summers, and Famines in the Northeastern Part of japan*. https://journals.ametsoc.org/view/journals/clim/1/8/1520-0442_1988_001_0775_vecsaf_2_0_co_2.xml

La Praglia. (2014, June 25). *Calendario dei trattamenti—Pomacee (Pero e Melo)*. La Praglia. https://www.lapraglia.it/calendario-dei-trattamenti-pomacee-pero-melo/

Leonard, G., Johnston, D., Williams, S., Cole, J., Finnis, K., & Barnard, S. (2005). *Impacts and management of recent volcanic eruptions in Ecuador: Lessons for New Zealand*. https://www.semanticscholar.org/paper/Impacts-and-management-of-recent-volcanic-eruptions-Leonard-Johnston/85db07a08e52188f759c6eb802e260eb2121e533

Lieth, H. (1974). *Phenology and seasonality modeling* (American Institute of Biological Sciences, Ed.). Springer-Verlag.

Ligot, N., Bogaert, P., Biass, S., Lobet, G., & Delmelle, P. (2023). *Grain size modulates volcanic ash retention on crop foliage and potential yield loss*. https://doi.org/10.5194/egusphere-2022-687

Ligot, N., De Tornaco, P. M., Pereira, B., Bogaert, P., & Delmelle, P. (2024). Exposure of vegetables to simulated volcanic ashfall reveals production loss controlled by plant traits and growth stage. *Agrosystems, Geosciences & Environment*, *7*(3), e20494. https://doi.org/10.1002/agg2.20494

Ligot, N., Delmelle, P., Bogaert, P., Bernard, D. B., Biass, D. S., Draye, X., & Hanert, E. (2022). *Crop vulnerability to tephra fall in volcanic regions: Field, experimental and modelling approaches*.

Ligot, N., Guevara, A., & Delmelle, P. (2022). Drivers of crop impacts from tephra fallout: Insights from interviews with farming communities around Tungurahua volcano, Ecuador. *Volcanica*, *5*(1), 163–181. https://doi.org/10.30909/vol.05.01.163181

Ligot, N., Viera, W., Peñaherrera, D., Bernard, B., Bogaert, P., & Delmelle, P. (2024). A quantitative assessment of crop vulnerability to tephra hazard at Tungurahua volcano, Ecuador: Understanding the effect of volcanic and biological factors. *Bulletin of Volcanology*, *86*(4), 28. https://doi.org/10.1007/s00445-024-01710-2

LoSaiChe. (2021, May 16). *La Vite—Il ciclo vitale e le fasi fenologiche della pianta*. Losaicheilvino.it. https://losaicheilvino.it/blogs/la-guida-completa-sulla-vigna-la-vite-il-vino/i-cicli-vitali-della-pianta

Macedonio, G., & Costa, A. (2012). Brief Communication "Rain effect on the load of tephra deposits." *Natural Hazards and Earth System Sciences*, *12*(4), 1229–1233. https://doi.org/10.5194/nhess-12-1229-2012

Martí, J., Groppelli, G., & Brum da Silveira, A. (2018). Volcanic stratigraphy: A review. *Journal of Volcanology and Geothermal Research*, *357*, 68–91. https://doi.org/10.1016/j.jvolgeores.2018.04.006

Matheron, G. (1963). Principles of geostatistics. *Economic Geology*, *58*(8), 1246–1266. https://doi.org/10.2113/gsecongeo.58.8.1246

Meier, U. (2001). *Stades phénologiques des mono-et dicotylédones cultivées* (2nd ed.). Centre Fédéral de Recherches Biologiques pour l`Agriculture et les Forêts.

Meilán-Vila, A., Fernández-Casal, R., Crujeiras, R. M., & Francisco-Fernández, M. (2021). A computational validation for nonparametric assessment of spatial trends. *Computational Statistics*, *36*(4), 2939–2965. https://doi.org/10.1007/s00180-021-01108-0

Miller, C. F. (1966). *Operation Ceniza-Arena: The Retention of Fallout Particles from Volcan Irazu (Costa Rica) by Plants and People. Part II. appendices.* (No. AD659385). Stanford Research Inst Menlo Park Calif. https://ntrl.ntis.gov/NTRL/dashboard/searchResults/titleDetail/AD659385.xhtml

Ministero dell’agricoltura, della sovranità alimentare e delle foreste. (2024). *Registro Nazionale delle Varietà di Vite*. http://catalogoviti.politicheagricole.it/catalogo.php?codice=

Ministro dell’agricoltura, della sovranità alimentare e delle foreste. (2022). *Disciplinare di produzione della Denominazione di Origine Controllata “Etna.”* https://www.masaf.gov.it/flex/cm/pages/ServeBLOB.php/L/IT/IDPagina/17936

Monteith, J. L. (1977). Climate and the efficiency of crop production in Britain. *Philosophical Transactions of the Royal Society of London. B, Biological Sciences*, *281*(980), 277–294. https://doi.org/10.1098/rstb.1977.0140

Motooka, P., Castro, L., Nelson, D., Nagai, G., & Ching, L. (2014). *Weeds of Hawai‘i’s Pastures and Natural Areas: An Identification and Management Guide*. https://uhpress.hawaii.edu/title/weeds-of-hawaiis-pastures-and-natural-areas-an-identification-and-management-guide/

Munns, R. (1993). Physiological processes limiting plant growth in saline soils: Some dogmas and hypotheses. *Plant, Cell & Environment*, *16*(1), 15–24. https://doi.org/10.1111/j.1365-3040.1993.tb00840.x

Murata, K. J., Dondoli, C., & Saenz, R. (1966). The 1963–65 eruption of Irazú volcano, Costa Rica (the period of March 1963 to October 1964). *Bulletin Volcanologique*, *29*(1), 763–793. https://doi.org/10.1007/BF02597194

Neild, J. D., Forestry, N. Z. M. of A. and, & Policy (N.Z.), M. A. F. (1998, January 1). *Impact of a volcanic eruption on agriculture and forestry in New Zealand / prepared by: Jeremy Neild*

... *[et al.]*. Impact of a Volcanic Eruption on Agri... | Items | National Library of New Zealand | National Library of New Zealand; Wellington [N.Z.] : Ministry of Agriculture and Forestry, [1998]. https://natlib.govt.nz/records/20520396

Neild, J., O'Flaherty, P., Hedley, P., Underwood, R., Johnston, D., & Christenson, B. (1998). *Impact of a Volcanic Eruption on Agriculture and Forestry in New Zealand*. https://www.semanticscholar.org/paper/Impact-of-a-Volcanic-Eruption-on-Agriculture-and-in-Neild-O'Flaherty/7020fd92da6dd24c0efeb5b65a636f83f922a652

Newhall, C. G., & Self, S. (1982). The volcanic explosivity index (VEI) an estimate of explosive magnitude for historical volcanism. *Journal of Geophysical Research: Oceans*, *87*(C2), 1231–1238. https://doi.org/10.1029/JC087iC02p01231

Newhall, C., & Hoblitt, R. (2002). Constructing event trees for volcanic crises. *Bulletin of Volcanology*, *64*(1), 3–20. https://doi.org/10.1007/s004450100173

Niño, M., Jaimes, M. A., & Reinoso, E. (2015). A risk index due to natural hazards based on the expected annual loss. *Natural Hazards*, *79*(1), 215–236. https://doi.org/10.1007/s11069-015-1837-0

Osservatorio Etneo, S. di C., INGV. (n.d.). *Monte Etna*. Retrieved March 18, 2025, from https://www.ct.ingv.it/index.php/ricerca/i-vulcani-siciliani/etna/l-attivita-esplosiva-dell-etna

Oukabli, A., Laghezali, M., Chahbar, A., & INRA. (1998). Phénologie et fructification du pommier en zone à hiver doux (Maroc). *Fruits*, *53*(2), Article 2.

Palaseanu-Lovejoy, M., Bisson, M., Spinetti, C., Buongiorno, M. F., Alexandrov, O., & Cecere, T. (2019). High-Resolution and Accurate Topography Reconstruction of Mount Etna from Pleiades Satellite Data. *Remote Sensing*, *11*(24), 2983. https://doi.org/10.3390/rs11242983

Palmeri, N. (2009). *Calendario dello agricoltore siciliano* (Carlo Somma). Catia Righi. https://liberliber.it/autori/autori-p/niccolo-palmeri/calendario-dello-agricoltore-siciliano/

Panza, G. F., Irikura, K., Kouteva, M., Peresan, A., Wang, Z., & Saragoni, R. (2011). Advanced Seismic Hazard Assessment. *Pure and Applied Geophysics*, *168*(1–2), 1–9. https://doi.org/10.1007/s00024-010-0179-9

Petino, G., & Privitera, D. (2023). Uncovering the local foodscapes. Exploring the Etna volcano case study, Italy. *AIMS Geosciences*, *9*(2), 392–408. https://doi.org/10.3934/geosci.2023021

Pevreal, C. W. (1993). *Volcanic impact to viticulture in the Hawke's Bay* [BSc Thesis]. University of Canterbury.

Pierantozzi, P., Searles, P., Rousseaux, M., García-Inza, G., Miserere, A., Bodoira, R., Contreras, C., & Maestri, D. (2017). Olive Cultivation in the Southern Hemisphere: Flowering, Water Requirements and Oil Quality Responses to New Crop Environments. *Frontiers in Plant Science*, *8*, 1830. https://doi.org/10.3389/fpls.2017.01830

Pyle, D. M. (1989). The thickness, volume and grainsize of tephra fall deposits. *Bulletin of Volcanology*, *51*(1), 1–15. https://doi.org/10.1007/BF01086757

Qualigeo. (n.d.). Ciliegia dell'Etna PDO. *Qualigeo :: Banca Dati Europea Dei Prodotti DOP IGP STG*. Retrieved April 30, 2025, from https://www.qualigeo.eu/en/product/ciliegia-delletna-pdo//

Quellier, F. (2003). Chapitre IV. L'art de cultiver les arbres fruitiers. In *Des fruits et des hommes: L'arboriculture fruitière en Île-de-France (vers 1600-vers 1800)* (pp. 177–224). Presses universitaires de Rennes. https://doi.org/10.4000/books.pur.17483

Ram, S. S., Majumder, S., Chaudhuri, P., Chanda, S., Santra, S. C., Maiti, P. K., Sudarshan, M., & Chakraborty, A. (2014). Plant canopies: Bio-monitor and trap for re-suspended dust particulates contaminated with heavy metals. *Mitigation and Adaptation Strategies for Global Change*, *19*(5), 499–508. https://doi.org/10.1007/s11027-012-9445-8

Rieger, M. (2006). *Introduction to Fruit Crops* (1st ed.). CRC Press. https://doi.org/10.1201/9781482298055

Rosi, M., Principe, C., & Vecci, R. (1993). The 1631 Vesuvius eruption. A reconstruction based on historical and stratigraphical data. *Journal of Volcanology and Geothermal Research*, *58*(1), 151–182. https://doi.org/10.1016/0377-0273(93)90106-2

Sæbø, A., Popek, R., Nawrot, B., Hanslin, H. M., Gawronska, H., & Gawronski, S. W. (2012). Plant species differences in particulate matter accumulation on leaf surfaces. *Science of The Total Environment*, *427–428*, 347–354. https://doi.org/10.1016/j.scitotenv.2012.03.084

Scollo, S., Coltelli, M., Bonadonna, C., & Del Carlo, P. (2013). Tephra hazard assessment at Mt. Etna (Italy). *Natural Hazards and Earth System Sciences*, *13*(12), 3221–3233. https://doi.org/10.5194/nhess-13-3221-2013

Scollo, S., Prestifilippo, M., Spata, G., D’Agostino, M., & Coltelli, M. (2009). Monitoring and forecasting Etna volcanic plumes. *Natural Hazards and Earth System Sciences*, *9*(5), 1573–1585. https://doi.org/10.5194/nhess-9-1573-2009

Scott, B. J., & Potter, S. H. (2014). Aspects of historical eruptive activity and volcanic unrest at Mt. Tongariro, New Zealand: 1846–2013. *Journal of Volcanology and Geothermal Research*, *286*, 263–276. https://doi.org/10.1016/j.jvolgeores.2014.04.003

Shoji, S., Dahlgren, R., & Nanzyo, M. (1993). Chapter 2 Morphology of Volcanic Ash Soils. In *Developments in Soil Science* (Vol. 21, pp. 7–35). Elsevier. https://doi.org/10.1016/S0166-2481(08)70263-0

Siebert, L., Kimberly, P., & Simkin, T. (2011). *Volcanoes of the World: Third Edition*. University of California Press. https://doi.org/10.1525/9780520947931

Signorello, G., Marzo, A., Prato, C., Sturiale, G., & De Salvo, M. (2020a). Assessing the hidden impacts of hypothetical eruption events at Mount Etna. *Environmental and Sustainability Indicators*, *8*, 100056. https://doi.org/10.1016/j.indic.2020.100056

Signorello, G., Marzo, A., Prato, C., Sturiale, G., & De Salvo, M. (2020b). Assessing the hidden impacts of hypothetical eruption events at Mount Etna. *Environmental and Sustainability Indicators*, *8*, 100056. https://doi.org/10.1016/j.indic.2020.100056

Simkin, T., & Siebert, L. (2007). Earth's volcanoes and eruptions: An overview. In Haraldur Sigurðsson (Ed.), *Encyclopedia of volcanoes* (4. print). Academic Press.

Slow Food. (n.d.). *Antiche mele dell'Etna—Presìdi Slow Food*. Fondazione Slow Food. Retrieved April 30, 2025, from https://www.fondazioneslowfood.com/it/presidi-slow-food/antiche-mele-delletna-2/

Small, C., & Naumann, T. (2001). The global distribution of human population and recent volcanism. *Environmental Hazards*, *3*(3), 93–109. https://doi.org/10.3763/ehaz.2001.0309

Smith, A. M., Coupland, G., Dolan, L., Harberd, N., Jones, J., Martin, C., Sablowski, R., & Amey, A. (2009). *Plant Biology*. Garland Science. https://doi.org/10.1201/9780203852576

Smith, K. (2013). *Environmental hazards: Assessing risk and reducing disaster* (6th ed). Routledge.

Smith, W. H., & Staskawicz, B. J. (1977). Removal of atmospheric particles by leaves and twigs of urban trees: Some preliminary observations and assessment of research needs. *Environmental Management*, *1*(4), 317–330. https://doi.org/10.1007/BF01865859

Smithsonian Institution. (2025). *Global Volcanism Program | Etna*. Smithsonian Institution | Global Volcanism Program. https://volcano.si.edu/volcano.cfm?vn=211060

Soldati, M., & Marchetti, M. (Eds.). (2017a). *Landscapes and Landforms of Italy*. Springer International Publishing. https://doi.org/10.1007/978-3-319-26194-2

Soldati, M., & Marchetti, M. (Eds.). (2017b). *Landscapes and Landforms of Italy*. Springer International Publishing. https://doi.org/10.1007/978-3-319-26194-2

Sparks, R. S. J. (1997). *Volcanic plumes*. Wiley.

Sparks, R. S. J., Bursik, M. I., Ablay, G. J., Thomas, R. M. E., & Carey, S. N. (1992). Sedimentation of tephra by volcanic plumes. Part 2: Controls on thickness and grain-size variations of tephra fall deposits. *Bulletin of Volcanology*, *54*(8), 685–695. https://doi.org/10.1007/BF00430779

Sword-Daniels, V., Wardman, J., Stewart, C., Wilson, T., Johnston, D., & Rossetto, T. (2011). *Infrastructure impacts, management and adaptations to eruptions at Volcan Tungurahua, Ecuador, 1999-2010*.

Tampubolon, J., Nainggolan, H., Ginting, A., & Aritonang, J. (2018). Mount Sinabung Eruption: Impact on Local Economy and Smallholder Farming in KaroRegency, North Sumatra. *IOP Conference Series: Earth and Environmental Science*, *178*(1), 012039. https://doi.org/10.1088/1755-1315/178/1/012039

Terwei, A. (2014). Prunus serotina (black cherry). *CABI Compendium*, *CABI Compendium*, 44360. https://doi.org/10.1079/cabicompendium.44360

Thompson, M. A., Lindsay, J. M., Wilson, T. M., Biass, S., & Sandri, L. (2017). Quantifying risk to agriculture from volcanic ashfall: A case study from the Bay of Plenty, New Zealand. *Natural Hazards*, *86*(1), 31–56. https://doi.org/10.1007/s11069-016-2672-7

Thorarinsson, S., & Sigvaldason, G. E. (1972). The Hekla Eruption of 1970. *Bulletin Volcanologique*, *36*(2), 269–288. https://doi.org/10.1007/BF02596870

Tilling, R. I. (2005). Volcano Hazards. In J. Martí & G. Ernst (Eds.), *Volcanoes and the environment* (p. 55). Cambridge University Press.

Tison, J.-M., Foucault, B. de, & Guiol, F. (with Société botanique de France). (2014). *Flora Gallica: Flore de France*. Biotope.

UNESCO, W. H. C. (2013). *Mount Etna*. UNESCO World Heritage Centre. https://whc.unesco.org/en/list/1427/

UNISDR. (2009). *UNISDR Terminology on Disaster Risk Reduction*. https://www.undrr.org/publication/2009-unisdr-terminology-disaster-risk-reduction

United Nations International Strategy for Disaster Reduction Secretariat (Ed.). (2015). *Making development sustainable: The future of disaster risk management*.

Viticabrol. (n.d.). *Calendrier et cycle de la vigne*. Retrieved April 29, 2025, from https://viticabrol.fr/content/18-calendrier-cycle-de-la-vigne

Wadge, G., Robertson, R., & Voight, B. (2014). *The Eruption of Soufriere Hills Volcano, Montserrat from 2000 to 2010*.

Weraduwage, S. M., Chen, J., Anozie, F. C., Morales, A., Weise, S. E., & Sharkey, T. D. (2015). The relationship between leaf area growth and biomass accumulation in Arabidopsis thaliana. *Frontiers in Plant Science*, *6*. https://doi.org/10.3389/fpls.2015.00167

Wilson, G., Wilson, T. M., Deligne, N. I., & Cole, J. W. (2014). Volcanic hazard impacts to critical infrastructure: A review. *Journal of Volcanology and Geothermal Research*, *286*, 148–182. https://doi.org/10.1016/j.jvolgeores.2014.08.030

Wilson, J. W. (1967). Ecological data on dry-matter production by plants and plant communities. In E. F. Bradley & O. T. Denmead (Eds.), *The Collection and Processing of Field Data*. Interscience Publishers.

Wilson, & Kaye. (2007). *Agricultural fragility estimates for volcanic ash fall hazards*.

Wilson, T., Cole, J., Cronin, S., Stewart, C., & Johnston, D. (2011). Impacts on agriculture following the 1991 eruption of Vulcan Hudson, Patagonia: Lessons for recovery. *Natural Hazards*, *57*(2), 185–212. https://doi.org/10.1007/s11069-010-9604-8

Wilson, T., Kaye, G., Stewart, C., & Cole, J. (2007). *Impacts of the 2006 eruption of Merapi volcano, Indonesia, on agriculture and infrastructure*.

Wilson, T. M. (2009). *Vulnerability of Pastoral Farming Systems to Volcanic Ashfall Hazards*. http://hdl.handle.net/10092/5978

Wilson, T. M., & Cole, J. W. (2007). Potential impact of ash eruptions on dairy farms from a study of the effects on a farm in eastern Bay of Plenty, New Zealand; implications for hazard mitigation. *Natural Hazards*, *43*(1), 103–128. https://doi.org/10.1007/s11069-007-9111-8

Wilson, T. M., Jenkins, S., & Stewart, C. (2015). Impacts from Volcanic Ash Fall. In *Volcanic Hazards, Risks and Disasters* (pp. 47–86). Elsevier. https://doi.org/10.1016/B978-0-12-396453-3.00003-4

Wilson, T. M., Stewart, C., Sword-Daniels, V., Leonard, G. S., Johnston, D. M., Cole, J. W., Wardman, J., Wilson, G., & Barnard, S. T. (2012). Volcanic ash impacts on critical infrastructure. *Physics and Chemistry of the Earth, Parts A/B/C*, *45–46*, 5–23. https://doi.org/10.1016/j.pce.2011.06.006

Winsemius, H. C., Aerts, J. C. J. H., Van Beek, L. P. H., Bierkens, M. F. P., Bouwman, A., Jongman, B., Kwadijk, J. C. J., Ligtvoet, W., Lucas, P. L., van Vuuren, D. P., & Ward, P. J. (2016). Global drivers of future river flood risk. *Nature Climate Change*, *6*(4), 381–385. https://doi.org/10.1038/nclimate2893

Yulianti, A., Sirnawati, E., & Ulpah, A. (2016). Introduction Technology of Cropping Calendar-Information System (CC-IS) for Rice Farming as A Climate Change Adaptation in Indonesia. *International Journal on Advanced Science, Engineering and Information Technology*, *6*(1), 92–96. https://doi.org/10.18517/ijaseit.6.1.659

Spatial and temporal risk assessment of crop yield loss from tephra fall: A case study on Mount Etna

Zoé Saintrain

Volcanic soils cover only about 1% of the world's ice-free land surface but feed at least 10% of the global population thanks to their high fertility. These agriculturally valuable landscapes are subject to multiple volcanic hazards, among which tephra accumulation on crops is the leading cause of agriculture-related losses from volcanic eruptions. Severe and long-lasting tephra fall impacts on agriculture underscore the need for spatial and temporal prioritization of mitigation actions supported by reliable risk models that integrate hazard, exposure and vulnerability. While tephra hazard modelling has advanced substantially, few studies have linked tephra loading to crop damage through empirical relationships or have combined the components of risk in an integrative manner. No study has yet done so at the scale of an entire agricultural area in the vicinity of a volcano.

In this work, we provide a methodology to quantify risk of crop yield loss from tephra fall through the case study of Mount Etna agriculture using two models that differ in hazard data treatment and are applied to two eruption magnitudes. The "IM" model uses probabilistic isomass maps to estimate yield loss for various tephra deposit levels, each with an associated exceedance probability. The "1000 simulations" model applies biweekly mean tephra deposits, producing yield loss estimates without probability values but incorporating wind seasonality. This integrative framework outperforms hazard-, exposure- or vulnerability-based agricultural impact assessments by highlighting risk patterns across multiple spatial and temporal scales. Results show that incorporating wind seasonality in the "1000 simulations" model reveals greater variability in loss magnitude and spatial distribution than models without this component.

These findings represent a contribution and open the way to improvements in volcanic risk management, including resource allocation, land-use planning and targeted preparedness measures. While this research establishes the foundations for a new framework of spatial and temporal risk models for crop yield loss from tephra fall, some limitations remain. Future developments should include refining the vulnerability assessment, adopting a probabilistic biweekly hazard approach for short-term eruptions and incorporating a fully probabilistic framework for eruption scenarios.

UNIVERSITÉ CATHOLIQUE DE LOUVAIN
Faculté des bioingénieurs
Croix du Sud, 2 bte L7.05.01, 1348 Louvain-la-Neuve, Belgique | **www.uclouvain.be/agro**